Technische Universität München
Fakultät für Chemie
Lehrstuhl für Theoretische Chemie

Doping of HfO_2 and ZrO_2 to improve the piezoelectric properties

Max Falkowski

Dissertation

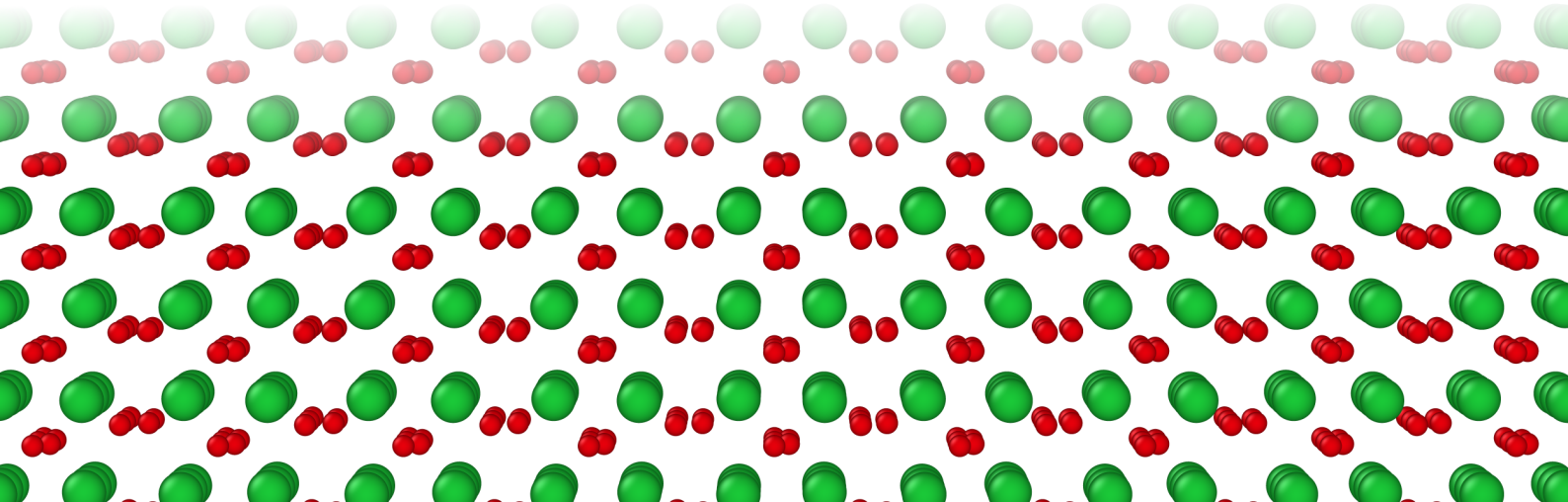

Technische Universität München
Fakultät für Chemie
Lehrstuhl für Theoretische Chemie

Doping of HfO_2 and ZrO_2 to improve the piezoelectric properties

Max Falkowski

Vollständiger Abdruck der von der Fakultät für Chemie der Technischen Universität München zur Erlangung des akademischen Grades eines

Doktors der Naturwissenschaften (Dr. rer. nat.)

genehmigten Dissertation.

Vorsitzender: Priv.-Doz. Dr. Harald Oberhofer

Prüfer der Dissertation:

1. Prof. Dr. Karsten Reuter
2. Prof. Dr. Alfred Kersch
3. Prof. Dr. Andreas Rüdiger

Die Dissertation wurde am 30.07.2020 bei der Technischen Universität München eingereicht und durch die Fakultät für Chemie am 07.09.2020 angenommen.

Abstract

Chemically and structurally, HfO_2 and ZrO_2 are two very similar oxides, which can mix in any proportion with each other and form $Hf_{1-x}Zr_xO_2$ solid solution. In 2011, the ferroelectric hysteresis in Si-doped HfO_2 was reported by Böscke *et al.* for the first time. Owing to the fundamental relations of material properties, a ferroelectric material also exhibits piezoelectric properties. A piezoelectric material accumulates charges on its surfaces if mechanical force is applied and develops mechanical strain if it is subjected to an external electric field. These properties can be utilized in applications such as sensors and actuators. The most important and industrially used piezoelectric material is $Pb(Zr_xTi_{1-x})O_3$ (PZT). However, in times when environmental regulations against the lead-containing electronic devices are issued, the lead-free material class of HfO_2 and ZrO_2 has a particular advantage over PZT. Further advantages of the new material system over the established piezoelectric materials are its silicon technology compatibility and the possibility to manufacture functional thin-films. While the genuine, crystalline piezoelectric effect of HfO_2 and ZrO_2 is small, the observed large piezoelectric activity in these materials is attributed to the crystal volume change during the electric field induced transition from the centrosymmetric $P4_2/mnc$ to the polar $Pbc2_1$ phase. Using *ab initio* calculations, this mechanism is investigated. Furthermore, doped structures are considered in order to optimize the piezoelectric activity in HfO_2 and ZrO_2. The theoretically determined piezoelectric coefficients are found to be in good agreement with the experimentally measured. Moreover, the comparison of HfO_2 and ZrO_2 with other materials shows a high potential of the novel material system for piezoelectric applications.

Zusammenfassung

HfO_2 und ZrO_2 sind chemisch und strukturell zwei sehr ähnliche Oxide, welche sich miteinander in beliebiger Proportion vermischen lassen und ein Mischkristall bilden können. In 2011 wurde zum ersten Mal die ferroelektrische Hysterese im Si-dotierten HfO_2 bei Böscke *et al.* berichtet. Wegen der fundamentalen Relationen der Materialeigenschaften, weist ein ferroelektrisches Material auch piezoelektrische Eigenschaften auf. Ein piezoelektrisches Material akkumuliert Ladung an seinen Oberflächen, wenn mechanische Kräfte einwirken, und entwickelt mechanische Verspannung, wenn es einem externen elektrischen Feld ausgesetzt ist. Diese Eigenschaften können in Anwendungen wie Sensoren und Aktoren verwendet werden. Das wichtigste und industriell verwendete piezoelektrische Material ist $Pb(Zr_xTi_{1-x})O_3$ (PZT). Seitdem ökologische Regulierungsmaßnahmen gegen bleihaltige elektronische Bauelemente erlassen worden sind, hat die bleifreie HfO_2 und ZrO_2 Materialklasse einen besonderen Vorteil gegenüber PZT. Weitere Vorteile des neuen Materialsystems gegenüber den etablierten piezoelektrischen Materialien sind seine Kompatibilität mit der Siliziumtechnologie und die Herstellungsmöglichkeit funktionaler Dünnschichtfilmen. Während der echte, kristalline piezoelektrische Effekt in HfO_2 und ZrO_2 klein ist, ist die große beobachtete piezoelektrische Aktivität in diesen Materialien der Kristallvolumenänderung zuzuschreiben, die während des durch elektrisches Feld induzierten Phasenübergangs von der zentrosymmetrischen $P4_2/mnc$ Phase in die polare $Pbc2_1$ Phase auftritt. Dieser Mechanismus wird mithilfe der *ab initio* Rechnungen untersucht. Außerdem werden dotierte Strukturen betrachtet, um die piezoelektrische Aktivität in HfO_2 und ZrO_2 zu optimieren. Die theoretisch bestimmten piezoelektrischen Koeffizienten sind in guter Übereinstimmung mit den experimentell gemessenen. Insgesamt zeigt der Vergleich von HfO_2 und ZrO_2 mit anderen Materialien ein großes Potential des neuen Materialsystems für piezoelektrische Anwendungen.

Contents

List of Illustrations

Figures

Tables

List of Abbreviations

ALD	atomic layer deposition
BNT	bismuth sodium titanate, $Bi_{0.5}Na_{0.5}TiO_3$
BT	barium titanate, $BaTiO_3$
CMOS	complementary metal oxide semiconductor
CSD	chemical solution deposition
DFT	density functional theory
FeFET	ferroelectric field effect transistor
FeRAM	ferroelectric random access memory
FET	field effect transistor
GGA	generalized gradient approximation
HZO	$Hf_{0.5}Zr_{0.5}O_2$
KNN	potassium-sodium niobate, $K_{0.5}Na_{0.5}NbO_3$
LDA	local density approximation
LGD	Landau–Ginzburg–Devonshire
MD	molecular dynamics
MPB	morphotropic phase boundary
NC	negative capacitance
PLD	pulsed laser deposition
PMN-PT	$Pb(Mg_{1/3}Nb_{2/3})O_3$-$PbTiO_3$
PVD	physical vapor deposition
PZN-PT	$Pb(Zn_{1/3}Nb_{2/3})O_3$-$PbTiO_3$
PZT	lead zirconate titanate, $Pb(Zr_xTi_{1-x})O_3$
XC	exchange-correlation

1 Introduction

This dissertation is based on two published articles that deal with the doping of HfO_2 and ZrO_2 in general and their piezoelectric properties in particular. The aim of the following sections is to motivate the research of the piezoelectric HfO_2 and ZrO_2 and compare them to other established piezoelectric materials. These sections are intentionally written on an introductory level to provide to the reader the basis for the in-depth discussion, which is then led in the articles.

Materials possessing piezoelectric characteristics generate an electric signal as a response to mechanical stress, and mechanical strain if an electric field is applied. In the first case, one speaks about the direct piezoelectric effect. The second case describes the converse piezoelectric effect. First discovered in 1880 by Jacques and Pierre Curie in quartz crystal, nowadays these effects are utilized in various applications like actuators, transducers, sensors, nano-positioners, ultrasonic motors and imaging devices. Piezoelectric materials and devices can be found in the phone and digital cameras, microscope lenses, fuel injectors, micro-pumps, inkjet printers, medical surgery and imaging instruments, etc. [1].

By far the most used piezoelectric material in the industry is lead zirconate titanate, $Pb(Zr_xTi_{1-x})O_3$ (PZT) ceramic, discovered in 1954 by Jaffe *et al.* [2]. During more than 60 years of research and engineering, the lead-containing PZT material system has become the superior piezoelectric material. Owing to the environmental considerations, the European Union legislated the "Directive on the restriction of the use of certain hazardous substances in electrical and electronic equipment", RoHS for short, in 2003 [3, 4]. Shortly after this, other Asian countries like China, Japan, and South Korea enacted similar regulations. This development stimulated the research for the lead-free piezoelectric materials as a substitution for the hazardous lead-containing materials in general and for PZT in particular. There are several known lead-free materials such as barium titanate, $BaTiO_3$ (BT), bismuth sodium titanate, $Bi_{0.5}Na_{0.5}TiO_3$ (BNT), and potassium-sodium niobate, $K_{0.5}Na_{0.5}NbO_3$ (KNN) [1].

The HfO_2, ZrO_2, and their solid solution $Hf_{1-x}Zr_xO_2$ material systems are new and less known piezoelectric materials. In contrast to all previously mentioned materials, which have the perovskite-based crystal structure, the crystal structure of $Hf_{1-x}Zr_xO_2$ is fluorite-based. This material system is lead-free, thus is a potential candidate as PZT replacement. Additionally, $Hf_{1-x}Zr_xO_2$ is compatible with the complementary metal oxide semiconductor (CMOS) technology, which the perovskite-structured materials are not. Thus, $Hf_{1-x}Zr_xO_2$ offers wider integration possibilities in the semiconductor industry.

Ferroelectricity is a material characteristic that describes the nonvanishing electric polarization, whose direction can be reversed if an external field is applied. Thus, a ferroelectric material can have two polarization states: "up" and "down". In 2011, Böscke *et al.* observed for the first time the ferroelectric characteristics in Si-doped HfO_2 [5]. In the same year, the ferroelectric characteristics of $Hf_{0.5}Zr_{0.5}O_2$ (HZO) were also published [6]. This discovery was rather surprising because this material system was already used by the semiconductor industry as a high dielectric constant

(high-κ) material and was believed to be well-understood. Therefore, it attracted researchers from all over the world, because the bi-stable nature of the $Hf_{1-x}Zr_xO_2$ material system and the CMOS compatibility opens the possibility for applications like nonvolatile memory [7] and logic [8]. Substantial progress has been made in the understanding of the ferroelectric $Hf_{1-x}Zr_xO_2$ in the last decade, however, the stabilization of the ferroelectricity in this material system is still not understood in full detail and is the subject of the ongoing research.

As a rule of thumb, the ferroelectric materials have also good piezoelectric characteristics. However, this side of HfO_2 and ZrO_2 is the worst investigated one so far. The current state of the research claims that the major part of the piezoelectric activity in this material system is rather attributed to the phase transition under external electric field, which is accompanied with the crystal volume change, and not to the intrinsic crystalline effect, the genuine piezoelectric effect. This dissertation evaluates precisely this effect and the possibility to improve it via doping from the theoretical point of view. It compares the piezoelectric properties of the fluorite-structured HfO_2 and ZrO_2 with the well-established and widespread perovskite-based materials. In the next chapter, the reader is introduced to the fundamentals of the dielectric material properties, especially genuine piezoelectricity. Also, the nucleation theory is discussed, which is important for the phase transition process, thus for the enhanced piezoelectric characteristics in the $Hf_{1-x}Zr_xO_2$ material system. In chapter 3, the lead-containing and lead-free perovskite-based materials are introduced and discussed in a short manner. Moreover, the important mechanisms of the piezoelectric activity in these materials are presented. Note that genuine piezoelectricity is only one of the four discussed mechanisms. In chapter 4, the novel ferroelectric $Hf_{1-x}Zr_xO_2$ material system is discussed in detail. It deals with its potential application fields and the current state of the research. Chapter 5 contains the summaries of the articles, which were published in the course of this dissertation. The final chapter 6 provides the summary, conclusions, and outlook.

2 Fundamentals

2.1 Hierarchy of material properties

All dielectric materials subjected to an electric field, develop an induced polarization. The polarization is the electric dipole moment density, which is formed by the bound positive and negative charges in the material, which are slightly separated by the field. After the field is removed, the bound charges rearrange themself back and the induced polarization vanishes. Some dielectric materials with a noncentrosymmetric crystalline structure can also develop polarization if mechanical stress is applied. This material property is called piezoelectricity and the described effect is the direct piezoelectric effect. Every piezoelectric material also shows the converse piezoelectric effect, which is the generation of the mechanical strain in response to the applied electric field.

Some piezoelectric materials, which possess polar crystalline structure, retain the polarization also if no electric field is applied. In contrast to the induced polarization, this polarization is called remnant or spontaneous polarization. Owing to the thermal expansion and relative movement of the atoms in the material, the magnitude of the remnant polarization decreases under heating. This material property is called pyroelectricity and the pyroelectric effect describes the changing remnant polarization with temperature.

The induced and remnant polarizations can be superimposed. Therefore, the remnant polarization can be canceled out with an electric field applied in the opposite direction. Furthermore, if the field is high enough and no electric breakdown of the material occurs, the direction of the remnant polarization can be reversed. The pyroelectric materials showing this property are called ferroelectric, similarly to the ferromagnetic materials in which the magnetic polarization can be reversed with the magnetic field. Thus, two stable polarization states exist for ferroelectric materials at zero electric field leading to the prominent hysteresis loop in the P–E–diagram as shown in Fig. 2.1(a).

Analogously to antiferromagnetic, there are also antiferroelectric materials. While in a ferro-

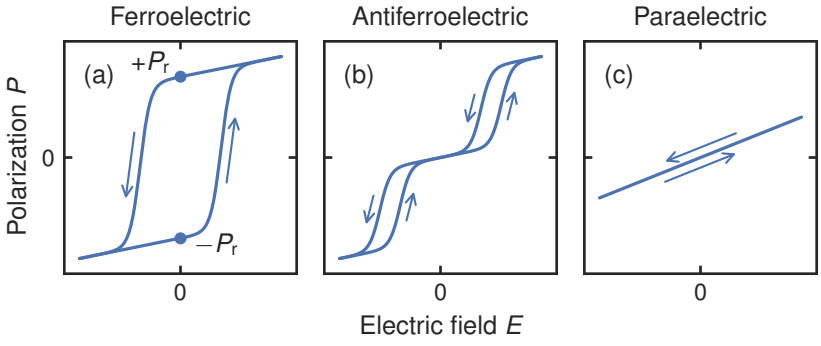

Fig. 2.1: *Sketches of P–E–diagram for (a) ferroelectric, (b) antiferroelectric, and (c) paraelectric materials.*

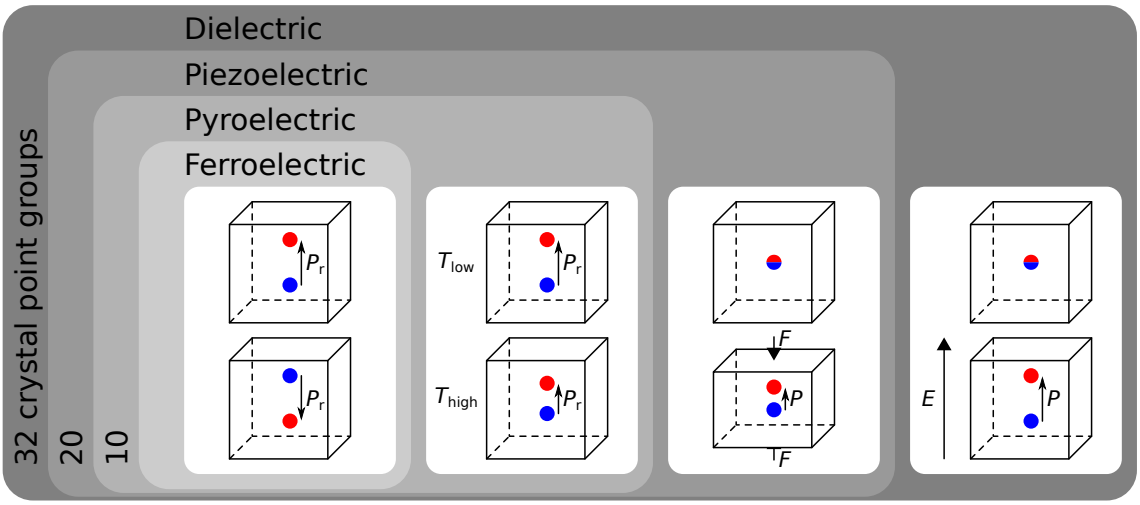

Fig. 2.2: *Hierarchy of material properties in dielectric materials. The red and blue dots represent barycenters of the positive and negative charges, respectively.*

electric material all the electric dipoles point in the same direction at zero field, hence leading to the remnant polarization, in an antiferroelectric material the direction of the dipoles is alternating and the overall polarization at zero field cancels out, which results in a pinched P–E–diagram as depicted in Fig. 2.1(b).

A very important characteristic for both ferroelectric and antiferroelectric materials is that with increasing temperature they undergo a transition to the paraelectric phase and the hysteretic P–E–loop disappears as shown in Fig. 2.1(c). The temperature at which this transition occurs is called Curie temperature T_C. The underlying mechanism for this transition is the crystalline transformation from a polar phase, which allows remnant polarization, to a nonpolar phase, which does not.

This sketched hierarchy of the properties of the dielectric materials underlies the hierarchy of crystal point groups, as depicted in Fig. 2.2. There are 32 point groups in total. Eleven of these point groups contain the point inversion symmetry and are called centrosymmetric, the remaining 21 point groups are noncentrosymmetric. From these 21 point groups, 20 are piezoelectric. Therefore, materials with point inversion symmetry (centrosymmetric) can not exhibit piezoelectricity. Half of the piezoelectric point groups are polar, also called pyroelectric. In theory, every material with pyroelectric point group is ferroelectric, however, in practice, the ferroelectricity is limited by the electric breakdown strength of the material. To sum up, all ferroelectric materials are pyroelectric, which, in turn, are piezoelectric.

2.2 Landau–Ginzburg–Devonshire formalism

From the previous discussion, it is obvious that the polarization of the material is a central quantity for its properties. The Landau–Ginzburg–Devonshire (LGD) formalism [9–11] is a *de facto* standard for the description of the ferroelectricity and antiferroelectricity, and their phase transition to the paraelectricity. Within the frame of LGD, the free energy A of a ferroelectric or antiferroelectric homogeneous bulk system is described as a polynomial of the polarization P. The paraelectric transition is accounted for by making the polynomial coefficients temperature-dependent. The two

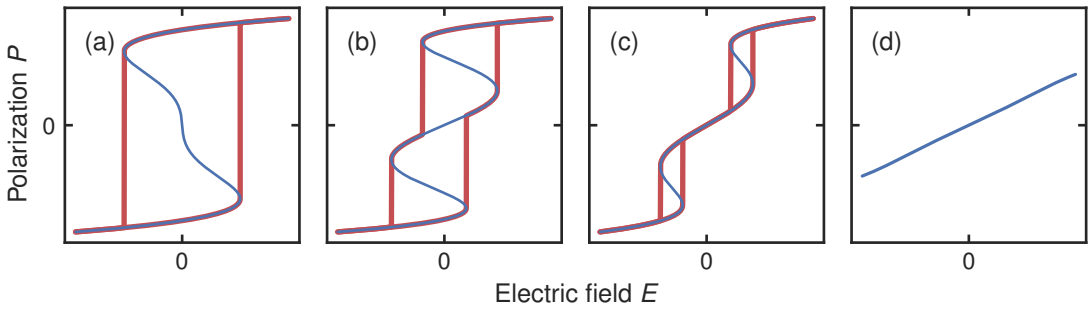

Fig. 2.3: *P–E–diagrams resulting from a sixth-degree LGD model for (a) ferroelectric, (b-c) antiferroelectric with partially and fully pinched loops, and (d) paraelectric materials. The blue lines depict the fifth-degree polynomial according to Eq. (2.2). The red lines in (a-c) depict the shapes of the loops measured in experiments.*

polarization states in a ferroelectric material differ only by the polarization direction and are equal in any other respect, therefore the free energy polynomial must contain only even degree terms in order to satisfy the axial symmetry $A(-P,T) = A(P,T)$. Furthermore, because the polarization states in a ferroelectric material are stable, they have to be separated by some barrier, meaning that the free energy potential must have two local minima. Therefore, for a ferroelectric material, the LGD polynomial has to be at least the fourth-degree. The fourth-degree LGD polynomial describes the second-order phase transition during which the polarization continuously varies and vanishes at the transition to the paraelectric phase. It is not sufficient for antiferroelectric materials, but still useful for ferroelectric materials. For more complicated cases, when the polarization can evolve in more than one Cartesian direction during phase transitions or the low crystal symmetry plays a role, further terms of the free energy polynomial have to be considered.

For the current discussion, and for $Hf_{1-x}Zr_xO_2$ material system in general, it is sufficient to consider the free energy sixth-degree polynomial, which can describe both ferroelectricity and antiferroelectricity [12]:

$$A(P,T) = \frac{\alpha'}{\chi(T)}P^2 + \beta P^4 + \gamma P^6 = \alpha(T - T_0)P^2 + \beta P^4 + \gamma P^6, \tag{2.1}$$

with free energy A, polarization P, dielectric susceptibility χ, temperature T and material-specific Curie–Weiss temperature T_0. α, β, and γ are material dependent fitting coefficients. The temperature dependence of A is encoded in the coefficient in front of the quadratic term and follows the Curie–Weiss law, which describes the temperature dependence of the dielectric susceptibility of the paraelectric phase. At the Curie–Weiss temperature T_0 the dielectric susceptibility χ diverges, a known behavior during (anti)ferroelectric–paraelectric transition. The sixth-degree polynomial describes the first-order phase transition. During the transition to the paraelectric phase, the polarization discontinuously drops to zero at Curie temperature T_C, which is not identical to T_0.

From Eq. (2.1), expression for the electric field $E(P,T)$ can be derived as follows:

$$E(P,T) = \frac{\partial A}{\partial P} = 2\alpha(T - T_0)P + 4\beta P^3 + 6\gamma P^5. \tag{2.2}$$

Varying the temperature T, all experimentally relevant P–E–curves, which are depicted in Fig. 2.3, can be obtained. For the coefficients must hold: $\alpha > 0$, $\beta < 0$, and $\gamma > 0$.

2.3 Piezoelectricity

An electric field $\boldsymbol{E}$ applied to material causes the displacement of its charges $\boldsymbol{D}$. These two electric quantities, which are vectors, are linked through the dielectric permittivity $\boldsymbol{\varepsilon}$, which is a second rank tensor:

$$D_i = \varepsilon_{ik} E_k \quad \text{with} \quad i,k \in \{1,2,3\}. \tag{2.3}$$

The indices i and k stand for the three space dimensions. Similarly, in the mechanical domain, an applied stress $\boldsymbol{T}$ leads to a strain $\boldsymbol{S}$ in the material. Both stress and strain are second rank tensors with diagonal components describing compressive or tensile forces and deformations, respectively. Their off-diagonal components describe shearing. These two mechanical quantities are related to each other through the fourth rank elastic stiffness $\boldsymbol{c}$ and elastic compliance $\boldsymbol{s}$ tensors in the following way:

$$T_{ij} = c_{ijkl} S_{kl}, \tag{2.4}$$

$$S_{ij} = s_{ijkl} T_{kl} \quad \text{with} \quad i,j,k,l \in \{1,2,3\}. \tag{2.5}$$

The symmetry properties of $\boldsymbol{T}$, $\boldsymbol{S}$, $\boldsymbol{c}$, and $\boldsymbol{s}$ [13] allow to use the Voigt's contracted notation, which replaces pairs of the indices ij and kl with indices α and β, respectively. α and β run from 1 to 6 and the prescription rule is listed in Tab. 2.1. Using the Voigt's notation, $\boldsymbol{T}$ and $\boldsymbol{S}$ become vectors, $\boldsymbol{c}$ and $\boldsymbol{s}$ 6×6 matrices, and Eqs. (2.4) and (2.5) simplify to the following matrix form:

$$T_\alpha = c_{\alpha\beta} S_\beta, \tag{2.6}$$

$$S_\alpha = s_{\alpha\beta} T_\beta \quad \text{with} \quad \alpha,\beta \in \{1,2,3,4,5,6\}. \tag{2.7}$$

The Voigt's notation also allows the inverse relation between the elastic stiffness and compliance to be written in the simple form:

$$c_{\alpha\gamma} s_{\gamma\beta} = \delta_{\alpha\beta} \quad \text{with} \quad \alpha,\beta,\gamma \in \{1,2,3,4,5,6\}. \tag{2.8}$$

$\delta_{\alpha\beta}$ denotes the Kronecker delta.

The above-described effects are called principle, because the involved physical quantities $\boldsymbol{E}$, $\boldsymbol{D}$, and $\boldsymbol{T}$, $\boldsymbol{S}$ are from the same domain, electrical and mechanical, respectively. Piezoelectricity describes the crossed effect and links these domains. Starting from the Gibbs free energy

$$G(\boldsymbol{E},\boldsymbol{T}) = U - E_i D_i - T_\alpha S_\alpha, \tag{2.9}$$

the following equations for $\boldsymbol{D}$ and $\boldsymbol{S}$ can be derived [14]:

$$D_i = \varepsilon_{ik}^T E_k + d_{i\alpha} T_\alpha, \tag{2.10}$$

$$S_\alpha = d_{\alpha k} E_k + s_{\alpha\beta}^E T_\beta. \tag{2.11}$$

Tab. 2.1: *Voigt's notation.*

ij or kl	11	22	33	23 and 32	31 and 13	12 and 21
α or β	1	2	3	4	5	6

$d_{i\alpha}$ and $d_{\alpha k}$ are 3×6 and 6×3 matrices, respectively. They are called piezoelectric charge and strain coefficients, and correspond to the direct and converse effects, as described in section 2.1. Owing to the symmetry, the direct and converse piezoelectric coefficients from Eqs. (2.10) and (2.11) are transpose of each other.

The dielectric permittivity and elastic compliance in Eqs. (2.10) and (2.11) have a T and E as superscripts, which stay for the constant mechanical stress and electric field, respectively. In piezoelectric materials, the electric and mechanical properties depend on such constraints and have different values, thus it is important to distinguish them. One differentiates between the *free* electric permittivity ε^T, for which the mechanical stress is held constant ($\mathrm{d}T = 0$), and the *clamped* electric permittivity ε^S, for which the mechanical strain stays constant ($\mathrm{d}S = 0$). Similarly, there are the *open-circuit* ($\mathrm{d}D = 0$) elastic stiffness c^D and compliance s^D, and their *short-circuit* ($\mathrm{d}E = 0$) versions: c^E and s^E.

In total, there are four types of piezoelectric coefficients, which are defined through the following Maxwell relations:

$$d_{i\alpha} = \left(\frac{\partial D_i}{\partial T_\alpha}\right)^E = \left(\frac{\partial S_\alpha}{\partial E_i}\right)^T, \tag{2.12}$$

$$e_{i\alpha} = \left(\frac{\partial D_i}{\partial S_\alpha}\right)^E = -\left(\frac{\partial T_\alpha}{\partial E_i}\right)^S, \tag{2.13}$$

$$g_{i\alpha} = -\left(\frac{\partial E_i}{\partial T_\alpha}\right)^D = \left(\frac{\partial S_\alpha}{\partial D_i}\right)^T, \tag{2.14}$$

$$h_{i\alpha} = -\left(\frac{\partial E_i}{\partial S_\alpha}\right)^D = -\left(\frac{\partial T_\alpha}{\partial D_i}\right)^S. \tag{2.15}$$

The first column defines the direct and the second the converse effect piezoelectric coefficients. Equation (2.12) is derived from Eqs. (2.10) and (2.11), hence from the Gibbs free energy. The other three definitions for the piezoelectric coefficients in Eqs. (2.13) to (2.15) are derived from other thermodynamic potentials, which are obtained from the Gibbs free energy Eq. (2.9) through Legendre transformations [14, 15]. Experimentally, the most relevant coefficients are the piezoelectric charge or strain coefficient $d_{i\alpha}$, measured in the units of $\mathrm{pC\,N^{-1}}$ or $\mathrm{pm\,V^{-1}}$, and the piezoelectric stress coefficient $e_{i\alpha}$, measured in the units of $\mathrm{pC\,m^{-2}}$.

Finally, the relations between the different piezoelectric, elastic, and electric coefficients can be written [15]. The most important are the following:

$$\begin{aligned} e_{i\alpha} &= d_{i\beta} c^E_{\beta\alpha}, \\ \varepsilon^T_{ij} &= \varepsilon^S_{ij} + d_{i\alpha} e_{\alpha j}, \\ c^D_{\alpha\beta} &= c^E_{\alpha\beta} + e_{\alpha i} h_{i\beta}, \\ s^D_{\alpha\beta} &= s^E_{\alpha\beta} + d_{\alpha i} g_{i\beta}. \end{aligned}$$

2.4 Nucleation theory

In a solid, the nucleation theory describes the formation of the thermodynamically stable crystal phase within the metastable one [16]. Thus, the nucleation theory is an important ingredient

within the frame of the direct and reversed transitions from the paraelectric to the ferroelectric or antiferroelectric phases, as described in section 2.1. The nucleation rate is proportional to

$$R \propto \exp\left(-\frac{G_{ij}^*}{kT}\right), \tag{2.16}$$

where k is the Boltzmann constant, T temperature, and G_{ij}^* the thermodynamic energy barrier for the formation of a nucleus of the stable phase within the metastable. These phases are indexed as j and i, respectively. The nucleus, which is schematically depicted in Fig. 2.4 inset, is characterized by its volume V, enthalpy density h_j, and surface to the metastable phase with interface energy γ_{ij}. h_i gives the enthalpy density of the metastable phase. During the formation of the nucleus, the Gibbs free energy of the system changes according to

$$\Delta G = -\left|\Delta h_{ij}\right| V + \beta \gamma_{ij} V^{\frac{2}{3}}, \tag{2.17}$$

where $\Delta h_{ij} = h_i - h_j$ and β is the geometry factor. For instance, for the spherical nucleus $\beta = \sqrt[3]{36\pi}$. Figure 2.4 shows the change of the systems Gibbs free energy with growing nucleus volume according to Eq. (2.17). Through the derivation of Eq. (2.17), the expressions for the critical nucleus volume V^* and thermodynamical barrier G_{ij}^* can be derived:

$$V^* = \left(\frac{2\beta\gamma_{ij}}{3\Delta h_{ij}}\right)^3, \tag{2.18}$$

$$G_{ij}^* = \frac{4}{27}\beta^3 \frac{\gamma_{ij}^3}{\Delta h_{ij}^2}. \tag{2.19}$$

Once the nucleus gains the critical volume and the barrier is overcome, it can grow unstoppably, and the metastable phase eventually transforms into the stable one. According to Eq. (2.19), the thermodynamic nucleation barrier is inverse proportional to the squared enthalpy difference Δh_{ij}. It can be seen as a driving force for nucleation. The greater the difference is, the lower the barrier is, thus higher the transition rate R (Eq. (2.16)). Note that the nucleation can only occur for the stable phase within the metastable, in order to minimize the systems Gibbs free energy, and not *vice versa*.

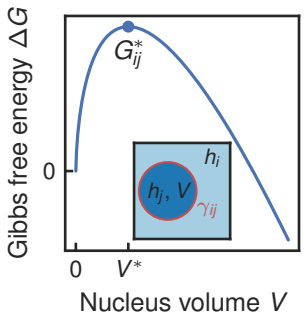

Fig. 2.4: *Change of the Gibbs free energy ΔG with growing nucleus volume V. Inset shows schematically a nucleus of the stable phase within the metastable.*

3 Perovskite-based piezoelectric materials

3.1 Perovskite crystal structures

The most widely used piezoelectric material is lead zirconate titanate, $Pb(Zr_xTi_{1-x})O_3$ (PZT) ceramics [2, 17]. It is a solid solution of lead zirconate and lead titanate and has the perovskite crystal structure. Another important class of piezoelectric materials is relaxors, for instance, $Pb(Mg_{1/3}Nb_{2/3})O_3$. The distinctive characteristics of the relaxors are diffuse phase transitions in temperature. The mixtures of ferroelectrics and relaxors, the relaxor ferroelectrics, exhibit high electrostriction, the quadratic electro-strain effect, which is discussed in section 3.2.2, and have perovskite structure as well. Two of the most prominent examples of relaxor ferroelectrics are $Pb(Mg_{1/3}Nb_{2/3})O_3$-$PbTiO_3$ (PMN-PT) and $Pb(Zn_{1/3}Nb_{2/3})O_3$-$PbTiO_3$ (PZN-PT) [18]. Furthermore, the lead-free piezoelectric materials like potassium-sodium niobate, $K_{0.5}Na_{0.5}NbO_3$ (KNN) [19, 20], barium titanate, $BaTiO_3$ (BT), and bismuth sodium titanate, $Bi_{0.5}Na_{0.5}TiO_3$ (BNT) [21] crystallize in the perovskite structure. In short, the perovskite crystal structure is by far the most important structure in the field of piezoelectric materials. Therefore, it is important to briefly discuss it at this place and later compare it to the fluorite-based HfO_2 and ZrO_2 crystals.

The perovskite structure is named after calcium titanate, $CaTiO_3$, a mineral called perovskite. The perovskite structure is commonly abbreviated as ABO_3. In Fig. 3.1, the green, blue, and red spheres depict A, B, and oxygen atoms, respectively. The large Pb^{2+}, Ba^{2+}, Sr^{2+}, Bi^{3+}, or Ba^{+} cations are typical for the A site. The B site is occupied by the smaller cations, like Ti^{4+}, Zr^{4+}, Nb^{5+}, Zn^{2+}, or Mg^{2+}. Figure 3.1(a) shows the paraelectric cubic crystal phase, which is observed for materials at elevated temperatures. This highly symmetric crystal phase is very prone to elastic distortions, which are subdivided into two categories: tilt and displacive transitions. These transitions occur under decreasing temperature. During the tilt transitions, the oxygen

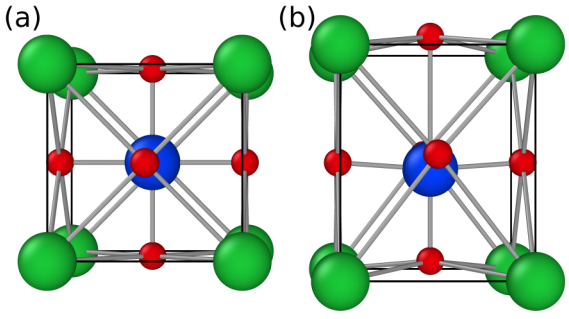

Fig. 3.1: *(a) cubic perovskite structure and (b) its tetragonal ferroelectric distortion. The elongation and atom displacements in (b) are exaggerated for comparability. Concerning the ABO_3 notation, the green spheres depict A atoms, the blue spheres B atoms, and the red spheres are oxygen atoms. The oxygen atoms form the prominent oxygen octahedron in the cubic phase. This nomenclature is also adapted for all its distortions.*

octahedra undergo a collective tilt-rotational motion. This spontaneous distortion (strain) can be accompanied by the spontaneous (remnant) polarization. Depending on whether the material develops the spontaneous polarization or not, it is called either ferroelectric or ferroelastic. In the displacive transition, the constituent atoms of the cubic crystal phase move out of the sites of high symmetry, thus potentially producing ferroelectric or antiferroelectric properties (see section 2.2). The later transition is more relevant for ferroelectric and piezoelectric perovskites.

There are several polar crystal phases that can emerge after the transition from the nonpolar cubic perovskite phase. They differ in the direction of distortion, thus in the polarization direction. For instance, in the tetragonal perovskite structure, as depicted in Fig. 3.1(b), the B cation (blue sphere) is displaced towards one of the oxygen atoms, which leads to the cell elongation along this particular direction and contraction of the two lateral directions. During the transition, the positive partial charge of the B cation and the negatively charged barycenter of the oxygen octahedron are moved apart and the remnant polarization is induced. In total, there are six oxygens, towards which the B cation can be displaced, hence there are six possible polarization directions after the transition into the tetragonal phase. In general, the polarization can be easily reversed or even rotated by 90° under an external electric field. In the orthorhombic crystal phase, the B cation is displaced towards two of its neighboring oxygen atoms along ⟨110⟩ family of directions, hence yielding 12 possible remnant polarization directions. In the rhombohedral crystal phase, the displacement takes place towards three oxygen atoms, which results in eight possible ⟨111⟩-orientations of the remnant polarization. There are also several monoclinic and triclinic perovskite crystal phases with possible 24 $\langle hk0 \rangle$ and 48 $\langle hkl \rangle$ remnant polarization directions, respectively [22].

3.2 Electro-strain effects in perovskite materials

There are four electro-strain effects responsible for the piezoelectric activity in perovskite-based materials. The genuine piezoelectric effect, as described in section 2.1, is only one of them. The three other effects: electrostrictive, domain switching, and volume change effects, are strictly speaking not piezoelectric. Nevertheless, in literature, all of them are often referred to as piezoelectric effects. A particular material can exhibit all of them simultaneously in different proportions.

3.2.1 Genuine piezoelectric effect

The piezoelectric effect is a linear intrinsic (crystalline) effect, which links, for instance, the mechanical strain $\boldsymbol{S}$ and electric field $\boldsymbol{E}$ via third rank piezoelectric strain coefficient tensor $\boldsymbol{d}$. If the Voigt's notation is omitted, the relation is written as follows:

$$S_{ij} = d_{ijk} E_k \quad \text{with} \quad i, j, k \in \{1, 2, 3\}.$$

There are also other definitions for the piezoelectric coefficient, as described in section 2.3. This linear piezoelectric effect is inherent only to crystals possessing a piezoelectric symmetry point group. The advantage of this effect is its linearity and absence of hysteresis in the S–E–diagram. The pure linear piezoelectric effect can be observed in the poled lithium niobate ($LiNbO_3$) single crystal if the driving electric field stays far below the coercive electric field E_c, the field needed for polarization reversal [23]. $LiNbO_3$ single crystals are used, for instance, as a high-frequency transducer in medical imaging applications [24].

3.2.2 Electrostrictive effect

The electrostrictive effect is the second-order intrinsic (crystalline) effect. In contrast to the piezoelectric effect, the electrostrictive effect is observed in all the dielectric materials, regardless of their symmetry point group. However, owing to its general weakness, it is best observed in nonpiezoelectric materials. The electrostriction is described by the fourth rank tensor $\boldsymbol{M}$ or $\boldsymbol{Q}$ as follows:

$$S_{ij} = d_{ijk}E_k + M_{ijkl}E_kE_l,$$
$$S_{ij} = g_{ijk}P_k + Q_{ijkl}P_kP_l \quad \text{with} \quad i,j,k,l \in \{1,2,3\}.$$

The electrostrictive effect is also hysteresis-free. The electrostriction is particularly high in relaxor ferroelectrics, like PMN-PT and PZN-PT [18].

3.2.3 Domain switching effect

Regions in the material with different polarization orientation are called domains. The domains are separated by the so-called domain walls. For a tetragonal perovskite structure, for instance, the typical angles between the polarization directions are 180° (antiparallel arrangement) or nearly 90°. Owing to the elongated form of the tetragonal cell, the angle between the polarization directions for the 90° arrangement is always smaller than 90°. Nevertheless, the domain walls oriented along the ⟨100⟩ and ⟨110⟩ directions are called 180° and 90° domain walls, respectively. An external electric field can force the polarization of domains to rotate and align with it to reduce the interaction energy. This rotation occurs at domain boundaries so that the polarization rotation results in the domain wall motion. While for the 180° domain wall motion, which is a simple flip of the polarization, no significant strain effects are present, the 90° domain walls induce strain in the crystal if they are moved, because the rectangular form of the tetragonal cell is rotated by 90°. The motion of the 90° domain wall is particularly important for the soft PZT [18], which is discussed in section 3.3. The domain switching effect is an extrinsic effect and its disadvantages are nonlinearity and hysteretic activity. Generally, it sets on at elevated electric field magnitudes.

3.2.4 Volume change effect

The material in the antiferroelectric phase can undergo a phase transition to the ferroelectric phase, producing the pinched hysteresis P–E–loop, if an external electric field is applied, as described in section 2.1. During this phase transition, the crystal volume changes, giving rise to the electro-strain effect. Similarly to the domain switching effect, this extrinsic effect is nonlinear and shows a hysteresis in the S–E–diagram. The phase transition occurs also at elevated electric field magnitudes. For instance, the following perovskite structured materials exhibit the volume change effect: $PbZrO_3$ [25], $NaNbO_3$ [26], $AgNbO_3$ [27], and $Pb_xLa_{1-x}(Zr_yTi_zSn_{1-y-z})O_3$ (PLZTS) [28].

3.2.5 Strain hysteresis loops

In comparison to a nonpolar material, the piezoelectric behavior of a ferroelectric material is complicated by the presence of the remnant polarization. During the polarization reversal, the piezoelectric coefficient also changes its sign [29]. Consider a ferroelectric single crystal. Figure 3.2(a,c) depicts its polarization and strain hysteresis loops, respectively. In the following will

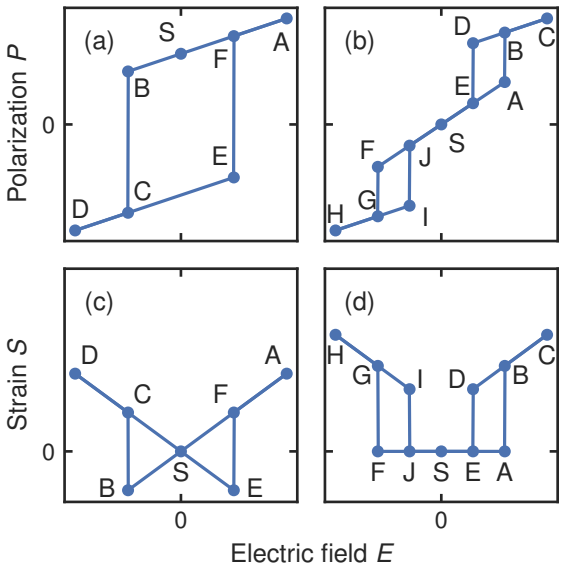

Fig. 3.2: *(a) polarization and (c) strain hysteresis loops for a ferroelectric material. During the electric field cycling, the traversed path is $S \rightarrow A \rightarrow B \rightarrow C \rightarrow D \rightarrow E \rightarrow F \rightarrow A \rightarrow B \rightarrow$, and so on. (b) and (d) depict the polarization and strain hysteresis loops for an antiferroelectric material, respectively. The traversed path is $S \rightarrow A \rightarrow B \rightarrow C \rightarrow D \rightarrow E \rightarrow F \rightarrow G \rightarrow H \rightarrow I \rightarrow J \rightarrow A \rightarrow B \rightarrow$, and so on.*

be described, how the so-called butterfly loop, the strain hysteresis loop, which is characteristic for the ferroelectric materials, is formed. Starting at zero electric field in point S, the crystal has positively oriented remnant polarization. At this point, its strain state is set to zero for the reference. The increasing electric field towards point A causes the polarization and strain to increase linearly. The slopes define the dielectric permittivity ε and piezoelectric strain coefficient d. In point A, the maximum polarization and tensile strain are achieved. In the next step, the electric field starts to decrease towards the negative values. With a negative electric field, the strain becomes also negative (compressive strain) up to point B. In point B, where the coercive electric field is achieved, the polarization switches abruptly its sign. This abrupt change is due to the considered single crystal. At the coercive electric field, the strain also changes its sign and becomes tensile, because d changes its sing. However, the strains in points B and C have the same magnitude. Furthermore, point B marks the highest achievable compressive strain. After the polarization reversal, the electric field is further reduced up to the largest negative field in the point D. At this point, the strain reaches once more its maximum tensile value, the same value as in point A. Now, the electric field starts to increase. At the positive coercive electric field in point E, the polarization changes its sign once more. At this point, the same compressive strain state is achieved as in point B, which then abruptly becomes tensile in point F. Finally, the electric field and strain reach their maximal values in point A, thus closing the loop. Note that the maximal tensile strain (points A and D) is greater in magnitude than the compressive strain (points B and E). Furthermore, if the electric field never exceeds the coercive field during the cycling, the single crystal either expands (line BF) or contracts (line CE), depending on the remnant polarization orientation.

Figure 3.2(b,d) shows the polarization and strain hysteresis loops, respectively, for centrosym-

metric antiferroelectric material in which the ferroelectric phase is induced. Again, for the purpose of discussion, an antiferroelectric single crystal is considered. Starting from point S, the zero electric field starts to increase. At low electric fields, the crystal is in its antiferroelectric phase, which is centrosymmetric, thus no strain response is observed. At the point A, where the critical electric field is achieved and the transition to the ferroelectric phase occurs, the abrupt jump in the polarization to the point B takes place due to the emerging remnant polarization. Synchronously, the strain changes, because of two effects. Firstly, owing to the ferroelectric, thus piezoelectric, phase, the crystal expands piezoelectrically. The second effect is the crystal volume change during the phase transition, as described in section 3.2.4. The further increase of the electric field leads to the maximum polarization and tensile strain in point C. The linear increase of the strain is solely attributed to the piezoelectric effect. Then, the electric field starts to decline, so the polarization and the strain. In point D, in which another critical value for the electric field is reached, the ferroelectric phase transitions back to the antiferroelectric phase. The remnant polarization vanishes and only the induced polarization remains in point E. The tensile strain vanishes, because of the centrosymmetry of the antiferroelectric phase. Furthermore, the crystal volume also shrinks back. When the electric field passes the zero value, the positive half of the polarization and strain loop is complete. For the negative electric field values, the second half of the loop with negative polarization values is traversed. Owing to the negative remnant polarization, the piezoelectric strain coefficient changes its sign. Therefore, the second half of the strain loop is oriented upwards, thus the strain is also tensile. Note that generally, the dielectric permittivities of the ferroelectric and antiferroelectric phases are different. Accordingly, the slopes of the lines CD and HI in the ferroelectric phase are different from the slope of the line AF in the antiferroelectric phase.

A comparison of the strain hysteresis loops of the ferroelectric and antiferroelectric materials (Fig. 3.2(c-d), respectively) gives the following insights. The antiferroelectric material produces always the tensile strain, while for the ferroelectric material also the compressive strain is possible. The strain response to a varying small electric field in the ferroelectric material is linear. For the antiferroelectric material, the strain emerges only at phase transition in an abrupt, stroke-like manner. Furthermore, the maximal strain values which can be achieved are higher for the antiferroelectric material. Note the apart from the sign equal slopes in the linear regions in (c) and (d). Here, the piezoelectric strain coefficients are intentionally chosen to be equal for the purpose of discussion. The extra strain (compare the points A and D in (c) with the points C and H in (d)) is due to the crystal volume change during the phase transition.

The strain hysteresis loops in Fig. 3.2(c-d) are idealistic. In the real polycrystalline materials, the sharp edges are smoothed due to the polycrystalline nature and further effects like domain wall movement (section 3.2.3), however, the overall form of the loops is still valid. Note that these strain hysteresis loops are observed not only in perovskite-based materials but in any ferroelectric or antiferroelectric materials. To sum up, the ferroelectric materials can exhibit linear electro-strain activity with moderate values for the strain. The antiferroelectric materials, however, show highly nonlinear, stroke-like electro-strain activity with high strain values. Depending on the application, both behaviors, thus materials, are desired.

3.3 PZT, a lead-containing perovskite-based material

PZT is the example of piezoelectric perovskite structured materials. It is a solid solution of $PbZrO_3$, an antiferroelectric, thus not piezoelectric material, and $PbTiO_3$, which has piezoelectric properties,

however is not commercially interesting for piezoelectric applications. These two constituents are perfectly solvable in each other over the whole range of concentrations, and the mixture possesses, surprisingly, excellent dielectric, elastic, and piezoelectric properties. Although PZT has been known since 1952 [30], there is still no agreement among researchers on the root cause of the enhanced material properties.

The most prominent feature of the $Pb(Zr_xTi_{1-x})O_3$ systems is the morphotropic phase boundary (MPB) in the phase diagram. With changing composition x, the system crystallizes in different crystal phases. The MPB describes the boundary between the rhombohedral and tetragonal phases around $x = 0.55$ [17]. The dielectric and piezoelectric properties are particularly enhanced at this composition, however it is still debated, what is the exact mechanism behind the MPB. Furthermore, MPB is almost temperature independent, which leads to stable material properties over a wide range of temperatures.

The material properties of perovskite structured materials in general and PZT in particular can be further improved or adjusted for certain applications by doping and additives admixture. In that way, soft and hard PZTs can be manufactured. The former one has higher dielectric and piezoelectric coefficients, and lower coercive electric field than the later one, however, the disadvantage of the soft PZT is its electromechanical hysteresis. The piezoelectric charge coefficient d_{33} for soft and hard PZT is 750 and 250 $\mathrm{pC\,N^{-1}}$, respectively [18].

3.4 Lead-free perovskite-based materials

During the Second World War, the ferroelectricity and piezoelectricity were discovered in BT. Ironically, the first piezoelectric perovskite-based material was lead-free. However, the lead-free BT-, BNT-, and KNN-based piezoelectric materials could not compete with PZT-based and relaxor-based ferroelectrics, because of their inferior piezoelectric properties. Only with the enaction of environmental regulations by the European Union [3, 4] the interest for research of lead-free piezoelectric materials was revived, which lead to new discoveries. For instance, the piezoelectric coefficient d_{33} of 416 $\mathrm{pC\,N^{-1}}$ was reported for a KNN-based system in 2004 [20], which is similar to PZT-based materials. Further information on lead-free perovskite-based materials research can be found in the extensive review articles [1, 31, 32].

4 $Hf_{1-x}Zr_xO_2$ material system

4.1 Applications

HfO_2 and ZrO_2 material systems have been studied and used for decades [33, 34]. For instance, HfO_2 is used as dielectric material (high-κ material) in CMOS technology for field effect transistor (FET) gate insulators [35] and dynamic random access memory capacitor insulators [36]. ZrO_2 doped with Y, also known as yttria-stabilized zirconia, is used in oxide fuel cells [37]. Nevertheless, in 2011, ferroelectricity was discovered in Si-doped HfO_2 [5] and in oxides solid solution $Hf_{0.5}Zr_{0.5}O_2$ (HZO) [6]. Since then, the community of researchers from around the world working on the HfO_2- and ZrO_2-based systems has steadily grown, as the ferroelectric behavior in these materials opens new possibilities for applications.

The two most prominent devices for digital electronics comprising a ferroelectric insulator are ferroelectric field effect transistor (FeFET) and ferroelectric random access memory (FeRAM). Owing to the remnant polarization, these nonvolatile ferroelectric devices can retain their state: "off"/"on" and "0"/"1", respectively, also after power supply removal. The HfO_2-based FeFETs produced with 28 and 22 nm technologies [38–40] show the potential of the HfO_2 and ZrO_2 material systems for FeFET [8] and FeRAM [7, 41]. Another digital device, in which ferroelectric $Hf_{1-x}Zr_xO_2$ can be used, is ferroelectric tunnel junction [42, 43]. In this device, the tunnel current through a thin ferroelectric layer encodes the "0" or "1" state, because the current magnitude depends on the remnant polarization of the ferroelectric layer.

Recently, another field of application arose for the ferroelectric $Hf_{1-x}Zr_xO_2$. For a FET, an essential primitive building block of today's semiconductor industry, which acts as a switch with clearly distinct "on" and "off" states, there is a fundamental limit for how efficient the current flow through the channel can be blocked with the gate voltage. At the temperature of 300 K, the gate voltage must be increased by 60 mV in order to decrease the current through the channel by the factor of ten. This fundamental limit is also called the Boltzmann's tyranny. It puts the lower limit on the dynamical power consumption of FET. In 2008, a modification to the FET was proposed in order to overcome this limit. If the ferroelectric instead of the dielectric material is used for the gate insulator, then the electrostatic potential directly at the channel causing the current seizing is amplified with respect to the actually applied gate voltage [44]. This effect is due to the negative differential capacitance, which in literature is often simply called the negative capacitance (NC), which can arise in a ferroelectric material. It can be explained within the frame of the LGD model. The differential capacitance is defined as a derivative of the polarization with respect to the electric field and its negative value is depicted by the blue line around zero electric field in Fig. 2.3(a). $Hf_{1-x}Zr_xO_2$, being CMOS-compatible material, is a good candidate for the NC applications. Recently, the stabilization of the NC state was achieved experimentally using HZO [45, 46]. For clarity, utilizing the NC of ferroelectric materials in FETs has an aim to improve their efficiency and reduce the dynamic power consumption. Such a device still remains volatile, in contrast to FeFET.

$Hf_{1-x}Zr_xO_2$ material systems also exhibit piezo- and pyroelectric, and electrocaloric effects.

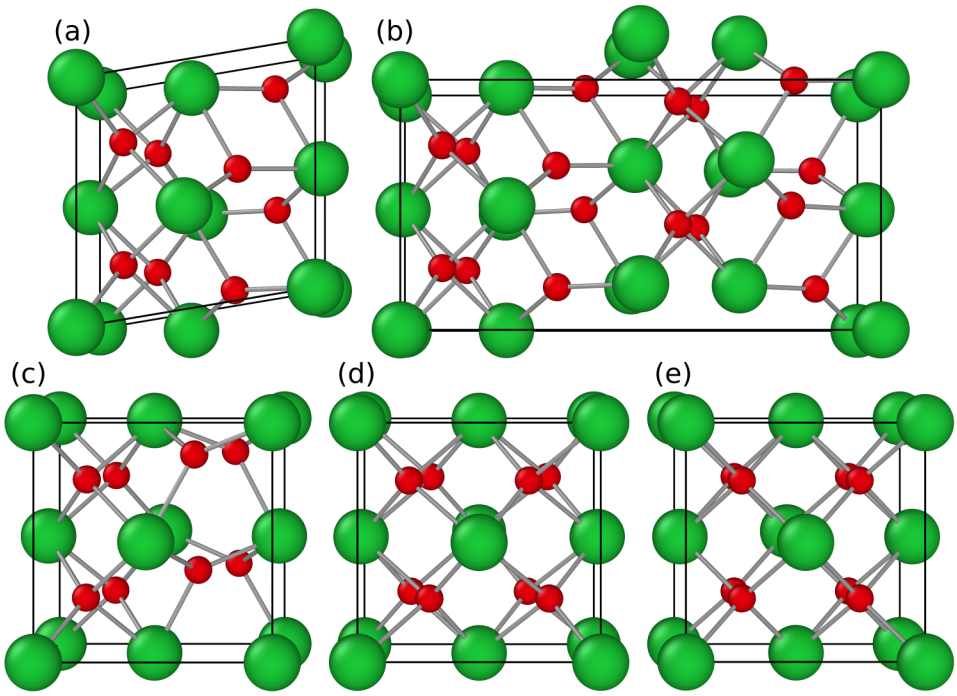

Fig. 4.1: *Structure of HfO_2 and ZrO_2 crystal phases: (a) the monoclinic $P2_1/c$, space group #14, (b) the orthorhombic Pbca, space group #61, (c) the polar orthorhombic $Pbc2_1$, space group #29, (d) the tetragonal $P4_2/mnc$, space group #137, and (e) cubic $Fm\bar{3}m$, space group #225. The green and red spheres are metal and oxygen atoms, respectively.*

The piezoelectric effect in $Hf_{1-x}Zr_xO_2$ is discussed in section 4.4. The electrocaloric effect is the physical inverse of the pyroelectric effect. They both, similar to the direct and converse piezoelectric effects (see section 2.3), are crossed effects and link the electrical and thermal domains. The pyroelectric effect describes the change of the remnant polarization with changing temperature. The pyroelectric $Hf_{1-x}Zr_xO_2$ can be utilized for thermal sensor and energy harvesting applications [47–53].

4.2 Fluorite crystal structures

HfO_2 and ZrO_2 are chemically very similar oxides and have the same crystal phases. At standard conditions, both HfO_2 and ZrO_2 bulk crystals form the monoclinic (m) phase with space group #14 and international symbol $P2_1/c$. At approximately 1900 K, the HfO_2 m-phase transitions to the tetragonal (t) $P4_2/mnc$ phase with space group #137. Then, at approximately 3000 K the t-phase transitions to the cubic (c) $Fm\bar{3}m$ phase with space group #225. For ZrO_2, these transition temperatures are 1300 and 2800 K, respectively. [54]. Furthermore, at low temperatures, the m-phase of HfO_2 and ZrO_2 transitions to the high pressure orthorhombic (o) *Pbca* phase (space group #61) at approximately 11 and 10 GPa, respectively [55, 56]. All these phases, depicted in Fig. 4.1(a,b,d,e), have a center of symmetry and are not polar, thus they do not possess the remnant polarization. In literature, HfO_2 and ZrO_2 are also termed as fluorite like, because of the structure of the c-phase, which resembles the structure and space group of the mineral fluorite, CaF_2.

The ferroelectricity in HfO_2 and ZrO_2 originates from the polar orthorhombic (p-o) $Pbc2_1$ phase (space group #29) [57], whose structure is depicted in Fig. 4.1(c). Interestingly, this crystal phase was already reported in 1989 [58], however, the electric characterization was not performed then, so that the ferroelectric properties were not unveiled until 2011 [5, 6]. There are also other crystal phases, including polar phases, which were theoretically predicted or experimentally found [59, 60]. However, these phases have either high energy in comparison to the low energy m-, o-, p-o, and t-phases, or the experimental conditions under which they occur are extreme, thus of no interest for applications.

Only a few hundred meV energy is needed, to substitute one Hf with one Zr atom in HfO_2 and *vice versa* [61]. This gives an explanation on the atomistic level, why HfO_2 and ZrO_2 mix well and form the solid solution $Hf_{1-x}Zr_xO_2$ with any composition parameter x [62]. If Hf and Zr atoms are mixed, for instance, in the m-phase, the number of space group symmetries is reduced, obviously, so that the crystal phase of the mixture is not $P2_1/c$ anymore. Nevertheless, it is still denoted as the monoclinic.

The direct comparison of the crystal phases of the perovskite-based (ABO_3) and fluorite-based (MO_2) materials shows that the former can adopt several polar phases with multiple polar axes, while the latter has only one relevant polar crystal phase, the p-o phase. Technically, the MO_2 c-phase (Fig. 4.1(e)) can be considered as the paraelectric phase, similar to the cubic phase of ABO_3 (Fig. 3.1(a)). However, owing to the crystal phase energies, the t-phase in MO_2 is more suitable for this role. The p-o-phase in MO_2 (Fig. 4.1(c)) is then the counterpart of the tetragonal phase in ABO_3 (Fig. 3.1(b)). They both have one six-fold polarization axis along ⟨100⟩-direction.

4.3 Ferroelectricity in $Hf_{1-x}Zr_xO_2$

The crystal phase geometries and their total energies can be calculated with density functional theory (DFT) [63, 64]. DFT calculates the ground state of a molecule or crystal at 0 K through the minimization of the energy functional, which is a function of the electron density. The quantum mechanical effects of the pairwise electron exchange and their correlation are considered in the exchange-correlation (XC) functional. The better this functional is, the better is the approximation for the ground state of the system. Indeed, if the XC term is exact, then the calculated ground state is also the true one. However, the exact XC term is not known. For instance, two very simple approximations can be made for it: the local density approximation (LDA) [65], in which only the electron density is accounted for, and the generalized gradient approximation (GGA) [66], which additionally takes into account the gradient of the electron density. It is well known that the LDA underestimates the geometry (lattice constants for crystals) and the GGA overestimates it. More sophisticated XCs exist, however, they are also more demanding in computing power.

Figure 4.2(a-c) shows the calculated total energies E_{tot} for the crystal phases of HfO_2 and ZrO_2 in reference to the corresponding m-phase using three approximations for XC functional: LDA, GGA, and for solids modified version of GGA [67]. The m-phase is the phase of the lowest energy for both materials across all used XC functionals. This corresponds to the experimental finding that the monoclinic phase is the ground phase in these materials. However, for the temperatures other than 0 K, the free energy $F(T) = E_{tot} - TS(T)$ needs to be considered instead of the E_{tot}. At elevated temperatures, the free energy of the high symmetric t- and c-phases is reduced [69], so that with rising temperature, first the t-phase becomes the lowest one in the free energy $F(T)$, and then the c-phase, in accordance with the experimental observations, as described in section 4.2. For the

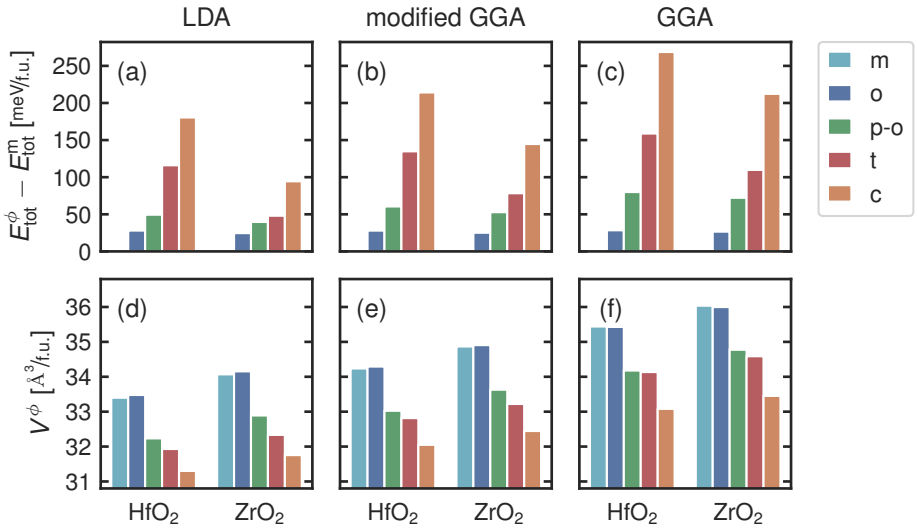

Fig. 4.2: *DFT values for the total energies (a-c) and volumes (d-f) of HfO_2 and ZrO_2 crystal phases for three different XC functionals: LDA, modified GGA, and simple GGA. The total energies are referenced to the corresponding m-phase total energy (m-bars have zero height). The calculations were performed with FHI-AIMS code [68].*

experimentally observed ferroelectricity in the $Hf_{1-x}Zr_xO_2$ material system [49, 70], the p-o-phase, which has the third-lowest energy among other crystal phases (Fig. 4.1(a-c)), needs to be stabilized. In literature, there are several mechanisms discussed, which can cause this stabilization. In the following, these are presented.

The thickness of the manufactured $Hf_{1-x}Zr_xO_2$ samples plays an important role in the ferroelectric properties. Experimentally, the p-o-phase is found to be stable in thin films with thicknesses of several tens of nm. This effect is called size effect in $Hf_{1-x}Zr_xO_2$ material systems [71]. On the contrary, in the perovskite-based materials, the ferroelectric properties are observed only in thick films. This gives the fluorite-based materials an advantage for thin-film applications. Nevertheless, the ferroelectricity was also demonstrated in 390 nm thick ZrO_2 [72] and 930 nm thick Y-doped HfO_2 [73] films, showing also the potential for these materials as a competitor to perovskite-based materials in thick film applications.

Ferroelectric $Hf_{1-x}Zr_xO_2$ films can be manufactured by means of atomic layer deposition (ALD) [5, 6, 62, 74–81], chemical solution deposition (CSD) [72, 82–85], chemical vapor deposition [86], physical vapor deposition (PVD) [87–90], and pulsed laser deposition (PLD) [73, 91, 92]. Normally, the material is deposited on the bottom electrode and then covered by the top electrode, forming a metal-insulator-metal structure (capacitor), which allows the electric characterization. All these deposition techniques, except for the last one, produce amorphous films, which are then crystallized to polycrystalline structures through a rapid annealing step. In contrast, the PLD is an epitaxial growth technique and produces single-crystal films. The polycrystalline films consist of nanoscaled grains, whose size is limited by the film thickness. Owing to the strain conditions originating, for instance, from the electrodes [5, 93–96], and grain interfaces [69–71, 97], the Gibbs free energy of the film system as a whole can be significantly altered, thus potentially stabilizing the p-o-phase.

The ferroelectric properties of the $Hf_{1-x}Zr_xO_2$ material system can also be promoted with doping. Experimentally was shown, that dopants such as Si [5, 98], Zr [6, 62], Y [74, 82, 87, 89, 92], Al [75], Gd [76, 77], Sr [78], La [79, 80, 99], Ge, Sc, Nb [89], and N [88, 89] can enhance the ferroelectricity in HfO_2 utilizing different growth techniques like ALD, CSD, PVD, and PLD. Compared to this, the doping of ZrO_2 is experimentally less studied. Only CSD grown ZrO_2 films with the following doping were considered so far: Mg, In, La [85], Ce, Ti, Sn [100], and Y [85, 100]. There are also several theoretical (DFT) studies for doped HfO_2 with dopants like Sr [101], Al, Y [102], La [102, 103], C, Ge, Ti, Sn, Zr, Ce [61], and Si [61, 103, 104]. In the aforementioned studies, for the Sr, Al, Y, and La doping, the oxygen vacancies are also considered. Nearly 40 species from the fourth, fifth, and sixth periods of the periodic table of elements are also investigated as dopants for HfO_2 in a high-throughput approach study [105]. Surprisingly, the doped ZrO_2 has not been considered from the theoretical point of view at all, until the recent screening study with 58 dopants, mainly from the first 15 groups in the periodic table of elements [106]. This latest screening study also considers all the 58 dopants for HfO_2.

In all these theoretical studies, the effect of the dopant atom on the crystal phase energies is investigated with the objective to significantly decrease the energy of the p-o-phase. Si doping, which is the most theoretically studied doping in HfO_2, is a good example of showing, how tedious are these DFT investigations of doped HfO_2 and ZrO_2. Künneth *et al.* show in their study that substitutional Si doping in HfO_2 slightly decreases the energy of the p-o-phase, however, not sufficiently enough to stabilize it over the m-phase [61]. Performing a larger set of calculations and considering the statistics, Falkowski *et al.* show that the energy of the p-o-phase is almost insensitive to the Si doping and the decrease reported in the previous study is an artifact, which is attributed to the doping density anisotropy [103]. Only Dutta *et al.* in their recent study managed to show that certain layered Si doping arrangements can stabilize the p-o-phase over the m-phase [104]. This demonstrates that such doping arrangements may play an important role in stabilizing the p-o-phase and thus the ferroelectricity in HfO_2, however, the question remains open, how often such doping arrangements appear in experiments.

One another mechanism for ferroelectricity stabilization in $Hf_{1-x}Zr_xO_2$ is proposed to be due to the crystallization process of thin films. During the crystallization at elevated temperatures, the as-deposited amorphous material first forms the high symmetric t-phase through nucleation (section 2.4). During the rapid cooling, the p-o-phase is nucleated withing the t-phase in the second step. However, this phase is thermodynamically metastable, as the energy of the m-phase is lower. The further decay into the m-phase is suppressed, due to the high thermodynamic barrier for the formation of the m-phase nuclei [107]. This model is supported by the experiments, which show that after the second anneal treatment, a ferroelectric film with a high proportion of the p-o-phase does decay into the thermodynamically stable m-phase and the ferroelectric properties vanish. Another dynamic process, which is discussed in the literature as an important ingredient for the stabilization of the p-o-phase, is the kinetic phase transitions. In contrast to the nucleation model with small nuclei, the kinetic model assumes the phase transitions of larger crystal regions, which proceeds collectively [108].

4.4 Antiferroelectricity and piezoelectricity in $Hf_{1-x}Zr_xO_2$

The antiferroelectric-like behavior in $Hf_{1-x}Zr_xO_2$ manifests itself as the experimentally measured double hysteresis loop. For instance, the double hysteresis loop is observed in the Si-doped HfO_2

[5] and $Hf_{1-x}Zr_xO_2$ with x close to 1, particularly in the pure ZrO_2 [62]. As described in section 2.1, the atomistic origin of the antiferroelectricity in a crystal is the alternating arrangement of the electric dipoles. The o-phase is suggested to be the antiferroelectric phase in $Hf_{1-x}Zr_xO_2$ [53], however, this phase occurs at elevated pressure conditions. The common explanation of the antiferroelectric-like behavior in this material system is the electric field induced phase transition from the paraelectric t-phase into the ferroelectric p-o-phase [109], similarly to the perovskite antiferroelectrics (section 3.2.4). As discussed in section 4.3, the t-phase is not stable at room temperature. Thus, the objective of the stabilization of the antiferroelectricity in $Hf_{1-x}Zr_xO_2$ is to stabilize the t-phase over the m-phase. Additionally, the p-o-phase must be inducible from the t-phase via the electric field, which means in the first approximation that the energy difference between these two phases must be surmountable. As depicted in Fig. 4.2(a-c), the t-phase energy for ZrO_2 is lower than for HfO_2. This point makes ZrO_2 in general more suitable for antiferroelectric applications.

The piezoelectric $Hf_{1-x}Zr_xO_2$ material system has the potential to be used in applications like actuators, resonators, sensors, transducers, etc. It appears that this property of the material system is the less studied so far. Recently, piezoelectric coefficients $d_{33} = 19.8\,\mathrm{pm\,V^{-1}}$ and $d_{31} = -11.5\,\mathrm{pm\,V^{-1}}$ for Si-doped HfO_2 were published [110, 111]. For undoped and Mg-doped ZrO_2, piezoelectric coefficient $d_{33} = 10\,\mathrm{pm\,V^{-1}}$ was reported [72, 85]. The authors of these reports state that the mechanism for the piezoelectric activity in their cases is the crystal volume change during the electric field induced transition from the t-phase to the p-o-phase. As depicted in Fig. 4.2(d-f), the crystal volume is smaller for the t-phase in comparison to the p-o-phase. Such an effect is also observed in the perovskite-based piezoelectrics (section 3.2.4). Falkowski *et al.* discuss in-depth the piezoelectric activity in HfO_2 and ZrO_2 and propose doping for its optimization [106]. The domain switching effect (section 3.2.3) can also be important for the piezoelectric activity in $Hf_{1-x}Zr_xO_2$, which has not been investigated yet. However, the kinetic energy barrier for the 90° polarization rotation in the fluorite structure is expected to be higher than in the perovskite structure, thus less probable.

5 Publications

As this dissertation is publication based, in the following the summary and highlights of the two respective articles are given. Furthermore, the authors' contributions to these articles are stated. The articles themselves are attached as copies in the appendix of the dissertation.

5.1 Unexpectedly large energy variations from dopant interactions in ferroelectric HfO_2 from high-throughput ab initio calculations

Max Falkowski, Christopher Künneth, Robin Materlik, and Alfred Kersch
npj Comput Mater **4**, 73 (2018)
DOI: 10.1038/s41524-018-0133-4

5.1.1 Summary

This article deals with the spatial energy fluctuations due to doping density inhomogeneities in four HfO_2 crystal phases: monoclinic, orthorhombic, polar orthorhombic, and tetragonal. La and Si dopants are chosen for the investigation as substitutions for Hf. Furthermore, the oxygen vacancies for the charge compensation of III-valent La on the site of IV-valent Hf are also considered. Moreover, mixtures of different La and Si defects are investigated, which has not been done so far. It is shown that the separate effect of doping species such as La and Si on the crystal phases can be superimposed if the dopants are mixed.

The article is based on a vast collection of DFT calculations of doped HfO_2 structures and their statistics. The approach for the generation of this statistics is best explained in an example. Consider, for instance, a 96-atomic supercell of HfO_2. It is approximately $1 \times 1 \times 1$ nm^3 in size and consists of 32 formula units (f.u., one Hf plus two O atoms), thus there are 32 sites for a doping atom. Putting two doping atoms in 96-atomic supercell results in 6.25 f.u.% doping concentration. There are $32 \times 31 = 992$ possible two-atomic dopant arrangements. Owing to the crystal symmetries, this number can be reduced down to several tens of arrangements. The exact number depends on the number of symmetries, thus crystal phase, and whether the two doping atoms are indistinguishable (Si − Si) or not (Si − La). Each doping arrangement produces a new value for the total energy. Therefore, at the constant concentration of 6.25 f.u.%, a coarse-grained 1 nm^3 region is subjected to energy variation. This is the first cause of the energy variations stemming from the doping. The second cause is the spatial doping concentration variation. Statistically, doping atoms may appear more often in one coarse-grained region than in others. However, the averaged doping concentration over large regions stays constant.

These energy fluctuations are then linked to the different growth processes of doped HfO_2 such as ceramics, ALD, and CSD. The first one, in contrast to the latter two, is a process with a large thermal budget, meaning that the crystallization is performed at high temperatures for long periods of time. It is assumed that under these conditions only the lowest energy state or states close to it are achieved. Therefore, the doping inhomogeneities and energy fluctuations are expected to be rather small in ceramics. On the contrary, the ALD and CSD crystallization process is short in time and performed at moderate temperatures. Under these conditions, the doping concentration fluctuations and their arrangements may withstand the crystallization and produce fluctuating energy landscape with tetragonal nanoregions within the polar orthorhombic phase of Si-doped HfO_2 as depicted in Article-Fig. 1. These energy fluctuations can explain the experimentally observed Curie temperature broadening in the transition from the tetragonal to the polar orthorhombic phase.

The energy fluctuations due to the doping can be of particular interest for the antiferroelectric-like behavior, thus the piezoelectric activity of doped HfO_2 and ZrO_2, which was not discussed in

the article. Within the frame of the nucleation theory (section 2.4), these fluctuations can produce locally high energy differences between the thermodynamically stable and metastable phases, which leads to high thermodynamic forces for the nucleation. Therefore, such nanoregions can natively function as nuclei of the tetragonal to polar orthorhombic phase transition and backward, which is the basis for the piezoelectric activity in HfO_2 and ZrO_2 systems.

5.1.2 Individual contributions

Max Falkowski and Alfred Kersch designed the study and the methodology for the article. Max Falkowski performed the DFT calculations of the doped structures. For this purpose, scripts were written in Python for the setup of the geometries, filtering the symmetry equivalent geometries, submitting the calculations to compute clusters, and checking of calculation completeness. Max Falkowski performed then the in-depth analysis of the simulations. The significant structure deformations and phase transitions were filtered out; the analysis results were displayed in comprehensive figures for discussion. All the authors took part in the discussion. Max Falkowski also designed and produced the final figures for the article. All the authors worked on the manuscript text, while Max Falkowski wrote the majority of it.

5.2 Optimizing the Piezoelectric Strain in ZrO_2- and HfO_2-Based Incipient Ferroelectrics for Thin-Film Applications: An Ab Initio Dopant Screening Study

Max Falkowski and Alfred Kersch
ACS Applied Materials & Interfaces **2020** *12* (29), 32915-32924
DOI: 10.1021/acsami.0c08310

5.2.1 Summary

This article deals with a vast DFT screening study of doped HfO_2 and ZrO_2. 58 dopants from groups 1–15 and periods 1–6 of the periodic table of elements plus Ce and Yb are examined herein. Two defect incorporation types are considered: metal (Hf or Zr) substitution and interstitial; in four crystal phases: monoclinic, orthorhombic, polar orthorhombic, and tetragonal. For each doping species, the total energies of calculated structures with substitutional and interstitial defects are set into relation to calculate the relative formation energy, which allows deducing, which of the incorporation types is more favored. The first interesting insight is that the dopant incorporation type depends to a large extent on the doping atom itself, the host material (HfO_2 or ZrO_2), crystal phase, and doping concentration are rather irrelevant. The relative formation energy is dependent on the oxygen chemical potential during the crystallization process. Therefore, adjusting the oxygen chemical potential, for instance, using oxygen plasma instead of ambient oxygen, the interstitial incorporation type can be suppressed in favor of the substitution.

Depending on how a dopant influence the total energy of HfO_2 and ZrO_2 crystal phases, its potential to promote material characteristics such as ferroelectricity, antiferroelectricity, and tetragonality (for high-κ applications) can be deduced. For instance, if the energy of the polar orthorhombic phase significantly reduces with increasing doping concentration, it means that this doping species improve ferroelectric characteristics. Similar criteria are then developed for the antiferroelectric and high-κ characteristics. La doping, being well studied both experimentally and theoretically, is known as a good ferroelectricity promoter in HfO_2. Thus, La is chosen to be the link between the theoretical results of the current study and the experiments. It defines the scale for doping effect significance on the aforementioned material characteristics. One of the two main results of the current article is the overview of dopants in HfO_2 and ZrO_2 for enhancement of the following material properties: ferroelectricity, antiferroelectricity, and tetragonality depending on the oxygen supply condition during the manufacturing process. This is the first study at all, which investigates the doped ZrO_2 from the theoretical point of view with this large amount of doping species.

As described in section 4.4, the prerequisite for the large piezoelectric activity in HfO_2 and ZrO_2 is their antiferroelectric-like behavior. The dopants, which promote the antiferroelectricity, are then investigated regarding their effect on the piezoelectric activity in HfO_2 and ZrO_2. The second main result of the article is the overview of the piezoelectric coefficients for these doped material systems. For this purpose, the crystal volumes of the doped tetragonal and polar orthorhombic phases are evaluated from the DFT calculations. It is shown and discussed that ZrO_2 is natively more suitable for the piezoelectric application than HfO_2. Its characteristics are then further improved via doping.

Finally, the calculated piezoelectric coefficients of doped HfO_2 and ZrO_2 are compared to the

few experimentally measured coefficients, which are found to be in a good agreement. Moreover, the piezoelectric characteristics of HfO_2 and ZrO_2 material systems are critically compared with other materials like AlN, PZT, and lead-free perovskite-based materials.

5.2.2 Individual contributions

Max Falkowski was solely responsible for conducting the DFT calculations. Using Python, he developed the XRD filter for effectively filtering out the significant structure deformations and phase transitions, which occasionally happen during geometry relaxation of doped structures. He analyzed the produced raw data and prepared comprehensive figures for discussion. The results were discussed with Alfred Kersch in full depth. Max Falkowski designed and prepared the final figures for the article. The manuscript was written by both authors, while the majority of text stems from Max Falkowski.

6 Summary, conclusions and outlook

The discovery of the ferroelectricity in Si-doped HfO_2 and HZO in 2011 opened wide application opportunities for the $Hf_{1-x}Zr_xO_2$ material system. Being a CMOS technology compatible material system, it is of high interest for the semiconductor industry as a gate insulator in nonvolatile memory (FeRAM) and logic (FeFET). $Hf_{1-x}Zr_xO_2$ also exhibits pyroelectric and piezoelectric characteristics, thus allowing applications like energy harvesting, sensing, etc. The fact that $Hf_{1-x}Zr_xO_2$ is lead-free, gives to this material system another large advantage in times of strict environmental regulations against hazardous materials like lead. This advantage is particularly important for the piezoelectric applications because these are vastly dominated by the lead-containing perovskite-based materials like PZT. Depending on the application, certain crystal phases such as the polar orthorhombic $Pbc2_1$ or tetragonal $P4_2/mnc$ need to be stabilized over the thermodynamically stable monoclinic $P2_1/c$. While in the last decade huge progress has been done in understanding of mechanisms and effects for phase stabilization, there is still plenty of topics for research on this highly promising material system.

This dissertation is based on two articles and deals primarily with the piezoelectric activity in HfO_2 and ZrO_2. However, these articles are not solely devoted to the piezoelectricity. Other important aspects of these material systems, like ferroelectric characteristics, are also investigated. The first article [103] from year 2018 deals with the energies of the doped HfO_2 crystal phases and their spatial variations. Si and La were chosen as dopants for this article because these two dopants are well investigated in experiments. La is known to be a good enhancer of ferroelectricity in HfO_2. Si, depending on its concentration, can promote either ferroelectricity or antiferroelectricity. At concentrations beyond 6%, the tetragonal phase is stabilized in Si-doped HfO_2. The main objective of this paper was to better understand the effects of these dopants. The found spatial energy variations of the crystal phases give an explanation for the experimentally observed Curie temperature T_C broadening in the tetragonal to polar orthorhombic phase transition in Si-doped HfO_2 [112]. These variations introduce nanoregions of the tetragonal phase within the polar orthorhombic in the material, which undergo the phase transition at different T_C, thus the broadening. This broadening makes up the pyroelectric activity in this system. In the frame of the current dissertation, this nanoregions can constitute the nucleation centers for the aforementioned phase transition, which is then important for the piezoelectric activity.

The second article [106] from year 2020 deals not only with piezoelectric, but also with ferroelectric, antiferroelectric, and high-κ characteristics of doped HfO_2 and ZrO_2. In total, 58 dopants are considered in this DFT screening. Numerous dopants were found to be useful for the enhancement of these characteristics. In particular, Mo, W, and Hg pose especially strong stabilization of the polar orthorhombic phase, thus ferroelectric characteristics. Regarding the piezoelectric activity in HfO_2 and ZrO_2, the later is found to be natively better for piezoelectric applications. The first reason for this is the larger difference in the volume of the tetragonal and polar orthorhombic phases, thus higher achievable strain during the phase transition. The second reason is the similarity of the total energies of these two crystal phases in ZrO_2. In HfO_2, the total energy of the tetragonal phase is much higher than it of the polar orthorhombic. However, for

the antiferroelectric-like behavior, thus high piezoelectric activity, the tetragonal must be below the polar orthorhombic phase. Therefore, in HfO_2, the tetragonal phase must be stabilized in the first place. This can be done by Ti, Si, Ge, and P doping, for instance. However, in terms of the piezoelectric coefficient, the doped HfO_2 just barely reaches the quality of the undoped ZrO_2. The doping of ZrO_2 improves its piezoelectric coefficient even further. The dopants like Yb, Li, and Na are the best in this regard. The last one nearly doubles the piezoelectric coefficient from 29 pm V^{-1} for the undoped to 57 pm V^{-1} for the Na-doped ZrO_2. Finally, these results are compared to the few available measured piezoelectric coefficients, yielding a good agreement with experiments.

The piezoelectric coefficients of doped ZrO_2 are also compared with other materials, for instance, perovskite-based and AlN-based materials, and $LiNbO_3$. Unfortunately, the piezoelectric coefficients of PZT, being two orders of magnitude larger, are unattainable for ZrO_2. However, the achievable strain by ZrO_2 is comparable to PZT, and in the case of Na-doped ZrO_2, it is even higher. There are two qualities of ZrO_2, which make it particularly distinguishable from PZT. First, ZrO_2 is lead-free, and second, it can be manufactured as thin-film down to several tens of nanometer in thickness. Therefore, ZrO_2 is an especially good alternative for piezoelectric thin-films applications, for instance, thin-film bulk acoustic wave resonators.

Regardless of the numerous articles and reviews published in the last decade on this intriguing material system, there is still a lot of open questions, which need to be addressed. A not closed topic is the doping of this material system. For instance, as pointed out previously, Mo, W, and Hg were found to be particularly interesting for the ferroelectric behavior in HfO_2 and ZrO_2. The further investigation of these dopants, also accompanied by oxygen vacancies, appears to be very promising and should be pursued. Only metal substitutions and interstitial defects were researched so far. No substituting defects for oxygen atoms such as S, F, or Cl were considered regarding the stabilization of the ferroelectric and antiferroelectric characteristics in $Hf_{1-x}Zr_xO_2$. It needs to be investigated, whether this type of defect has the potential for material characteristics improvement.

As discussed in section 2.4, in the frame of the nucleation theory, the interface energy between the stable and metastable phases plays also an important role, as it appears in the third power in expression for the thermodynamic energy barrier (Eq. (2.19)). This is a particularly hard task because numerous interfaces between crystal phases are possible and all of them need to be considered. Another obstacle that arises is that such interfaces in the idealistic DFT calculation are not stable and disassemble themselves during the structural relaxation. To tackle this problem, the DFT calculations need to be performed, in which space group symmetries are applied only to a fraction of geometry, in order to prevent the decay of the interface, which is not a trivial task. During the work on this dissertation, a proof of concept for this method was successfully shown. This method should be further developed and pursued by the successor student.

In this dissertation, the electric field-induced phase transition with changing crystal volume was considered as the cause for the enhanced piezoelectric activity in HfO_2 and ZrO_2. However, it still remains an unanswered question, whether this is the only mechanism for the piezoelectric activity. For instance, similarly to the perovskite-based materials, the domain switching and wall motion may also play an important role. For this, the possibility of 90° polarization rotation in HfO_2 and ZrO_2 must be evaluated.

The drawback of the DFT is its limitation in system size and time scale, which can be simulated. For instance, a structure consisting of 1000 atoms is barely solvable in a reasonable amount of time. The transient processes such as crystallization or electric field cycling are practically impossible to investigate. On the other end of the spectrum of atomistic simulations is the molecular dynamics

(MD). It allows systems consisting of millions of atoms to be simulated, because the MD implements purely classical interactions between atoms, thus the quantum mechanical nature is completely neglected. This means that the simulation accuracy is sacrificed in favor of the simulation speed. The solution for this problem brings the novel method of machine-learned classical potentials for MD, while the data for learning is provided by the DFT calculations [113, 114]. During the work on this dissertation, it was successfully shown, that this method can be applied to HfO_2 and ZrO_2. A classical potential was learned from the available DFT data, which was capable of simulating the dynamics of the tetragonal and polar orthorhombic crystal phases simultaneously. In the author's opinion, it is the most promising approach for dynamics simulation in HfO_2 and ZrO_2. The successor student should further pursue this idea.

Acknowledgments

First of all, I want to thank my first doctoral thesis supervisor, Alfred Kersch. Thank you for giving me the opportunity to be a part of your group and work on an exciting topic. Thank you for your continuous presence and support, especially in the hard times of frustration, for motivating me to pursue even greater and greater goals, for your positive attitude at all times. I have learned a lot in these four years.

I also want to thank my second doctoral thesis supervisor, Karsten Reuter, for giving me both scientific and personal advice. I am very grateful to you for giving me the opportunity to write the doctoral thesis at the Chair for Theoretical Chemistry.

I am also very thankful to my colleagues, Christopher Künneth, Robin Materlik, and Andreas Dörfler, for the serious and not so much talks and disputes, for the funny spent time in the office and outside of it (bars, beer gardens, etc.)

Very special thanks go to the collaborators from Aachen and Dresden, Fenja Berg, Tony Schenk, Ulrich Böttger, and Uwe Schröder. Thank you for the interesting scientific discussions on the conference days and nonscientific in the evenings.

Furthermore, I want to acknowledge the Deutsche Forschungsgemeinschaft (German Research Foundation) for funding the project which I worked on and FORWIN at the Munich University of Applied Sciences, especially Dr. Jürgen Meier and Dr. Katja Mitzscherling, for supporting and funding my foreign trips to conferences.

Last but not least, I want to say thank you to my wife, who always supported me in this endeavor, especially in its final stage. I am very thankful and grateful to You.

Bibliography

[1] W. Jo, R. Dittmer, M. Acosta, J. Zang, C. Groh, E. Sapper, K. Wang, and J. Rödel, "Giant electric-field-induced strains in lead-free ceramics for actuator applications – status and perspective," Journal of Electroceramics **29**, 71 (2012) (cit. on pp. 1, 14).

[2] B. Jaffe, R. S. Roth, and S. Marzullo, "Piezoelectric Properties of Lead Zirconate-Lead Titanate Solid-Solution Ceramics," Journal of Applied Physics **25**, 809 (1954) (cit. on pp. 1, 9).

[3] Official Journal of the European Union **L37**, 19 (2003) (cit. on pp. 1, 14).

[4] Official Journal of the European Union **L174**, 88 (2011) (cit. on pp. 1, 14).

[5] T. S. Böscke, J. Müller, D. Bräuhaus, U. Schröder, and U. Böttger, "Ferroelectricity in hafnium oxide thin films," Applied Physics Letters **99**, 102903 (2011) (cit. on pp. 1, 15, 17–20).

[6] J. Müller, T. S. Böscke, D. Bräuhaus, U. Schröder, U. Böttger, J. Sundqvist, P. Kücher, T. Mikolajick, and L. Frey, "Ferroelectric $Zr_{0.5}Hf_{0.5}O_2$ thin films for nonvolatile memory applications," Applied Physics Letters **99**, 112901 (2011) (cit. on pp. 1, 15, 17–19).

[7] T. Mikolajick, S. Slesazeck, M. H. Park, and U. Schroeder, "Ferroelectric hafnium oxide for ferroelectric random-access memories and ferroelectric field-effect transistors," MRS Bulletin **43**, 340 (2018) (cit. on pp. 2, 15).

[8] T. Mikolajick, S. Müller, T. Schenk, E. Yurchuk, S. Slesazeck, U. Schröder, S. Flachowsky, R. van Bentum, S. Kolodinski, P. Polakowski, and J. Müller, "Doped Hafnium Oxide – An Enabler for Ferroelectric Field Effect Transistors," Advances in Science and Technology **95**, 136 (2014) (cit. on pp. 2, 15).

[9] L. Landau and E. Lifshitz, in *Statistical Physics* (Elsevier, 1980) Chap. Phase Transitions of the Second Kind and Critical Phenomena, pp. 446–516 (cit. on p. 4).

[10] A. Devonshire, "XCVI. Theory of barium titanate—Part I," The London, Edinburgh, and Dublin Philosophical Magazine and Journal of Science **40**, 1040 (1949) (cit. on p. 4).

[11] A. Devonshire, "CIX. Theory of barium titanate—Part II," The London, Edinburgh, and Dublin Philosophical Magazine and Journal of Science **42**, 1065 (1951) (cit. on p. 4).

[12] W. J. Merz, "Double Hysteresis Loop of $BaTiO_3$ at the Curie Point," Physical Review **91**, 513 (1953) (cit. on p. 5).

[13] C. Malgrange, C. Ricolleau, and M. Schlenker, in *Symmetry and Physical Properties of Crystals* (Springer Netherlands, 2014) Chap. Elasticity, pp. 259–291 (cit. on p. 6).

[14] C. Malgrange, C. Ricolleau, and M. Schlenker, in *Symmetry and Physical Properties of Crystals* (Springer Netherlands, 2014) Chap. Crystal thermodynamics. Piezoelectricity, pp. 311–339 (cit. on pp. 6, 7).

[15] "IEEE Standard on Piezoelectricity," ANSI/IEEE Std 176-1987 `10.1109/ieeestd.1988.79638` (cit. on p. 7).

[16] A. Ziabicki and B. Misztal-Faraj, "Modeling of phase transitions in three-phase polymorphic systems: Part I. Basic equations and example simulation," Journal of Materials Research **26**, 1585 (2011) (cit. on p. 7).

[17] B. Jaffe, R. Roth, and S. Marzullo, "Properties of Piezoelectric Ceramics in the Solid-Solution Series Lead Titanate-Lead Zirconate-Lead Oxide: Tin Oxide and Lead Titanate-Lead Hafnate," Journal of Research of the National Bureau of Standards **55**, 239 (1955) (cit. on pp. 9, 14).

[18] S.-E. Park and T. R. Shrout, "Ultrahigh strain and piezoelectric behavior in relaxor based ferroelectric single crystals," Journal of Applied Physics **82**, 1804 (1997) (cit. on pp. 9, 11, 14).

[19] J.-F. Li, K. Wang, F.-Y. Zhu, L.-Q. Cheng, and F.-Z. Yao, "(K,Na)NbO_3-Based Lead-Free Piezoceramics: Fundamental Aspects, Processing Technologies, and Remaining Challenges," Journal of the American Ceramic Society **96**, edited by D. J. Green, 3677 (2013) (cit. on p. 9).

[20] Y. Saito, H. Takao, T. Tani, T. Nonoyama, K. Takatori, T. Homma, T. Nagaya, and M. Nakamura, "Lead-free piezoceramics," Nature **432**, 84 (2004) (cit. on pp. 9, 14).

[21] N. D. Quan, L. H. Bac, D. V. Thiet, V. N. Hung, and D. D. Dung, "Current Development in Lead-Free $Bi_{0.5}$(Na,K)$_{0.5}TiO_3$-Based Piezoelectric Materials," Advances in Materials Science and Engineering **2014**, 1 (2014) (cit. on p. 9).

[22] S. Trolier-McKinstry, in *Piezoelectric and Acoustic Materials for Transducer Applications* (Springer US, 2008) Chap. Crystal Chemistry of Piezoelectric Materials, pp. 39–56 (cit. on p. 10).

[23] G. Viola, T. Saunders, X. Wei, K. B. Chong, H. Luo, M. J. Reece, and H. Yan, "Contribution of piezoelectric effect, electrostriction and ferroelectric/ferroelastic switching to strain-electric field response of dielectrics," Journal of Advanced Dielectrics **03**, 1350007 (2013) (cit. on p. 10).

[24] J. Cannata, T. Ritter, W.-H. Chen, R. Silverman, and K. Shung, "Design of efficient, broadband single-element (20-80 MHz) ultrasonic transducers for medical imaging applications," IEEE Transactions on Ultrasonics, Ferroelectrics and Frequency Control **50**, 1548 (2003) (cit. on p. 10).

[25] H. Liu and B. Dkhil, "A brief review on the model antiferroelectric $PbZrO_3$ perovskite-like material," Zeitschrift für Kristallographie **226**, 163 (2011) (cit. on p. 11).

[26] L. E. Cross, "Electric Double Hysteresis in (K_xNa_{1-x})NbO_3 Single Crystals," Nature **181**, 178 (1958) (cit. on p. 11).

[27] D. Fu, M. Endo, H. Taniguchi, T. Taniyama, and M. Itoh, "$AgNbO_3$: A lead-free material with large polarization and electromechanical response," Applied Physics Letters **90**, 252907 (2007) (cit. on p. 11).

[28] S.-E. Park, M.-J. Pan, K. Markowski, S. Yoshikawa, and L. E. Cross, "Electric field induced phase transition of antiferroelectric lead lanthanum zirconate titanate stannate ceramics," Journal of Applied Physics **82**, 1798 (1997) (cit. on p. 11).

[29] M. E. Caspari and W. J. Merz, "The Electromechanical Behavior of $BaTiO_3$ Single-Domain Crystals," Physical Review **80**, 1082 (1950) (cit. on p. 11).

[30] G. Shirane, K. Suzuki, and A. Takeda, "Phase Transitions in Solid Solutions of $PbZrO_3$ and $PbTiO_3$ (II) X-ray Study," Journal of the Physical Society of Japan **7**, 12 (1952) (cit. on p. 14).

[31] T. Zheng, J. Wu, D. Xiao, and J. Zhu, "Recent development in lead-free perovskite piezoelectric bulk materials," Progress in Materials Science **98**, 552 (2018) (cit. on p. 14).

[32] J. Hao, W. Li, J. Zhai, and H. Chen, "Progress in high-strain perovskite piezoelectric ceramics," Materials Science and Engineering: R: Reports **135**, 1 (2019) (cit. on p. 14).

[33] J. Wang, H. P. Li, and R. Stevens, "Hafnia and hafnia-toughened ceramics," Journal of Materials Science **27**, 5397 (1992) (cit. on p. 15).

[34] E. H. Kisi and C. Howard, "Crystal Structures of Zirconia Phases and their Inter-Relation," Key Engineering Materials **153-154**, 1 (1998) (cit. on p. 15).

[35] J. Robertson and R. M. Wallace, "High-K materials and metal gates for CMOS applications," Materials Science and Engineering: R: Reports **88**, 1 (2015) (cit. on p. 15).

[36] W. Mueller, G. Aichmayr, W. Bergner, E. Erben, T. Hecht, C. Kapteyn, A. Kersch, S. Kudelka, F. Lau, J. Luetzen, A. Orth, J. Nuetzel, T. Schloesser, A. Scholz, U. Schroeder, A. Sieck, A. Spitzer, M. Strasser, P.-F. Wang, S. Wege, and R. Weis, "Challenges for the DRAM cell scaling to 40nm," in IEEE International Electron Devices Meeting, 2005. IEDM Technical Digest. (2005) (cit. on p. 15).

[37] J. W. Fergus, "Electrolytes for solid oxide fuel cells," Journal of Power Sources **162**, 30 (2006) (cit. on p. 15).

[38] J. Muller, E. Yurchuk, T. Schlosser, J. Paul, R. Hoffmann, S. Muller, D. Martin, S. Slesazeck, P. Polakowski, J. Sundqvist, M. Czernohorsky, K. Seidel, P. Kucher, R. Boschke, M. Trentzsch, K. Gebauer, U. Schroder, and T. Mikolajick, "Ferroelectricity in HfO_2 enables nonvolatile data storage in 28 nm HKMG," in 2012 Symposium on VLSI Technology (VLSIT) (2012) (cit. on p. 15).

[39] M. Trentzsch, S. Flachowsky, R. Richter, J. Paul, B. Reimer, D. Utess, S. Jansen, H. Mulaosmanovic, S. Muller, S. Slesazeck, J. Ocker, M. Noack, J. Muller, P. Polakowski, J. Schreiter, S. Beyer, T. Mikolajick, and B. Rice, "A 28nm HKMG super low power embedded NVM technology based on ferroelectric FETs," in 2016 IEEE International Electron Devices Meeting (IEDM) (2016) (cit. on p. 15).

[40] S. Dünkel, M. Trentzsch, R. Richter, P. Moll, C. Fuchs, O. Gehring, M. Majer, S. Wittek, B. Muller, T. Melde, H. Mulaosmanovic, S. Slesazeck, S. Müller, J. Ocker, M. Noack, D.-A. Löhr, P. Polakowski, J. Muller, T. Mikolajick, J. Hontschel, B. Rice, J. Pellerin, and S. Beyer, "A FeFET based super-low-power ultra-fast embedded NVM technology for 22nm FDSOI and beyond," in 2017 IEEE International Electron Devices Meeting (IEDM) (2017) (cit. on p. 15).

[41] M. H. Park, Y. H. Lee, T. Mikolajick, U. Schroeder, and C. S. Hwang, "Review and perspective on ferroelectric HfO_2-based thin films for memory applications," MRS Communications **8**, 795 (2018) (cit. on p. 15).

[42] A. Chernikova, M. Kozodaev, A. Markeev, D. Negrov, M. Spiridonov, S. Zarubin, O. Bak, P. Buragohain, H. Lu, E. Suvorova, A. Gruverman, and A. Zenkevich, "Ultrathin $Hf_{0.5}Zr_{0.5}O_2$ Ferroelectric Films on Si," ACS Applied Materials & Interfaces **8**, 7232 (2016) (cit. on p. 15).

[43] F. Ambriz-Vargas, G. Kolhatkar, M. Broyer, A. Hadj-Youssef, R. Nouar, A. Sarkissian, R. Thomas, C. Gomez-Yáñez, M. A. Gauthier, and A. Ruediger, "A Complementary Metal Oxide Semiconductor Process-Compatible Ferroelectric Tunnel Junction," ACS Applied Materials & Interfaces **9**, 13262 (2017) (cit. on p. 15).

[44] S. Salahuddin and S. Datta, "Use of Negative Capacitance to Provide Voltage Amplification for Low Power Nanoscale Devices," Nano Letters **8**, 405 (2008) (cit. on p. 15).

[45] M. Hoffmann, F. P. G. Fengler, M. Herzig, T. Mittmann, B. Max, U. Schroeder, R. Negrea, P. Lucian, S. Slesazeck, and T. Mikolajick, "Unveiling the double-well energy landscape in a ferroelectric layer," Nature **565**, 464 (2019) (cit. on p. 15).

[46] M. Hoffmann, B. Max, T. Mittmann, U. Schroeder, S. Slesazeck, and T. Mikolajick, "Demonstration of High-speed Hysteresis-free Negative Capacitance in Ferroelectric $Hf_{0.5}Zr_{0.5}O_2$," in 2018 IEEE International Electron Devices Meeting (IEDM) (2018) (cit. on p. 15).

[47] M. H. Park, H. J. Kim, Y. J. Kim, T. Moon, K. D. Kim, and C. S. Hwang, "Thin $Hf_xZr_{1-x}O_2$ Films: A New Lead-Free System for Electrostatic Supercapacitors with Large Energy Storage Density and Robust Thermal Stability," Advanced Energy Materials **4**, 1400610 (2014) (cit. on p. 16).

[48] M. Hoffmann, U. Schroeder, C. Künneth, A. Kersch, S. Starschich, U. Böttger, and T. Mikolajick, "Ferroelectric phase transitions in nanoscale HfO_2 films enable giant pyroelectric energy conversion and highly efficient supercapacitors," Nano Energy **18**, 154 (2015) (cit. on p. 16).

[49] M. H. Park, Y. H. Lee, H. J. Kim, Y. J. Kim, T. Moon, K. D. Kim, J. Müller, A. Kersch, U. Schroeder, T. Mikolajick, and C. S. Hwang, "Ferroelectricity and Antiferroelectricity of Doped Thin HfO_2-Based Films," Advanced Materials **27**, 1811 (2015) (cit. on pp. 16, 18).

[50] M. H. Park, H. J. Kim, Y. J. Kim, T. Moon, K. D. Kim, and C. S. Hwang, "Toward a multifunctional monolithic device based on pyroelectricity and the electrocaloric effect of thin antiferroelectric $Hf_xZr_{1-x}O_2$ films," Nano Energy **12**, 131 (2015) (cit. on p. 16).

[51] M. H. Park, H. J. Kim, Y. J. Kim, T. Moon, K. D. Kim, Y. H. Lee, S. D. Hyun, and C. S. Hwang, "Giant Negative Electrocaloric Effects of $Hf_{0.5}Zr_{0.5}O_2$ Thin Films," Advanced Materials **28**, 7956 (2016) (cit. on p. 16).

[52] C. Mart, T. Kämpfe, S. Zybell, and W. Weinreich, "Layer thickness scaling and wake-up effect of pyroelectric response in Si-doped HfO_2," Applied Physics Letters **112**, 052905 (2018) (cit. on p. 16).

[53] J. Liu, S. Liu, L. H. Liu, B. Hanrahan, and S. T. Pantelides, "Origin of Pyroelectricity in Ferroelectric HfO_2," Physical Review Applied **12**, 034032 (2019) (cit. on pp. 16, 20).

[54] R. Ruh, H. J. Garrett, R. F. Domagala, and N. M. Tallan, "The System Zirconia-Hafnia," Journal of the American Ceramic Society **51**, 23 (1968) (cit. on p. 16).

[55] Y. Al-Khatatbeh, K. K. M. Lee, and B. Kiefer, "Phase diagram up to 105 GPa and mechanical strength of HfO_2," Physical Review B **82**, 144106 (2010) (cit. on p. 16).

[56] Y. Al-Khatatbeh, K. K. M. Lee, and B. Kiefer, "Phase relations and hardness trends of zro_2 phases at high pressure," Physical Review B **81**, 214102 (2010) (cit. on p. 16).

[57] X. Sang, E. D. Grimley, T. Schenk, U. Schroeder, and J. M. LeBeau, "On the structural origins of ferroelectricity in HfO_2 thin films," Applied Physics Letters **106**, 162905 (2015) (cit. on p. 17).

[58] E. H. Kisi, C. J. Howard, and R. J. Hill, "Crystal Structure of Orthorhombic Zirconia in Partially Stabilized Zirconia," Journal of the American Ceramic Society **72**, 1757 (1989) (cit. on p. 17).

[59] T. D. Huan, V. Sharma, G. A. Rossetti, and R. Ramprasad, "Pathways towards ferroelectricity in hafnia," Physical Review B **90**, 064111 (2014) (cit. on p. 17).

[60] S. V. Barabash, "Prediction of new metastable HfO_2 phases: toward understanding ferro- and antiferroelectric films," Journal of Computational Electronics **16**, 1227 (2017) (cit. on p. 17).

[61] C. Künneth, R. Materlik, M. Falkowski, and A. Kersch, "Impact of Four-Valent Doping on the Crystallographic Phase Formation for Ferroelectric HfO_2 from First-Principles: Implications for Ferroelectric Memory and Energy-Related Applications," ACS Applied Nano Materials **1**, 254 (2017) (cit. on pp. 17, 19).

[62] J. Müller, T. S. Böscke, U. Schröder, S. Mueller, D. Bräuhaus, U. Böttger, L. Frey, and T. Mikolajick, "Ferroelectricity in Simple Binary ZrO_2 and HfO_2," Nano Letters **12**, 4318 (2012) (cit. on pp. 17–20).

[63] P. Hohenberg and W. Kohn, "Inhomogeneous Electron Gas," Physical Review **136**, B864 (1964) (cit. on p. 17).

[64] W. Kohn and L. J. Sham, "Self-Consistent Equations Including Exchange and Correlation Effects," Physical Review **140**, A1133 (1965) (cit. on p. 17).

[65] J. P. Perdew and Y. Wang, "Accurate and simple analytic representation of the electron-gas correlation energy," Physical Review B **45**, 13244 (1992) (cit. on p. 17).

[66] J. P. Perdew, K. Burke, and M. Ernzerhof, "Generalized Gradient Approximation Made Simple," Physical Review Letters **77**, 3865 (1996) (cit. on p. 17).

[67] J. P. Perdew, A. Ruzsinszky, G. I. Csonka, O. A. Vydrov, G. E. Scuseria, L. A. Constantin, X. Zhou, and K. Burke, "Restoring the Density-Gradient Expansion for Exchange in Solids and Surfaces," Physical Review Letters **100**, 136406 (2008) (cit. on p. 17).

[68] V. Blum, R. Gehrke, F. Hanke, P. Havu, V. Havu, X. Ren, K. Reuter, and M. Scheffler, "Ab initio molecular simulations with numeric atom-centered orbitals," Computer Physics Communications **180**, 2175 (2009) (cit. on p. 18).

[69] C. Künneth, R. Materlik, and A. Kersch, "Modeling ferroelectric film properties and size effects from tetragonal interlayer in $Hf_{1-x}Zr_xO_2$ grains," Journal of Applied Physics **121**, 205304 (2017) (cit. on pp. 17, 18).

[70] R. Materlik, C. Künneth, and A. Kersch, "The origin of ferroelectricity in $Hf_{1-x}Zr_xO_2$: A computational investigation and a surface energy model," Journal of Applied Physics **117**, 134109 (2015) (cit. on p. 18).

[71] M. H. Park, Y. H. Lee, H. J. Kim, T. Schenk, W. Lee, K. D. Kim, F. P. G. Fengler, T. Mikolajick, U. Schroeder, and C. S. Hwang, "Surface and grain boundary energy as the key enabler of ferroelectricity in nanoscale hafnia-zirconia: a comparison of model and experiment," Nanoscale **9**, 9973 (2017) (cit. on p. 18).

[72] S. Starschich, T. Schenk, U. Schroeder, and U. Boettger, "Ferroelectric and piezoelectric properties of $Hf_{1-x}Zr_xO_2$ and pure ZrO_2 films," Applied Physics Letters **110**, 182905 (2017) (cit. on pp. 18, 20).

[73] T. Mimura, T. Shimizu, and H. Funakubo, "Ferroelectricity in $YO_{1.5}$-HfO_2 films around 1μm in thickness," Applied Physics Letters **115**, 032901 (2019) (cit. on p. 18).

[74] J. Müller, U. Schröder, T. S. Böscke, I. Müller, U. Böttger, L. Wilde, J. Sundqvist, M. Lemberger, P. Kücher, T. Mikolajick, and L. Frey, "Ferroelectricity in yttrium-doped hafnium oxide," Journal of Applied Physics **110**, 114113 (2011) (cit. on pp. 18, 19).

[75] S. Mueller, J. Mueller, A. Singh, S. Riedel, J. Sundqvist, U. Schroeder, and T. Mikolajick, "Incipient Ferroelectricity in Al-Doped HfO_2 Thin Films," Advanced Functional Materials **22**, 2412 (2012) (cit. on pp. 18, 19).

[76] S. Mueller, C. Adelmann, A. Singh, S. V. Elshocht, U. Schroeder, and T. Mikolajick, "Ferroelectricity in Gd-Doped HfO_2 Thin Films," ECS Journal of Solid State Science and Technology **1**, N123 (2012) (cit. on pp. 18, 19).

[77] M. Hoffmann, U. Schroeder, T. Schenk, T. Shimizu, H. Funakubo, O. Sakata, D. Pohl, M. Drescher, C. Adelmann, R. Materlik, A. Kersch, and T. Mikolajick, "Stabilizing the ferroelectric phase in doped hafnium oxide," Journal of Applied Physics **118**, 072006 (2015) (cit. on pp. 18, 19).

[78] T. Schenk, S. Mueller, U. Schroeder, R. Materlik, A. Kersch, M. Popovici, C. Adelmann, S. V. Elshocht, and T. Mikolajick, "Strontium doped hafnium oxide thin films: Wide process window for ferroelectric memories," in 2013 Proceedings of the European Solid-State Device Research Conference (ESSDERC) (2013) (cit. on pp. 18, 19).

[79] A. G. Chernikova, D. S. Kuzmichev, D. V. Negrov, M. G. Kozodaev, S. N. Polyakov, and A. M. Markeev, "Ferroelectric properties of full plasma-enhanced ALD TiN/La:HfO_2/TiN stacks," Applied Physics Letters **108**, 242905 (2016) (cit. on pp. 18, 19).

[80] U. Schroeder, C. Richter, M. H. Park, T. Schenk, M. Pešić, M. Hoffmann, F. P. G. Fengler, D. Pohl, B. Rellinghaus, C. Zhou, C.-C. Chung, J. L. Jones, and T. Mikolajick, "Lanthanum-Doped Hafnium Oxide: A Robust Ferroelectric Material," Inorganic Chemistry **57**, 2752 (2018) (cit. on pp. 18, 19).

[81] P. Polakowski and J. Müller, "Ferroelectricity in undoped hafnium oxide," Applied Physics Letters **106**, 232905 (2015) (cit. on p. 18).

[82] S. Starschich, D. Griesche, T. Schneller, R. Waser, and U. Böttger, "Chemical solution deposition of ferroelectric yttrium-doped hafnium oxide films on platinum electrodes," Applied Physics Letters **104**, 202903 (2014) (cit. on pp. 18, 19).

[83] S. Starschich, D. Griesche, T. Schneller, and U. Böttger, "Chemical Solution Deposition of Ferroelectric Hafnium Oxide for Future Lead Free Ferroelectric Devices," ECS Journal of Solid State Science and Technology **4**, P419 (2015) (cit. on p. 18).

[84] S. Starschich and U. Boettger, "An extensive study of the influence of dopants on the ferroelectric properties of HfO_2," Journal of Materials Chemistry C **5**, 333 (2017) (cit. on p. 18).

[85] S. Starschich and U. Böttger, "Doped ZrO_2 for future lead free piezoelectric devices," Journal of Applied Physics **123**, 044101 (2018) (cit. on pp. 18–20).

[86] T. Shimizu, T. Yokouchi, T. Oikawa, T. Shiraishi, T. Kiguchi, A. Akama, T. J. Konno, A. Gruverman, and H. Funakubo, "Contribution of oxygen vacancies to the ferroelectric behavior of $Hf_{0.5}Zr_{0.5}O_2$ thin films," Applied Physics Letters **106**, 112904 (2015) (cit. on p. 18).

[87] T. Olsen, U. Schröder, S. Müller, A. Krause, D. Martin, A. Singh, J. Müller, M. Geidel, and T. Mikolajick, "Co-sputtering yttrium into hafnium oxide thin films to produce ferroelectric properties," Applied Physics Letters **101**, 082905 (2012) (cit. on pp. 18, 19).

[88] L. Xu, T. Nishimura, S. Shibayama, T. Yajima, S. Migita, and A. Toriumi, "Ferroelectric phase stabilization of HfO_2 by nitrogen doping," Applied Physics Express **9**, 091501 (2016) (cit. on pp. 18, 19).

[89] L. Xu, T. Nishimura, S. Shibayama, T. Yajima, S. Migita, and A. Toriumi, "Kinetic pathway of the ferroelectric phase formation in doped HfO_2 films," Journal of Applied Physics **122**, 124104 (2017) (cit. on pp. 18, 19).

[90] Y. H. Lee, H. J. Kim, T. Moon, K. D. Kim, S. D. Hyun, H. W. Park, Y. B. Lee, M. H. Park, and C. S. Hwang, "Preparation and characterization of ferroelectric $Hf_{0.5}Zr_{0.5}O_2$ thin films grown by reactive sputtering," Nanotechnology **28**, 305703 (2017) (cit. on p. 18).

[91] T. Shimizu, K. Katayama, T. Kiguchi, A. Akama, T. J. Konno, and H. Funakubo, "Growth of epitaxial orthorhombic $YO_{1.5}$-substituted HfO_2 thin film," Applied Physics Letters **107**, 032910 (2015) (cit. on p. 18).

[92] T. Shimizu, K. Katayama, T. Kiguchi, A. Akama, T. J. Konno, O. Sakata, and H. Funakubo, "The demonstration of significant ferroelectricity in epitaxial Y-doped HfO_2 film," Scientific Reports **6**, 32931 (2016) (cit. on pp. 18, 19).

[93] M. H. Park, H. J. Kim, Y. J. Kim, W. Lee, T. Moon, and C. S. Hwang, "Evolution of phases and ferroelectric properties of thin $Hf_{0.5}Zr_{0.5}O_2$ films according to the thickness and annealing temperature," Applied Physics Letters **102**, 242905 (2013) (cit. on p. 18).

[94] M. H. Park, H. J. Kim, Y. J. Kim, T. Moon, and C. S. Hwang, "The effects of crystallographic orientation and strain of thin $Hf_{0.5}Zr_{0.5}O_2$ film on its ferroelectricity," Applied Physics Letters **104**, 072901 (2014) (cit. on p. 18).

[95] T. Shiraishi, K. Katayama, T. Yokouchi, T. Shimizu, T. Oikawa, O. Sakata, H. Uchida, Y. Imai, T. Kiguchi, T. J. Konno, and H. Funakubo, "Impact of mechanical stress on ferroelectricity in $(Hf_{0.5}Zr_{0.5})O_2$ thin films," Applied Physics Letters **108**, 262904 (2016) (cit. on p. 18).

[96] R. Batra, T. D. Huan, J. L. Jones, G. Rossetti, and R. Ramprasad, "Factors Favoring Ferroelectricity in Hafnia: A First-Principles Computational Study," The Journal of Physical Chemistry C **121**, 4139 (2017) (cit. on p. 18).

[97] R. Batra, H. D. Tran, and R. Ramprasad, "Stabilization of metastable phases in hafnia owing to surface energy effects," Applied Physics Letters **108**, 172902 (2016) (cit. on p. 18).

[98] C. Richter, T. Schenk, M. H. Park, F. A. Tscharntke, E. D. Grimley, J. M. LeBeau, C. Zhou, C. M. Fancher, J. L. Jones, T. Mikolajick, and U. Schroeder, "Si Doped Hafnium Oxide—A "Fragile"Ferroelectric System," Advanced Electronic Materials **3**, 1700131 (2017) (cit. on p. 19).

[99] T. Schenk, C. M. Fancher, M. H. Park, C. Richter, C. Künneth, A. Kersch, J. L. Jones, T. Mikolajick, and U. Schroeder, "On the Origin of the Large Remanent Polarization in La:HfO_2," Advanced Electronic Materials **5**, 1900303 (2019) (cit. on p. 19).

[100] S. Yoneda, T. Hosokura, M. Kimura, A. Ando, and K. Shiratsuyu, "Nonlinear polarization responses of ZrO_2-based thin films fabricated by chemical solution deposition," Japanese Journal of Applied Physics **56**, 10PF07 (2017) (cit. on p. 19).

[101] R. Materlik, C. Künneth, T. Mikolajick, and A. Kersch, "The impact of charge compensated and uncompensated strontium defects on the stabilization of the ferroelectric phase in HfO_2," Applied Physics Letters **111**, 082902 (2017) (cit. on p. 19).

[102] R. Materlik, C. Künneth, M. Falkowski, T. Mikolajick, and A. Kersch, "Al-, Y-, and La-doping effects favoring intrinsic and field induced ferroelectricity in HfO_2: A first principles study," Journal of Applied Physics **123**, 164101 (2018) (cit. on p. 19).

[103] M. Falkowski, C. Künneth, R. Materlik, and A. Kersch, "Unexpectedly large energy variations from dopant interactions in ferroelectric HfO_2 from high-throughput ab initio calculations," npj Computational Materials **4**, 73 (2018) (cit. on pp. 19, 27).

[104] S. Dutta, H. Aramberri, T. Schenk, and J. Íñiguez, "Effect of Dopant Ordering on the Stability of Ferroelectric Hafnia," physica status solidi (RRL) – Rapid Research Letters **14**, 2000047 (2020) (cit. on p. 19).

[105] R. Batra, T. D. Huan, G. A. Rossetti, and R. Ramprasad, "Dopants Promoting Ferroelectricity in Hafnia: Insights from a comprehensive Chemical Space Exploration," Chemistry of Materials **29**, 9102 (2017) (cit. on p. 19).

[106] M. Falkowski and A. Kersch, "Optimizing the Piezoelectric Strain in ZrO_2- and HfO_2-Based Incipient Ferroelectrics for Thin-Film Applications: An Ab Initio Dopant Screening Study," ACS Applied Materials & Interfaces **12**, 32915 (2020) (cit. on pp. 19, 20, 27).

[107] M. H. Park, Y. H. Lee, T. Mikolajick, U. Schroeder, and C. S. Hwang, "Thermodynamic and Kinetic Origins of Ferroelectricity in Fluorite Structure Oxides," Advanced Electronic Materials **5**, 1800522 (2018) (cit. on p. 19).

[108] S. Liu and B. M. Hanrahan, "Effects of growth orientations and epitaxial strains on phase stability of HfO_2 thin films," Physical Review Materials **3**, 054404 (2019) (cit. on p. 19).

[109] S. E. Reyes-Lillo, K. F. Garrity, and K. M. Rabe, "Antiferroelectricity in thin-film ZrO_2 from first principles," Physical Review B **90**, 140103 (2014) (cit. on p. 20).

[110] S. Kirbach, K. Kuhnel, and W. Weinreich, "Piezoelectric Hafnium Oxide Thin Films for Energy-Harvesting Applications," in 2018 IEEE 18th International Conference on Nanotechnology (IEEE-NANO) (2018) (cit. on p. 20).

[111] C. Mart, T. Kämpfe, R. Hoffmann, S. Eßlinger, S. Kirbach, K. Kühnel, M. Czernohorsky, L. M. Eng, and W. Weinreich, "Piezoelectric Response of Polycrystalline Silicon-Doped Hafnium Oxide Thin Films Determined by Rapid Temperature Cycles," Advanced Electronic Materials **6**, 1901015 (2020) (cit. on p. 20).

[112] M. H. Park, C.-C. Chung, T. Schenk, C. Richter, M. Hoffmann, S. Wirth, J. L. Jones, T. Mikolajick, and U. Schroeder, "Origin of Temperature-Dependent Ferroelectricity in Si-Doped HfO_2," Advanced Electronic Materials **4**, 1700489 (2018) (cit. on p. 27).

[113] H. Wang, L. Zhang, J. Han, and W. E, "DeePMD-kit: A deep learning package for many-body potential energy representation and molecular dynamics," Computer Physics Communications **228**, 178 (2018) (cit. on p. 29).

[114] L. Zhang, D.-Y. Lin, H. Wang, R. Car, and W. E, "Active learning of uniformly accurate interatomic potentials for materials simulation," Physical Review Materials **3**, 023804 (2019) (cit. on p. 29).

Appendices

A Article #1

Unexpectedly large energy variations from dopant interactions in ferroelectric HfO_2 from high-throughput ab initio calculations

Max Falkowski, Christopher Künneth, Robin Materlik, and Alfred Kersch

npj Comput Mater **4**, 73 (2018)
DOI: 10.1038/s41524-018-0133-4

npj | Computational Materials

www.nature.com/npjcompumats

ARTICLE OPEN

Unexpectedly large energy variations from dopant interactions in ferroelectric HfO_2 from high-throughput ab initio calculations

Max Falkowski[1], Christopher Künneth[1], Robin Materlik[1] and Alfred Kersch[1]

Insight into the origin of process-related properties like small-scale inhomogeneities is key for material optimization. Here, we analyze DFT calculations of randomly doped HfO_2 structures with Si, La, and V_O and relate them to the kind of production process. Total energies of the relevant ferroelectric $Pbc2_1$ phase are compared with the competing crystallographic phases under the influence of the arising local inhomogeneities in a coarse-grained approach. The interaction among dopants adds to the statistical effect from the random positioning of the dopants. In anneals after atomic layer or chemical solution deposition processes, which are short compared to ceramic process tempering, the large energy variations remain because the dopants do not diffuse. Since the energy difference is the criterion for the phase stability, the large variation suggests the possibility of nanoregions and diffuse phase transitions because these local doping effects may move the system over the paraelectric-ferroelectric phase boundary.

npj Computational Materials (2018) 4:73; https://doi.org/10.1038/s41524-018-0133-4

INTRODUCTION

Random distributions of the dopant positions may lead to variances of materials properties, causing unexpected but potentially useful effects. Distance-dependent interactions of dopants, as we demonstrate here on the example of La- and Si-doped HfO_2, lead to two different contributions in the variation of local energy density: (i) local variations of the concentration from random dopant positions, and (ii) local variations from dopant arrangement. An example of concentration variation is extrinsic channel doping in nanoscale transistors on the ppm level leading to a statistical variation of the small number of dopants in the device, measurable in the threshold voltage.[1] However, in ferroelectric materials like the newly discovered HfO_2 stabilized in the polar-orthorhombic phase,[2] doping concentrations are at least on the percent level because their mechanism is based on the modification of the local structure and free energy, affecting the phase stability.[3,4] For such large concentration c, one could expect a standard deviation $\sigma(\overline{E})$ of the mean energy density $\overline{E}$ resulting from $\sigma(\overline{c})$ and sensitivity as $\sigma(\overline{E}) = \frac{\partial \overline{E}}{\partial c}\sigma(\overline{c})$, which is only significant for control volumes of small size L^3 containing few dopant atoms. However, we have found significant additional energy variations IQR(E) on the atomistic length scale ξ, resulting from the dopant−dopant interactions, which we calculate as $\xi \sim 1$ nm. They can be identified by choosing control volumes of edge size ξ in a coarse-grained approach to the free energy.[5,6] Furthermore, the doping concentration variation has the same interaction range; hence $L = \xi$, and the total energy variation results into the sum of $\sigma(\overline{E})$ and IQR(E)/2. Experimentally, especially in ferroelectric materials,[7] nanodomains of different doping concentrations may be found with different physical properties and diffusive phase transitions.[8–10] Positional static disorder has been proposed as the origin of relaxor ferroelectrics with exceptional piezoelectric and dielectric properties.[11,12] Furthermore, nanolaminates have been processed and have shown improved ferroelectric properties in particular cases.[13–15] Although there is an enormous amount of experimental[16] and theoretical[17] work quantifying the influence of dopant order on average quantities, there is no theoretical work quantifying the local variation $\sigma(\overline{E}) + \mathrm{IQR}(E)/2$ that may occur on the scale ξ and relate them to the production process.

A very promising, recently discovered ferroelectric materials class is HfO_2 and ZrO_2,[2,18–21] which is based on the fluorite instead of the prominent perovskite structure.[22,23] The stabilization of the desired ferroelectric crystal phase is achieved with doping on the percent level.[24–27] Pure HfO_2 and ZrO_2 are chemically similar (i.e. they have a low atomic chemical potential[27]) and crystallize in the monoclinic $P2_1/c$ phase (m-phase) at low temperatures. Under medium pressure (~10 GPa) a nonpolar, orthorhombic Pbca phase (o-phase) is stabilized. Differently, with increasing temperatures, the m-phase transforms first to the tetragonal $P4_2/nmc$ (t-phase) and then to the cubic $Fm\bar{3}m$ (c-phase) crystallographic phase. Appropriate doping concentrations can modify the materials characteristics of both HfO_2 and ZrO_2 for particular applications. For instance, by this means, the t-phase with a high dielectric constant $k \sim 40$ can be promoted to be the stable phase at room temperatures, utilized as insulator layers for metal-oxide-semiconductor field-effect transistors gates[28] and dynamic random access memory capacitors.[29] Another example is yttrium-doped ZrO_2 in the c-phase (YSZ), an important material for solid oxide fuel cells and gas sensors.[30] Finally, HfO_2 and ZrO_2 can exhibit ferroelectricity in thin films for certain doping concentrations.[4,18] The ferroelectricity arises from the polar, orthorhombic $Pbc2_1$ phase (p-o-phase).[31] Thus, HfO_2 and ZrO_2 are a lead-free and CMOS-compatible material class for applications like ferroelectric field-effect transistors, ferroelectric random access memory,[32] and pyro- and piezoelectric sensors.[4]

[1]Munich University of Applied Sciences, Lothstr. 34, 80335 Munich, Germany
Correspondence: Max Falkowski (max.falkowski@hm.edu) or Alfred Kersch (alfred.kersch@hm.edu)

Received: 3 September 2018 Accepted: 22 November 2018
Published online: 10 December 2018

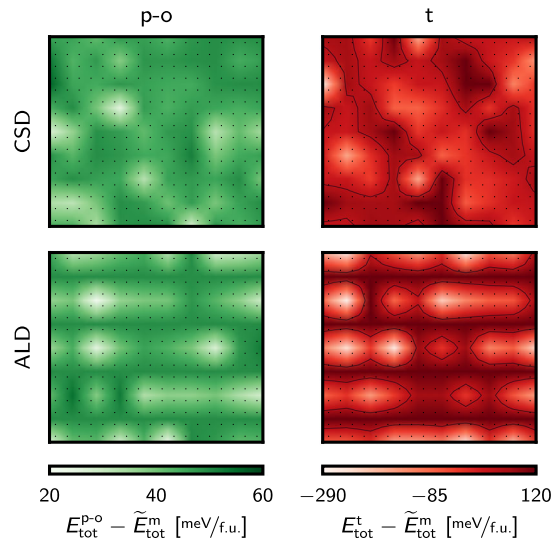

Fig. 1 Energy landscapes of 9×10 nm^2 sections of Si-doped HfO_2 material in a coarse-grained approach with length scale $\xi = 1$ nm for the p-o-phase (left column) and the t-phase (right column). The CSD deposited material (upper row) is homogeneously doped with a concentration of 6.25 f.u.%. For the ALD deposited material (lower row), 1 nm layers of 12.5 f.u.% are followed by layers of 0 f.u.%. In the t-phase energy landscapes, the black contour lines indicate the boundary where the energy shifts locally below the energy of the p-o-phase

Crystal structures with dopants processed with a high thermal budget, such as ceramics, will approach their thermodynamic equilibrium configuration. In this lowest-energy configuration, the dopants are not necessarily randomly distributed but may develop a long-range order and the structural energy might be lower for such a distribution.[33] In contrast, the dopant distribution of chemical solution deposition (CSD)-manufactured films using a liquid precursor is believed to be almost random. After crystallization with a moderate thermal budget anneal,[19] local energy variations on the atomistic length scale from imprinted dopant positions remain. Yet another case are atomic layer deposition (ALD)-manufactured films. Since the host material (Hf or Zr) and the dopants are deposited in alternating layers, the doping distribution in the film deposition direction is enforced to follow the sequence of the layers whereas it is random in the layer plane. There are several experimental observations that require an explanation. The remanent polarization of ferroelectric $Hf_{0.5}Zr_{0.5}O_2$ ALD films,[34,35] which are actually nanolaminates depending on the cycle ratio of Hf and Zr, has been found to vary strongly with the laminate thickness ranging from 1 to 4 nm,[15] which can be considered as 1D nanoregion effects. The positions of dopants were investigated by Lomenzo et al.[36] and Richter et al.[37] They studied laminate structures from Si doping cycles in HfO_2 with the time-of-flight secondary ion mass spectrometry and high-resolution transmission electron microscopy (HR-TEM) after thermal processing and proved the limited mobility of cations in the low thermal budget ALD and CSD anneals. Oxygen, on the other hand, has been found to be very mobile,[38–40] allowing the formation or dissolution of dopant−oxygen vacancy defect configurations, depending on the oxygen supply and thermal processing. Finally, a temperature-induced polar to nonpolar phase transition in Si-doped HfO_2 has been found to be extremely broad.[41,42]

As pointed out in the last paragraph, each of the three processing techniques reveals different dopant distributions, which only in one case represents the thermodynamic equilibrium configuration with the lowest energy. Doping of HfO_2[25–27,43–45] and ZrO_2[46] was extensively researched utilizing the density functional theory (DFT) and using cluster expansion[30,33,47] or high-throughput calculations[48] under the premise that the lowest-energy structure is realized in thin films. Although all these studies attempt to answer the question of phase stabilization with doping, they do not consider the energy variation from the doping distribution enforced and biased by the processing technique. Attempting to fully cover the question of phase stabilization in HfO_2 from doping, the current study thoroughly investigates the influences of La and Si[37,49,50] doping (also considering oxygen vacancies), and their mixtures on the phases of HfO_2 for different doping concentrations and defect combinations, taking into account the dopant distribution of the different manufacturing processes. Since the goal is not to search for the lowest-energy incorporation of the dopant in HfO_2, the high-throughput approach is preferred to the cluster expansion. It is unavoidable to perform a numerous statistic of calculations for different arrangements of La and Si atoms in the HfO_2 matrix for a thorough study of the dopant mixture.

Some of the results can be condensed in a coarse-grained energy landscape (Fig. 1) which is fundamental for understanding local nanoregions that have been suggested in ferroelectric, doped HfO_2 based on HR-TEM observations.[51]

RESULTS

A first step in investigating the positional arrangements of defects and their combinations is to define the defects. As Künneth et al.[27] have shown that Si_{Hf} and $Si_{Hf}V_O$ defects have similar impacts on the energetics in HfO_2, only the (i) Si_{Hf} defect is considered in this study. On the contrary, La is a III-valent dopant in HfO_2 necessitating the consideration of oxygen vacancies (V_O). Following the work of Materlik et al.,[26] which computationally investigated La and V_O defects in HfO_2 and showcased different DFT energies, we decided to focus on three La defects: (ii) electronically compensated La_{Hf}, (iii) mixed compensated $La_{Hf}V_O$ and (iv) ionically compensated $La_{Hf}La_{Hf}V_O$. Altogether, four defects are discussed in this study, which can be expressed using the Kröger-Vink notation as

(i) $1/2O_2 + La_2O_3 \rightarrow 2La'_{Hf} + 4O_O + 2h^{\cdot}$,
(ii) $La_2O_3 \rightarrow 2La'_{Hf} + 2O_O + 2V^{\cdot\cdot}_O + 2e' + 1/2O_2$,
(iii) $La_2O_3 \rightarrow 2La'_{Hf} + 3O_O + V^{\cdot\cdot}_O$ and
(iv) $SiO_2 \rightarrow Si_{Hf} + 2O_O$.

Apart from the single defects defined in the previous list, selected defect pairs are investigated in this publication. Table 1 summarizes these defect combinations along with their supercell (SC) sizes, ensuring the defect concentration. Considering the symmetry of the different phases, the number of positional arrangements can be computed, which may be further reduced by thoughts detailed in the section "Geometries setup for the calculations" (# nonequiv.). A dash (−) separating two defects indicates that all positional arrangements of the defects pair are considered. For instance, in the case of the defect combination $Si_{Hf} - Si_{Hf}$ all possible metal positions of the Si's in a 96-atomic supercell (992) are regarded. Conversely, defect constituents written in parentheses build a tightly packed defect. For instance, the combination ($La_{Hf}V_O$) means the V_O is in the direct vicinity of the La_{Hf} (next-neighbor). The selection of the defect combinations was generally performed with increasing complexity taking into account the computational effort of the DFT computations. Apart from the two simple defects, Si_{Hf} and La_{Hf}, and their combinations, the mixed compensated ($La_{Hf}V_O$), the ionically compensated ($La_{Hf}La_{Hf}V_O$) and two complex defect pairs are considered in this study. Moreover, in the case of $La_{Hf} - La_{Hf}$, $Si_{Hf} - La_{Hf}$ and ($La_{Hf}V_O$), we considered two doping concentrations. For the remainder of this work, the collection of calculations of a certain supercell size and defect combination of all four crystal phases is referred to a

Table 1. Summary of the defect combinations, the supercell (SC) size, the resulting concentration for the four different phases in HfO_2

Defect combinations[a]	SC size[b]	Conc. [f.u.%]	Phase	# arrangements[c]	# nonequiv.[d]	Defect combinations[a]	SC size[b]	Conc. [f.u.%]	Phase	# arrangements[c]	# nonequiv.[d]
La_{Hf}	96	3.125	m	32	1	Si_{Hf}	96	3.125	m	32	1
			o	32	1				o	32	1
			p-o	32	1				p-o	32	1
			t	32	1				t	32	1
$La_{Hf} - La_{Hf}$	96	6.25	m	992	23	$Si_{Hf} - Si_{Hf}$	96	6.25	m	992	23
			o	992	23				o	992	23
			p-o	992	19				p-o	992 (864)	19 (16)
			t	992	9				t	992	9
$La_{Hf} - La_{Hf}$	48	12.5	m	720	34	$Si_{Hf} - La_{Hf}$	96	6.25	m	992	31
			o	480	25				o	992	31
			p-o	720	30				p-o	992	31
			t	720 (656)	12 (11)				t	992	9
$(La_{Hf}V_O)$	96	3.125	m	256	8	$Si_{Hf} - La_{Hf}$	48	12.5	m	720	45
			o	256	8				o	480	30
			p-o	256	8				p-o	720 (592)	45 (37)
			t	256	2				t	720	13
$(La_{Hf}V_O)$	48	6.25	m	384	24	$Si_{Hf} - (La_{Hf}V_O)$	96	6.25	m	7936	248
			o	256	16				o	7936	248
			p-o	384	24				p-o	7936	248
			t	384 (256)	4 (2)				t	7936	38
$(La_{Hf}La_{Hf}V_O)$	96	6.25	m	768	12	$Si_{Hf} - (La_{Hf}La_{Hf}V_O)$	96	9.375	m	23,040	360
			o	768	12				o	23,040	360
			p-o	768	12				p-o	23,040 (21,376)	360 (334)
			t	768	3				t	23,040	52

[a]Defect combinations in parentheses are positioned in vicinity (next-neighbors, tight defects)
[b]Nominal number of atoms in a supercell (SC) size. Introduction of an oxygen vacancy into the SC reduces the number of atoms by one. Nevertheless, the SCs with an oxygen vacancy are referred to as 48-atomic or 96-atomic
[c]Number of possible defect arrangements in the SC. Parentheses enclose the arrangements after filtering out the phase-transformed structures during the structural relaxation, as discussed in the section "Phase transformation detection during structural relaxation"
[d]Number of nonequivalent structures for which DFT calculations need to be performed. The reduction of needed calculations is discussed in the section "Geometries setup for the calculations". Parentheses enclose the number of structures that have stayed in the initial crystal phase during the structural relaxation

set. For instance, a *set* of pure HfO_2 calculations consists of four calculations, one for each crystal phase. Table 1 lists 12 *sets* of 12 different defects and concentrations.

In order to be able to compare different defect types containing different atom species, a unified concentration definition is needed. One formula unit (f.u.) is defined by one metal and two oxygen sites. For instance, a 96-atom supercell contains 32 f.u.s. Placing one La_{Hf} or $(La_{Hf}V_O)$ defect into the cell results in a concentration of 3.125f.u.%, because both defects need exactly one of 32 f.u.s. Opposed to these defects, $(La_{Hf}La_{Hf}V_O)$ needs two f.u.s, resulting in a doubled concentration of 6.25f.u.%.

The boxes in Fig. 2 show DFT energies of the four phases with respect to the energy median $\tilde{E}$ of the m-phase carried out for the defect combinations tabulated in Table 1. For instance, the boxplots for the 6.25 f.u.% $La_{Hf} - La_{Hf}$ defect in Fig. 2a represent in each case 992 $La_{Hf} - La_{Hf}$ different positional arrangements in the 96-atomic supercell, although only the symmetric nonequivalent arrangements as listed in Table 1 are computed with DFT. This was achieved by weighting the symmetric nonequivalent arrangements with their number of symmetry equivalent possibilities.

Experimental measurements on doped HfO_2 show that 3 f.u.% to 5 f.u.% Si-doped HfO_2[37] and 7−15 f.u.% La-doped HfO_2[49] is ferroelectric. However, even the defect arrangements with the lowest energy of the statistic (manufacturing processes with large thermal budget) in Fig. 2 alone cannot explain the stabilization of the p-o-phase, which is believed to be responsible for the ferroelectricity, over the o-phase and m-phase. As discussed in other studies[25–27,45,52–54] for several dopants, there are mechanisms to exclude the o-phase and m-phase in thin films and doping affects only the competition between t-phase and p-o-phase under these conditions. A more detailed discussion of these mechanisms for doped HfO_2 with La and Si can be found in the supplementary materials. It should be noted that for La and Si, an in-depth discussion of the phase stability was held in the publications of Materlik et al.[26] and Künneth et al.,[27] respectively, and the current study confirms their findings qualitatively.

DISCUSSION

As the calculated energy distributions are not Gaussian, we use median instead of mean quantities. Figure 3a–d illustrates the DFT energy medians of Fig. 2 of the four defects against their defect concentration which turn out to be almost linear, following the linear response rules. This linear response of La doping up to 12.5 f.u.% found here (Fig. 3a) with the statistical approach is in contrast to the nonlinearity of the DFT energies of the t-phase for 12.5 f.u.% defect concentration which was recently found by Materlik et al.[26] considering the lowest-energy structures

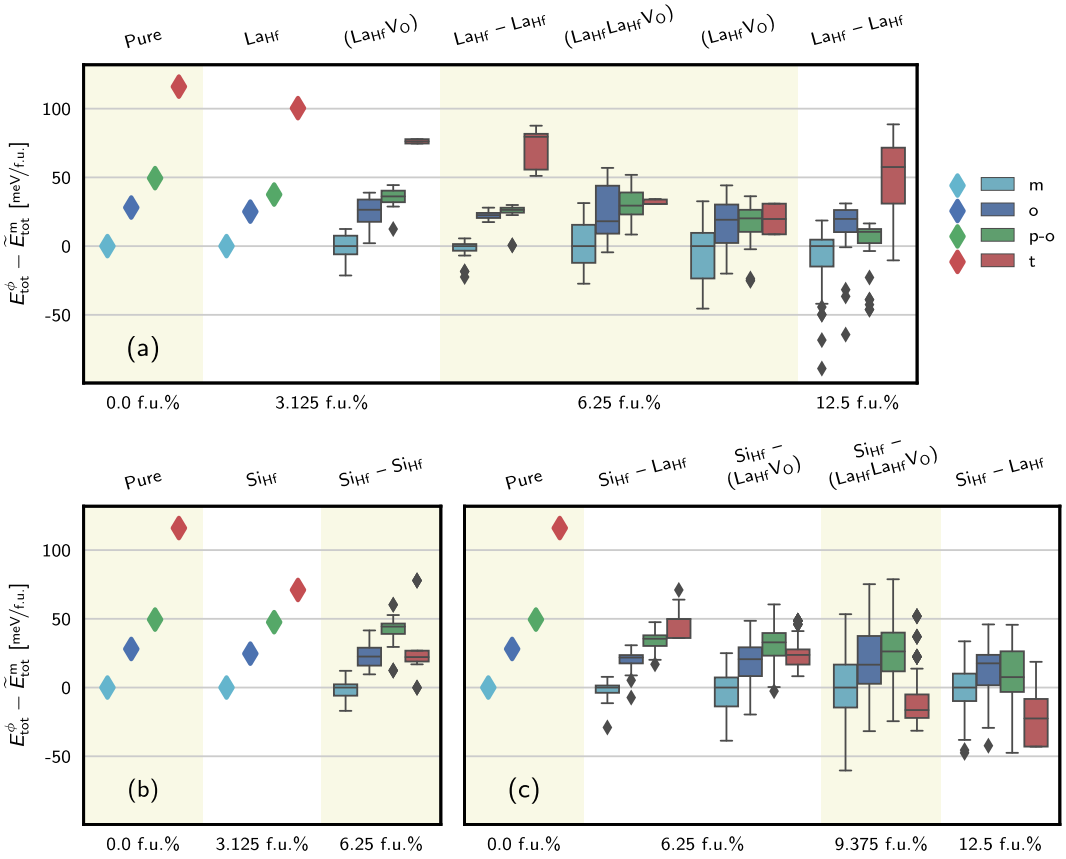

Fig. 2 The total energies of the La defects **a**, Si defects **b**, and their mixtures **c** in HfO_2. The big colored diamonds mark single data points. The box diagrams depict the distributions of data points: the colored box body marks the lower and upper quartiles, the line in the box is the median, the whiskers are the lowest and the highest values neglecting the outliers, which are marked by small black diamonds. The quartets of colored diamonds or box diagrams represent the *sets*, as described in Table 1. They are sorted in an ascending order of concentration along the horizontal axis. The background color associates the *sets* with defect concentration labels at the bottom edge and the defect type itself is labeled at the top edge. The four colors mark different crystal phases as described in the legend. All *sets* are referenced to the corresponding m-phase data point or distribution median $\tilde{E}^{m}_{tot}$

(see supplementary materials). With the statistical approach, the p-o-phase becomes bulk stable at 15.5 f.u.%, if extrapolated.

The energies of the $(La_{Hf}V_O)$ defect in Fig. 3b exhibit a slight nonlinearity in the DFT energies with the defect concentration, especially the o- and t-phases. Two possible explanations are conceivable: (i) the $(La_{Hf}V_O)$ defect in HfO_2 may induce nonlinear effects already at lower doping concentrations than Si. Or (ii), the statistic behind the data points of o- and t-phases at 6.25 f.u.% is smaller than for the La_{Hf} defect of the same concentration. The reason for a smaller statistic of $(La_{Hf}V_O)$ is the exclusion of some computations transformed to other phases as discussed in the section "Phase transformation detection during structural relaxation". Nevertheless, the nonlinearity can be considered as not significant.

Künneth et al.[27] have found nonlinear effects of DFT energies of Si_{Hf}-doped HfO_2 at 6.25 f.u.% doping concentration. They only used three different computations (for the three spatial directions) for 6.25 f.u.% doping and chose the lowest energy in the discussion. In Fig. 3c the DFT energies for the 6.25 f.u.% Si_{Hf} defect are the medians of several tens of computations. Similar than in the case of the La_{Hf} defect, this larger statistic of Si_{Hf} results in linear DFT energies for the p-o- and t-phases with increasing doping concentration. Surprisingly, only the t-phase reacts on the increasing amount of Si_{Hf} defects and the crossing of the m- and t-lines can be extrapolated at 8 f.u.%. At this concentration the t-phase becomes the phase of the lowest energy, giving an explanation for the experimental observation of Si-doped HfO_2 crystallizing in t-phase.[55]

Figure 3d depicts the medians of the DFT energies of Si_{Hf}—La_{Hf}-doped HfO_2. The medians show the linear dependency of the energy evolution with the doping concentration of all phases, except for the p-o-phase. The argument of an insufficient statistics cannot explain this nonlinearity because the size of the statistic for Si_{Hf}—La_{Hf} mixture is the same as for the Si_{Hf} or La_{Hf} *sets* at equal concentrations. However, because this is the first defect substituting two Hf discussed, Si_{Hf} and La_{Hf} can interact with each other resulting in the steeper change of the total energy of the p-o-phase from 6.25 to 12.5 f.u.% Si_{Hf} La_{Hf}.

Yet another interesting question is why do the 3.125 f.u.% energies of the La_{Hf} and Si_{Hf} defects lie on the line with another data points in the concentration series. For pure HfO_2, there is only one possible structure for each crystal phase. The 6.25 and 12.5 f.u.% data points are backed by statistics of several hundred defect arrangements. On the contrary, the 3.125 f.u.% data points are also represented by a single structure for each phase. Though it is possible to generate statistics in a similar way as is done for higher concentrations. For this, two substitutional defects in a 192-atomic supercell need to be considered. Nevertheless, it seems that this huge number of structures can be represented by only one structure with one substitutional defect in a 96-atomic supercell. The reason for that is that this defect creates not only a homogeneously doped HfO_2 matrix, given the periodic boundary conditions, but this homogeneity is also almost isotropic, because

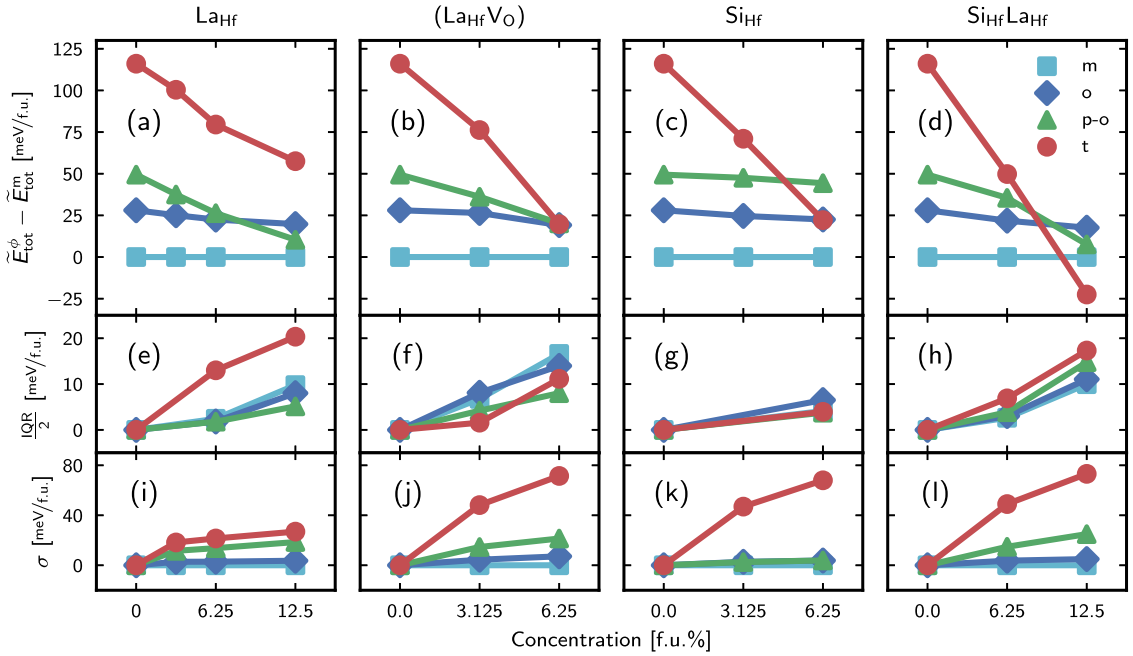

Fig. 3 Total energies against the defect concentration plots for **a** La_{Hf}, **b** $(La_{Hf}V_O)$, **c** Si_{Hf}, and **d** $Si_{Hf}La_{Hf}$ defects in HfO_2. All the points are extracted from Fig. 2 for a better representation of the linear dependencies. The points for the pure HfO_2 and 3.125 f.u.% La_{Hf} and Si_{Hf} defect concentration are single data points. All other points in the plots are the medians of the corresponding distributions. The second row of plots **e**–**h** shows half the interquartile range IQR(*E*)/2, as a measure of energy variations caused by dopant interaction, versus defect concentration for the four defects. The third row of plots **i**–**l** shows $\sigma(\tilde{E})$, caused by dopant concentration, versus defect concentration for the four defects

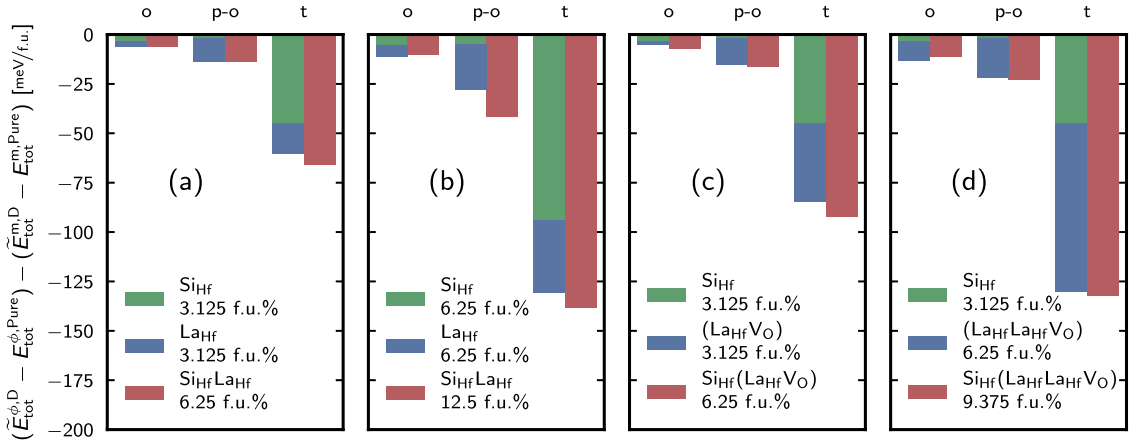

Fig. 4 The effect of the defects on the crystal phases for **a**, **b** $Si_{Hf}La_{Hf}$, **c** $Si_{Hf}(La_{Hf}V_O)$, and **d** $Si_{Hf}(La_{Hf}La_{Hf}V_O)$ mixtures and their constituents in HfO_2. Bars represent the change of the total energies of the o-, p-o-, and t- phases due to the defect, given by $(\tilde{E}^{\phi,D}_{tot} - E^{\phi,Pure}_{tot})$, with respect to the m-phase, the $(\tilde{E}^{m,D}_{tot} - E^{m,Pure}_{tot})$ part. The red bars depict the effect of the mixtures and the green and blue bars depict the effect of their constituents. The bars are drawn using the medians of the statistics

all three lattice constants of the 96-atomic supercell of any HfO_2 phase are approximately 10 Å long. So each defect has six defects next to it in a distance of 10 Å. 6.25 f.u.% doped structure can also be created putting one defect in a 48-atomic supercell. This also leads to homogeneous doping, but one lattice constant of the supercell is twice as short as the two others. This results in a strong anisotropy of the defect density. This anisotropy is canceled out when the statistics of several hundreds of locally inhomogeneous defect arrangements are considered.

Figure 3d shows that the crystal phase total energies go linearly with defect concentration to a certain extent also for a mixture of two defects. An interesting question is whether the effects of single defects in the mixture on the total energy can be superimposed. The effect of a defect on the total energy of a crystal phase is defined by the energy difference of the doped HfO_2 structure and the undoped HfO_2 in this phase. For instance, the effect of 3.125 f.u.% Si_{Hf} doping on the t-phase is 71 meV/f.u. – 116 meV/f.u. = −45 meV/f.u. (middle and left red points in Fig. 3c). Similarly, the effect of 3.125 f.u.% La_{Hf} on the t-phase is −16 meV/f.u. (see Fig. 3a). These two numbers are represented as green and blue bars in Fig. 4a. The sum of the two effects is approximately equal to the effect of 6.25 f.u.% Si_{Hf}–La_{Hf}-doped t-phase, which is equal to −66 meV/f.u. (see Fig. 3d) and represented by the red bar in Fig. 4a. The same holds for the o- and p-o-phases. The m-phase is generally not depicted in Fig. 4, because each *set* is referenced

to its m-phase and the effect of any defect on the total energy of the m-phase is always zero.

Figure 4b supports the argument for the nonlinearity of the p-o-line in Fig. 3d. For the o- and t-phases, the green and blue bars of the Si_{Hf} and La_{Hf} defects approximately sum up to the red bar of the Si_{Hf}−La_{Hf} mixture. Thus, the mixture constituents do not interact with each other in these crystal phases. On the contrary, the red p-o-phase bar of the mixture is 50% higher than the sum of the green and blue bars of the constituents. Consequently, the Si_{Hf}−La_{Hf} defects start to interact at 12.5 f.u.% and exert a stronger effect on the stability of the p-o-phase. Both Figs. 3d and 4b visualize it from two different approaches.

The effects superposition can also be shown for more complicated defects. Figure 4c shows that the effect on the crystal phase total energies of freely distributed Si_{Hf} and ($La_{Hf}V_O$) defects with the total concentration of 6.25 f.u.% is given by the sum of the contribution of the single defects with 3.125 f.u.% concentration each. Figure 4d reveals the same for freely distributed Si_{Hf}−($La_{Hf}La_{Hf}V_O$) defects pair at 9.375 f.u.%.

This finding allows the assumption that the effect of a mixture of two defects on the phase total energies can be approximated by the sum of the effects of its constituents. This again can be formulated as the appearance of Vegard's rule.

A crucial point in the computation of defects in periodic DFT calculations is the interaction of the incorporated defects, which differs for their concentration and distribution. For sufficient dilute dopant concentrations, no interaction and energetic influence are expected. Differently, for denser concentrations and possible enforced defect distributions (i.e. in the case of ALD manufactured films), in which defects in denser areas interact while defects in diluted areas do not. Generally speaking, the interaction increases with the point defect density, which is determined by the manufacturing process. Attempting to quantify these interactions, formation energies E_f of the single La and Si defect in HfO_2 in the t-phase are computed for three different supercell sizes and illustrated in Fig. 5. The larger the supercell, the greater the distance to the next dopant. The results evidence that the formation energy saturates at a $2\times2\times2$ supercell meaning that defects at distances larger than 1 nm do not interact, which reflects a sufficiently dilute concentration. In the distance range of 0.5−1 nm, the defects do interact, which is precisely the distance range of two defects in the 48- or 96-atomic supercell computed in this study. The natural length scale of our coarse-grained model for the interaction energy variation turns out to be $\xi = 1$ nm. Since the energies of all positional arrangements of dopants in the 48- and 96-atomic unit cells in Table 1 are computed, the distance-dependent interactions of the defects are already included in the statistic as error bars shown in Fig. 2. Therefore, we can argue that the IQRs in Fig. 2, which are illustrated separately in Fig. 3e−h, are caused by the dopant−dopant interactions and increase with increasing doping concentration. Note that the IQRs in Fig. 2 do not contain a statistical contribution $\sigma(\overline{E})$. These arise from a statistical variation $\sigma(\overline{c})$ of the averaged concentration and

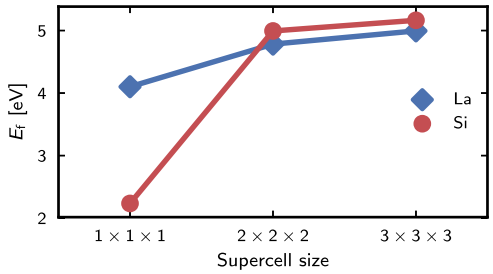

Fig. 5 Formation energies of La and Si defects in HfO_2 t-phase in dependence on the supercell size, according to Eq. (1). $2\times2\times2$ corresponds to $\xi = 1$ nm

depend on the sensitivity as $\sigma(\overline{E}) = \frac{\partial\overline{E}}{\partial c}\sigma(\overline{c})$. Figure 3i–l contains these values. The concentration dependence has the same interaction length ξ as the individual dopants because a concentration gradient is modeled with a similar supercell with inserted dopant atoms.

In the introduction, three different manufacturing processes were discussed, revealing three different dopant distributions, see also Fig. 1. Since we have shown in the previous paragraphs that the energy evolution with increasing doping concentration is linear and an additional energy variation resulting from a dopant−dopant distance-dependent interaction must be included, we can decide which energy must be considered for specific manufacturing processes. In the case of the ceramics process, in which a large thermal budget is available during the crystallization process, the structure is expected to be in or close to the thermodynamic equilibrium (lowest-energy structures). Mostly structures with low energy are realized and the lower whiskers in Fig. 2 are essential for the energy and phase stability. Moreover, the energy variations in the film from dopant−dopant interactions are expected to be very shallow.

In the case of CSD-manufactured films, the dopants can be considered to be homogeneously distributed after processing because of the liquid precursor and the low thermal budget during the anneal. Therefore, all positional arrangements would be randomly realized in the film. Overall, the energy and the phase stability of the CSD-manufactured film would be determined by the energy median, as shown in Fig. 3a–d. The energy variations in the film, possibly causing nanoregions, are a superposition from concentration variation as shown in Fig. 3i–l and dopant interaction in Fig. 3e–h. The dopant distribution of ALD-manufactured films is more complex. Doping on the level of 6.25 f.u.% is realized by a single deposition cycle of an Si precursor followed by about 15 deposition cycles of Hf. Since a single layer realizes only a fraction of a monolayer, the Si concentration is modeled as a 1-nm-thick region of 12.5 f.u.% Si. It is experimentally shown[36,37] that metal movements are suppressed by the low thermal budget during the anneal. The dopant distribution orthogonal to the surface of the film would lead to a wavy energy evolution superimposed by energy variations. But the energy variations are much stronger in the dopant layers compared to CSD due to the concentration dependence of the variation shown in Fig. 3e–l, increasing the possibility for nanoregions.

Figure 1 shows the nanoscaled energy variations in CSD and ALD Si-doped HfO_2 films in the p-o- and t-phases due to the local doping distribution inhomogeneities in a coarse-grained representation in $1\times1\times1\,nm^3$ units. For the CSD film, a constant average concentration of 6.25 f.u.% is chosen that corresponds to two Si atoms per discretization unit. For each unit the number of Si atoms is randomly chosen in accordance to the Poisson distribution resulting in the variance of the local concentration $\sigma(\overline{c})$ and hence the energy $\sigma(\overline{E})$ (Fig. 3k). The additional energy variation stemming from the defect−defect interaction is drawn from an assumed normal distribution with the standard deviation equal to IQR(E)/2 (Fig. 3g). For the ALD films, the layers of 1 nm thickness are chosen. Within each layer, the doping concentration is constant on average, while along the growth direction it alternates between 0 and 12.5 f.u.%. In the undoped layers, both types of the energy variation are equal to zero. For the doped layers, the variations are calculated in the same manner as for the CSD film with appropriate $\sigma(\overline{E})$ and IQR(E)/2. Finally, both energy variations are added to the energy profile originating from the average doping concentration, which is constant for the CSD and alternating for the ALD film. Owing to the independent total energy of the p-o-phase on the defect concentration, the energy variation $\sigma(\overline{E})$ is small in comparison to IQR(E)/2 (Fig. 3g, k). Hence, the defect−defect interaction is the main contributor to the energy variance of the p-o-phase for both the CSD and ALD Si-doped HfO_2 films. On contrary, for the t-phase the energy

variance is mainly based on the local variations of the defect concentration.

For instance, the Curie temperature is broadened during the transformation from the polar to the nonpolar phase in experimental measurements,[41,42] possibly owing to the nanoscaled energy domains. Due to the high crystal symmetry of the t-phase its Helmholtz free energy is decreasing faster with the increasing temperature if compared to the p-o-phase. Therefore, the rising temperature results in the downwards shift of the energy landscape of the t-phase with respect to the p-o-phase, which leads to the gradual switching of the domains from the p-o-phase to the t-phase.

The range of interaction of La or/and Si dopants in HfO_2, relevant for the stability of the ferroelectric p-o-phase relative to the t-phase, has been calculated as $\xi = 1$ nm. High-throughput calculations with 1 nm-sized supercells for all relevant crystal phases produce low energy structures, median energy values, and unexpectedly large energy variation IQR(E), caused by the dopant interaction. The current approach is an improvement to our previous studies because it now considers big statistics and allows to relate the data to different production processes. As there is additionally a statistical deviation $\sigma(\bar{E})$ in any control volume, the detection of IQR(E) seems only possible in a coarse-grained approach with discretization units of size ξ. When evaluating the data, the dependence of median energies on the average concentration turns out to be almost linear, even in the mixture of defects, resembling Vegard's rule. The relevance of the energy variation is considered with regard to the competition between the dielectric t-phase and ferroelectric p-o-phase. As nanoregions in this material have been suggested and nanolaminate effects have been identified, the theoretical results obtained here are an important step to fundamentally substantiate the experimental findings. The formation of nanoregions with different phases requires interphase boundaries with additional energy contributions. The related and experimentally observed effect of the Curie temperature broadening can be investigated utilizing the Monte Carlo method. The condition for the appearance of the interphase boundaries and diffuse phase transition with increasing temperature are the topics of further research.

METHODS

Geometries setup for the calculations

The primitive unit cells for the m-, o-, p-o-, and t-crystal phases consist of 12, 24, 12, and 6 atoms, respectively. For convenience, a 12-atomic cell for the t-phase can be constructed through a coordinate transformation. The c-phase is omitted, because it always disintegrates into the t-phase during the ionic force relaxation. It is also expected, because the c-phase is stabilized dynamically at high temperatures and has disadvantageous energy at 0 K, a condition of DFT calculations. In this study, supercells consisting of 48 and 96 atoms are considered. For the m-, p-o- and t-phases a $2\times2\times2$ supercell and for the o-phase a $1\times2\times2$ supercell sum up to 96 atoms. There are, though, three possible orientations for a 48-atomic supercell for m-, p-o-, and t- phases: $1\times2\times2$, $2\times1\times2$ or $2\times2\times1$. For the o-phase only two orientations $1\times1\times2$ or $1\times2\times1$ are possible due to the double amount of atoms in the primitive cell.

The number of possible arrangements of two substitutional dopants on the metal sites in, for instance, a 96-atomic supercell with 32 Hf atoms is $32\times31 = 992$. Due to the symmetry, a lot of these arrangements are equal. Hence, not for all possible arrangements, a DFT calculation needs to be performed. In a supercell of any size metal sites in all here considered crystal phases are equivalent by symmetry. It does not play any role on which metal site the first substitutional dopant is placed. The presence of this dopant in the supercell though reduces the spatial symmetry, so the remaining 31 metal sites for the second substitutional dopant are in general not equivalent. For this reason, at most, 31 DFT calculations are needed for covering the whole space of arrangements of two substitutional dopants on the metal sites in a 96-atomic supercell. For the t-phase this number is further reduced due to the high symmetry of the crystal phase compared to the other three phases. The number of needed computations is also reduced if the two substitutional dopants are of the same kind, and so indistinguishable.

Similar arguments hold for placing an oxygen vacancy in supercells during the structures set up for calculations. In m-, o- and p-o-phases there are only two by symmetry nonequivalent oxygen sites, regardless of the supercell size. In the t-phase all oxygen sites are equal by symmetry.

Freely distributed La_{Hf}–La_{Hf}–V_O defects in, for instance, a 96-atomic p-o-supercell require almost 2000 calculations, even after reduction of arrangement space due to the symmetry. Further reduction can be made assuming that a tight complex ($La_{Hf}La_{Hf}V_O$) is build due to the electrostatic attraction. Any oxygen or hafnium site in any phase has four hafnium or eight oxygen next-neighbor sites, respectively.

In comparison to 96-atomic supercell, a 48-atomic supercell can be differently oriented. For instance, $16\times15\times3 = 720$ arrangements of two dopants of a different kind in a 48-atomic p-o-supercell with 16 metal sites are possible. The number of needed calculations can be reduced, though, in the same manner as discussed above.

Defect formation energy

For Fig. 5, the defect formation energies in HfO_2 supercells of different size are calculated. The structures for the three different supercell sizes are prepared in a special way and only single-shot calculations of the total energies without the ionic relaxation are performed. The setup procedure for the structure is as follows. First, a 12-atomic cell in t-phase with one Hf substituted by a defect is relaxed, which changes the lattice constants and the oxygen atoms around the defect form a characteristic tetrahedron arrangement. While keeping the reduced coordinates of the relaxed doped structure intact, the lattice constants are set to the values of the pure HfO_2 t-phase cell in order to build pre-relaxed 48- and 96-atomic doped cells. Second, an HfO_2 supercell in the t-phase of needed size is constructed and one 12-atomic section is substituted by the relaxed and scaled cell with the defect prepared in the first step. The result is a doped HfO_2 supercell, structurally mostly equal to the pure t-phase with adjusted crystal structure in the vicinity of the defect. The formation energy of a substitutional defect in the HfO_2 matrix is the energy for replacing one Hf with the doping atom. Additionally, the chemical potentials of Hf and the dopant are also needed. The chemical potential of Hf is the energy for incorporating the removed Hf into some reference structure like metallic hafnium. On the contrary, the chemical potential of the dopant gives the energy for creation of one free atom from some reference structure. Hence, the formation energy of a defect is given as follows:

$$E_f^D = E_{tot}^D - E_{tot}^{Pure} - \mu^D + \mu^{Hf}, \quad (1)$$

where μ^D and μ^{Hf} are the chemical potentials of La, Si and Hf atoms, which are calculated from pure lanthanum, silicon and hafnium metals, respectively.

Phase transformation detection during structural relaxation

In total, more than 2500 DFT calculations are needed for this study. For each doped structure, a structural relaxation must be performed, which leads to changes of the supercell and the positions of all atoms compared to the pure HfO_2 host. None of the structures can retain its initial space group symmetry, not only due to the introduced doping defects but also due to the structural deformation after the relaxation. Only by means of certain characteristics of the relaxed structures, like lattice constants, their ratios, lattice angles, positions of the oxygen atoms with respect to the metal atoms, they can be related to a certain crystal phase. Furthermore, a doped structure can even transform from its initial phase into another one during the relaxation of ionic forces. Such transformations must be filtered out for further evaluation of the calculations.

It is rather a rare case that a structure transforms into another crystal phase. Therefore, it is sufficient enough to compare calculations with each other within a single *set* to filter out the cases of the phase transformation.

The m- and o-phases have greater supercell volume than the p-o- and t-phases. Additionally, the m-phase has one sharp angle and the o-phase has only right angles. The relaxed structures comparing with each other can be unambiguously classified into the m- or o-phase by these two characteristics.

The distinction between the p-o- and t-phases is more complicated. We have found empirically that the Hirshfeld charge analysis,[56] which can be performed by FHI-AIMS, gives a good criterion for distinguishing the p-o-phase from the t-phase. For the m-, o-, and t-phases of the pure HfO_2, the vector sum of the electron dipole moments is a zero-vector. For the

p-o-phase this is a vector of 0.01856 eÅ/f.u. length, which is chosen to be a reference. The doped m-, o-, and t-supercells have a finite dipole moments sum due to the presence of the defect, of course. Nevertheless, these phases can still be clearly separated from the doped p-o-supercells.

All the described procedures can be performed in an automated manner, which not only saves evaluation time but also excludes the subjective nature of the human eye if the classification of the relaxed structures were performed by hand.

DFT calculations

All DFT calculations in this paper were performed with the all-electron code FHI-AIMS[57] using the local density approximation[58] (LDA). FHI-AIMS uses tabulated numeric, atom-centered orbitals as the basis set. The simulations were conducted using the tight settings of basis set additionally enabling the complete first and second tiers for the atom species. The convergence criteria were set to 1×10^{-4} and 1×10^{-2} eV/Å for electronic and ionic forces, respectively. FHI-AIMS utilizes the Monkhorst-Pack[59] grid for the k-point grid definition. For supercells consisting of 96 atoms (95 with a vacancy), a $2\times2\times2$ grid was chosen. For supercells consisting of 48 atoms (47 with a vacancy) $4\times2\times2$, $2\times4\times2$ or $2\times2\times4$ grid was chosen depending on the orientation of the supercell, as discussed in the section "Geometries setup for the calculations". All these settings were found to be sufficient in a convergence study.

DATA AVAILABILITY

The datasets for the study are available from the corresponding authors upon request.

ACKNOWLEDGEMENTS

The Deutsche Forschungsgemeinschaft (German Research Foundation) has funded this research in the frame of the project Inferox II (Project MI 1247/11-2). The authors gratefully acknowledge the Gauss Centre for Supercomputing e.V. (www.gauss-centre.eu) for providing computing time on the GCS Supercomputer SuperMUC at Leibniz Supercomputing Center (LRZ, www.lrz.de) under grant: pr53xo. This work was supported by the Deutsche Forschungsgemeinschaft (German Research Foundation (DFG)—Project 393121356) and the Munich University of Applied Sciences (MUAS) through the Open Access Publishing program.

AUTHOR CONTRIBUTIONS

M.F. and A.K. designed the study and the methodology. M.F. carried out the calculations, evaluated the results and produced the figures. All authors analyzed the findings and wrote the manuscript. M.F. is guarantor of the presented study.

ADDITIONAL INFORMATION

Supplementary information accompanies the paper on the *npj Computational Materials* website (https://doi.org/10.1038/s41524-018-0133-4).

Competing interests: The authors declare no competing interests.

Publisher's note: Springer Nature remains neutral with regard to jurisdictional claims in published maps and institutional affiliations.

REFERENCES

1. Keyes, R. W. Physical limits of silicon transistors and circuits. *Rep. Progress. Phys.* **68**, 2701–2746 (2005).
2. Böscke, T. S., Müller, J., Bräuhaus, D., Schröder, U. & Böttger, U. Ferroelectricity in hafnium oxide thin films. *Appl. Phys. Lett.* **99**, 102903 (2011).
3. Toriumi, A. (Invited) High-k, higher-k and ferroelectric HfO_2. *ECS Trans.* **80**, 29–40 (2017).
4. Park, M. H. et al. Ferroelectricity and antiferroelectricity of doped thin HfO_2-based films. *Adv. Mater.* **27**, 1811–1831 (2015).
5. Ahnert, S. E., Grant, W. P. & Pickard, C. J. Revealing and exploiting hierarchical material structure through complex atomic networks. *npj Comput. Mater.* **3**, 35 (2017).
6. Kaski, K., Binder, K. & Gunton, J. D. A study of a coarse-grained free energy functional for the three-dimensional Ising model. *J. Phys. A: Math. General.* **16**, L623–L627 (1983).
7. Cross, L. E. Relaxor ferroelectrics. *Ferroelectrics* **76**, 241–267 (1987).
8. Krogstad, M. J. et al. The relation of local order to material properties in relaxor ferroelectrics. *Nat. Mater.* **17**, 718–724 (2018).
9. Xu, G., Wen, J., Stock, C. & Gehring, P. M. Phase instability induced by polar nanoregions in a relaxor ferroelectric system. *Nat. Mater.* **7**, 562–566 (2008).
10. Seyf, H. R. et al. Rethinking phonons: the issue of disorder. *npj Comput. Mater.* **3**, 49 (2017).
11. Bokov, A. A. & Ye, Z. G. Recent progress in relaxor ferroelectrics with perovskite structure. In Lang, S. B. & Chan, H. L. W. (eds.) *Frontiers of Ferroelectricity: A Special Issue of the Journal of Materials Science* 31–52 (Springer US, Boston, MA, 2007).
12. Groszewicz, P. B. et al. Reconciling local structure disorder and the relaxor state in $(Bi_{1/2}Na_{1/2})TiO_3$-$BaTiO_3$. *Sci. Rep.* **6**, 31739 (2016).
13. Azadmanjiri, J. et al. A review on hybrid nanolaminate materials synthesized by deposition techniques for energy storage applications. *J. Mater. Chem. A* **2**, 3695–3708 (2014).
14. Lee, G., Fuentes-Fernandez, E. M. A., Lian, G., Katiyar, R. S. & Auciello, O. Hetero-epitaxial $BiFeO_3$/$SrTiO_3$ nanolaminates with higher piezoresponse performance over stoichiometric $BiFeO_3$ films. *Appl. Phys. Lett.* **106**, 022905 (2015).
15. Weeks, S. L., Pal, A., Narasimhan, V. K., Littau, K. A. & Chiang, T. Engineering of ferroelectric HfO_2–ZrO_2 nanolaminates. *ACS Appl. Mater. Interfaces* **9**, 13440–13447 (2017).
16. Shvartsman, V., Dkhil, B. & Kholkin, A. Mesoscale domains and nature of the relaxor state by piezoresponse force microscopy. *Annu. Rev. Mater. Res.* **43**, 423–449 (2013).
17. Li, F. et al. The origin of ultrahigh piezoelectricity in relaxor-ferroelectric solid solution crystals. *Nat. Commun.* **7**, 13807 (2016).
18. Müller, J. et al. Ferroelectricity in simple binary ZrO_2 and HfO_2. *Nano Lett.* **12**, 4318–4323 (2012).
19. Starschich, S., Griesche, D., Schneller, T. & Böttger, U. Chemical solution deposition of ferroelectric hafnium oxide for future lead free ferroelectric devices. *ECS J. Solid State Sci. Technol.* **4**, P419–P423 (2015).
20. Starschich, S. & Boettger, U. An extensive study of the influence of dopants on the ferroelectric properties of HfO_2. *J. Mater. Chem. C* **5**, 333–338 (2017).
21. Shimizu, T. et al. The demonstration of significant ferroelectricity in epitaxial Y-doped HfO_2 film. *Sci. Rep.* **6**, 32931 (2016).
22. Zhu, H., Tang, C., Fonseca, L. R. C. & Ramprasad, R. Recent progress in ab initio simulations of hafnia-based gate stacks. *J. Mater. Sci.* **47**, 7399–7416 (2012).
23. Barabash, S. V. Prediction of new metastable HfO_2 phases: toward understanding ferro- and antiferroelectric films. *J. Comput. Electron.* **16**, 1227–1235 (2017).
24. Xu, L. et al. Kinetic pathway of the ferroelectric phase formation in doped HfO_2 films. *J. Appl. Phys.* **122**, 124104 (2017).
25. Materlik, R., Künneth, C., Mikolajick, T. & Kersch, A. The impact of charge compensated and uncompensated strontium defects on the stabilization of the ferroelectric phase in HfO_2. *Appl. Phys. Lett.* **111**, 082902 (2017).
26. Materlik, R., Künneth, C., Falkowski, M., Mikolajick, T. & Kersch, A. Al-, Y-, and La-doping effects favoring intrinsic and field induced ferroelectricity in HfO_2: a first principles study. *J. Appl. Phys.* **123**, 164101 (2018).
27. Künneth, C., Materlik, R., Falkowski, M. & Kersch, A. Impact of four-valent doping on the crystallographic phase formation for ferroelectric HfO_2 from first-principles: implications for ferroelectric memory and energy-related applications. *ACS Appl. Nano Mater.* **1**, 254–264 (2018).
28. Robertson, J. & Wallace, R. M. High-K materials and metal gates for CMOS applications. *Mater. Sci. Eng. R: Rep.* **88**, 1–41 (2015).
29. Mueller, W. et al. Challenges for the DRAM cell scaling to 40 nm. In *IEEE International-Electron Devices Meeting, 2005*. IEDM Technical Digest, Vol. 1, 336−339 (IEEE, 2005).
30. Parkes, M. A. et al. The atomistic structure of yttria stabilised zirconia at 6.7 mol%: An ab initio study. *Phys. Chem. Chem. Phys.* **18**, 31277–31285 (2016).
31. Sang, X., Grimley, E. D., Schenk, T., Schroeder, U. & Lebeau, J. M. On the structural origins of ferroelectricity in HfO_2 thin films. *Appl. Phys. Lett.* **106**, 162905 (2015).
32. Mikolajick, T., Slesazeck, S., Park, M. H. & Schroeder, U. Ferroelectric hafnium oxide for ferroelectric random-access memories and ferroelectric field-effect transistors. *MRS Bull.* **43**, 340–346 (2018).
33. Predith, A., Ceder, G., Wolverton, C., Persson, K. & Mueller, T. Ab initio prediction of ordered ground-state structures in ZrO_2-Y_2O_3. *Phys. Rev. B—Condens. Matter Mater. Phys.* **77**, 144104 (2008).
34. Stolichnov, I. et al. Genuinely ferroelectric sub-1-volt-switchable nanodomains in $Hf_xZr_{(1-x)}O_2$ ultrathin capacitors. *ACS Appl. Mater. Interfaces*. **10**, 30514–30521 (2018).
35. Mittmann, T. et al. Optimizing process conditions for improved $Hf_{1-x}Zr_xO_2$ ferroelectric capacitor performance. *Microelectron. Eng.* **178**, 48–51 (2017).
36. Lomenzo, P. D. et al. The effects of layering in ferroelectric Si-doped HfO_2 thin films. *Appl. Phys. Lett.* **105**, 072906 (2014).

37. Richter, C. et al. Si doped hafnium oxide—a "fragile" ferroelectric system. *Adv. Electron. Mater.* **3**, 1700131 (2017).
38. Starschich, S. & Böttger, U. Doped ZrO_2 for future lead free piezoelectric devices. *J. Appl. Phys.* **123**, 044101 (2018).
39. Pešić, M. et al. Physical mechanisms behind the field-cycling behavior of HfO_2-based ferroelectric capacitors. *Adv. Funct. Mater.* **26**, 4601–4612 (2016).
40. Pešić, M. et al. A computational study of hafnia-based ferroelectric memories: from ab initio via physical modeling to circuit models of ferroelectric device. *J. Comput. Electron.* **16**, 1236–1256 (2017).
41. Hoffmann, M. et al. Ferroelectric phase transitions in nanoscale HfO_2 films enable giant pyroelectric energy conversion and highly efficient supercapacitors. *Nano Energy* **18**, 154–164 (2015).
42. Park, M. H. et al. Origin of temperature-dependent ferroelectricity in Si-doped HfO_2. *Adv. Electron. Mater.* **4**, 1700489 (2018).
43. Lee, C.-K., Cho, E., Lee, H.-S., Hwang, C. S. & Han, S. First-principles study on doping and phase stability of HfO_2. *Phys. Rev. B* **78**, 012102 (2008).
44. Fischer, D. & Kersch, A. Stabilization of the high-k tetragonal phase in HfO_2: the influence of dopants and temperature from ab initio simulations. *J. Appl. Phys.* **104**, 084104 (2008).
45. Batra, R., Huan, T. D., Rossetti, G. A. & Ramprasad, R. Dopants promoting ferroelectricity in hafnia: insights from a comprehensive chemical space exploration. *Chem. Mater.* **29**, 9102–9109 (2017).
46. Fischer, D. & Kersch, A. The effect of dopants on the dielectric constant of HfO_2 and ZrO_2 from first principles. *Appl. Phys. Lett.* **92**, 012908 (2008).
47. Parkes, M. A. et al. Chemical descriptors of yttria-stabilized zirconia at low defect concentration: An ab initio study. *J. Phys. Chem. A* **119**, 6412–6420 (2015).
48. Curtarolo, S. et al. The high-throughput highway to computational materials design. *Nat. Mater.* **12**, 191–201 (2013).
49. Schroeder, U. et al. Lanthanum-doped hafnium oxide: a robust ferroelectric material. *Inorg. Chem.* **57**, 2752–2765 (2018).
50. Buragohain, P. et al. Nanoscopic studies of domain structure dynamics in ferroelectric La:HfO_2 capacitors. *Appl. Phys. Lett.* **112**, 222901 (2018).
51. Grimley, E. D., Schenk, T., Mikolajick, T., Schroeder, U. & LeBeau, J. M. Atomic structure of domain and interphase boundaries in ferroelectric HfO_2. *Adv. Mater. Interfaces* **5**, 1701258 (2018).
52. Künneth, C., Materlik, R. & Kersch, A. Modeling ferroelectric film properties and size effects from tetragonal interlayer in $Hf_{1-x}Zr_xO_2$ grains. *J. Appl. Phys.* **121**, 205304 (2017).
53. Materlik, R., Künneth, C. & Kersch, A. The origin of ferroelectricity in $Hf_{1-x}Zr_xO_2$: a computational investigation and a surface energy model. *J. Appl. Phys.* **117**, 134109 (2015).
54. Batra, R., Huan, T. D., Jones, J. L., Rossetti, G. & Ramprasad, R. Factors favoring ferroelectricity in hafnia: a first-principles computational study. *J. Phys. Chem. C.* **121**, 4139–4145 (2017).
55. Böscke, T. S. et al. Stabilization of higher-κ tetragonal HfO_2 by SiO_2 admixture enabling thermally stable metal-insulator-metal capacitors. *Appl. Phys. Lett.* **91**, 072902 (2007).
56. Hirshfeld, F. L. Bonded-atom fragments for describing molecular charge densities. *Theor. Chim. Acta* **44**, 129–138 (1977).
57. Blum, V. et al. Ab initio molecular simulations with numeric atom-centered orbitals. *Comput. Phys. Commun.* **180**, 2175–2196 (2009).
58. Perdew, J. P. & Wang, Y. Accurate and simple analytic representation of the electron-gas correlation energy. *Phys. Rev. B* **45**, 13244–13249 (1992).
59. Monkhorst, H. J. & Pack, J. D. Special points for Brillouin-zone integrations. *Phys. Rev. B* **13**, 5188–5192 (1976).

B Article #2

Optimizing the Piezoelectric Strain in ZrO_2- and HfO_2-Based Incipient Ferroelectrics for Thin-Film Applications: An Ab Initio Dopant Screening Study

Max Falkowski and Alfred Kersch

ACS Applied Materials & Interfaces **2020** *12* (29), 32915-32924
DOI: 10.1021/acsami.0c08310

ACS APPLIED MATERIALS & INTERFACES

www.acsami.org

Research Article

Optimizing the Piezoelectric Strain in ZrO_2- and HfO_2-Based Incipient Ferroelectrics for Thin-Film Applications: An Ab Initio Dopant Screening Study

Max Falkowski and Alfred Kersch*

Cite This: *ACS Appl. Mater. Interfaces* 2020, 12, 32915−32924

Read Online

ACCESS | Metrics & More | Article Recommendations | Supporting Information

ABSTRACT: HfO_2 and ZrO_2 have increasingly drawn the interest of researchers as lead-free and silicon technology-compatible materials for ferroelectric, pyroelectric, and piezoelectric applications in thin films such as ferroelectric field-effect transistors, ferroelectric random access memories, nanoscale sensors, and energy harvesters. Owing to the environmental regulations against lead-containing electronic components, HfO_2 and ZrO_2 offer, along with AlN, $(K,Na)NbO_3$- and $(Bi_{0.5}Na_{0.5})TiO_3$-based materials, an alternative to $Pb(Zr_xTi_{1-x})O_3$-based materials, which are the overwhelmingly used ceramics in industry. HfO_2 and ZrO_2 thin films may show field-induced phase transformation from the paraelectric tetragonal to the ferroelectric orthorhombic phase, leading to a change in crystal volume and thus strain. These field-induced strains have already been measured experimentally in pure and doped systems; however, no systematic optimization of the piezoelectric activity was performed, either experimentally or theoretically. In this screening study, we calculate the ultimate size of this effect for 58 dopants depending on the oxygen supply and the defect incorporation type: substitutional or interstitial. The largest piezoelectric strain values are achieved with Yb, Li, and Na in ZrO_2 and exceed 40 pm V^{-1} or 0.8% maximal strain, which exceeds the best experimental findings by a factor of 2. Furthermore, we discovered that Mo, W, and Hg make the polar-orthorhombic phase in the ZrO_2 bulk stable under certain circumstances, which would count in favor of these systems for the ceramic crystallization process. Our work guides the development of the performance of a promising material system by rational design of the essential mechanisms so as to apply it to unforeseen applications.

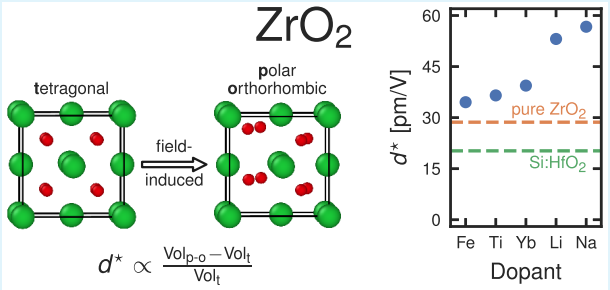

KEYWORDS: *hafnium oxide, zirconium oxide, thin film, piezoelectric, ferroelectric, antiferroelectric*

1. INTRODUCTION

Incipient HfO_2- and ZrO_2-based ferroelectrics[1] have recently stimulated materials research, as they show great potential for a vast number of applications such as next-generation memories,[2] nanotransistors,[3] tunnel junctions,[4,5] neuromorphic architectures,[6] and optical,[7] high-frequency,[8] and thermoelectric[9] devices. What is noteworthy is that the ferroelectric phase is metastable and that the desired properties are most easily obtained in thin films because of the size effect.[10,11] The thickest films reported so far have been prepared by chemical solution deposition (CSD) of up to 390 nm[12] and with an epitaxy of up to 930 nm.[13] Thinner films can be deposited by atomic layer deposition (ALD) or physical vapor deposition. Among their material properties, the piezoelectric and field-induced strain effects are the least studied.

Thin-film piezoelectrics are needed for electromechanical transducers such as thin-film bulk acoustic wave resonators and tactile sensors,[14] and the availability of a printing process is desired.[15] For comparison, the widely used aluminum nitride (AlN) thin films have a moderate piezoelectric strain coefficient of around 4 pm V^{-1}.[16] Following the pioneering work of Böscke[17] and Starschich,[12] the piezoelectric coefficient of Si-doped HfO_2 has recently been investigated more systematically by Kirbach et al.[18] and Mart et al.,[19] and they found larger piezoelectric coefficients than in conventional AlN and much larger strain values.

Piezoelectric properties are found as a combination of linear crystalline piezoelectric, nonlinear electrostrictive, domain-switching, and volume-change effects, which become large in the proximity of a phase boundary.[20] For lead zirconate titanate (PZT)- and potassium sodium niobate (KNN)-based materials, the morphotropic phase boundary between two ferroelectric phases, determined by optimization of their composition and doping, has shown large strain values with little temperature

Received: May 6, 2020
Accepted: June 15, 2020
Published: June 15, 2020

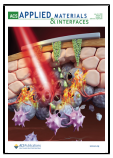

dependence. However, recently, in the search for lead-free materials such as sodium bismuth titanate (BNT), materials close to a further polymorphic phase boundary[21] (PPB) have displayed large field-induced strain effects. This has been interpreted as a volume-change effect caused by a field-induced phase transition from a paraelectric phase to a ferroelectric phase.[22] The strain values could be optimized by adding small amounts of KNN, thus moving the material system closer to the PPB, and this effort is ongoing.[20] Thin-film piezoelectrics so far have not been optimized to maximize the volume change. AlN is paraelectric, it operates without phase transition, and the addition of a dopant may increase its crystalline piezoelectric coefficient. Very few studies are available where optimization is systematically supported with ab initio simulations by calculating piezoelectric coefficients in a doped crystal.[23,24]

Pure HfO_2 and ZrO_2 are chemically similar and crystallize in the monoclinic $P2_1/c$ phase (m) at low temperatures. Under medium pressures (~10 GPa), a nonpolar orthorhombic *Pbca* phase (o) is stabilized. Differently, with the increase of the temperature, the monoclinic phase transforms into the tetragonal $P4_2/nmc$ phase (t). The ferroelectric, polar-orthorhombic $Pbc2_1$ phase (p-o) is metastable,[1] which makes these materials incipient ferroelectrics. Stabilization is possible with doping, whose most prominent examples are 3−4% Si-doped HfO_2 and 50% Zr-doped HfO_2 or $Hf_{0.5}Zr_{0.5}O_2$. Since its discovery,[17,25] field-induced phase transition has been suggested as an explanation for the double hysteresis appearing in about 5% Si-doped HfO_2 and $Hf_{1-x}Zr_xO_2$ with Zr content close to x = 1. The feasibility of such a mechanism has been investigated theoretically.[26,27]

In this paper, we will design by simulation the material properties close to the tetragonal to polar phase transition for the piezoelectric applications. These design points may also be favorable for thermoelectric applications based on the pyroelectric or electrocaloric effect. The design point for the ferroelectric application is maximal polar phase stabilization. Many experimental and theoretical studies concerned with doping have focused on the stabilization, and less on the material properties. There is no study available where the field-induced strain effects have been addressed. Doping effects show a great variety stemming from the large number of required structures, as there is a choice of the host material (HfO_2 or ZrO_2); dopant and its concentration; incorporation type (substitutional or interstitial); and the charge compensation mechanism (ionic-compensated, electronic-compensated or mixed-compensated). To date, HfO_2 has been studied experimentally with dopants[28] Si, Zr, Al, Gd, Sr, La, Y, Ge, Sc, and N and ZrO_2 with dopants Mg, In, La, Y, Ce, Ti, and Sn.[29,30] Theoretically, HfO_2 with dopants Zr, Si, Ge, Ti, Sn, C, Ce, Al, Y, La, and Sr has been investigated in detail[31−34] and more than 40 dopants using a theoretical high-throughput selection approach,[35] with a focus on phase stabilization. The dependence of the crystal volume on doping has been studied in HfO_2 for the polar phase, showing a good correlation between the theoretical and experimental values.[36] Doping effects in ZrO_2 have not been studied theoretically and constitute the focus of this study. With regard to the incorporation type, these studies assumed that large dopants are incorporated substitutionally, and only small dopants may be interstitials.[34] Finally, the allowed charge compensation mechanism is controversial for dopants other than tetravalent ones. While in ceramic process materials, an ionic compensation including oxygen vacancies is expected, ALD or CSD materials processed for a short time under oxygen-rich conditions may preserve the electronic compensation, which is metal site substitution without the associated oxygen vacancy.[32−34]

In the present work, we calculate the energy, structure, and volume of substitutionally—assuming electronic compensation only—and interstitially doped HfO_2 and ZrO_2 supercells in the crystal phases mentioned, focusing on the free energy difference between the tetragonal and polar-orthorhombic phase with field-induced transition in mind, and obtain the values for the volume change and associated strain.

2. RESULTS AND DISCUSSION

Fifty-eight species from groups 1−15 and periods 1−6 in the periodic table of elements and Ce and Yb from lanthanide series were chosen for the study. For each dopant species, we considered a substitution on a metal site and its interstitial incorporation at nominal concentrations of 3.125 and 6.25 formula unit percent (f.u. %) in four crystallographic phases: monoclinic, orthorhombic, polar-orthorhombic, and tetragonal. The setup of geometries and definition of the nominal concentration are explained in the Methods section and Supporting Information. In total, we performed the geometry relaxation of 3450 structures of doped HfO_2 and ZrO_2.

During the geometry relaxation, an initial structure deforms or even undergoes a phase transition due to the presence of the doping atom. It is necessary to filter out these transitions and strong deformations in an automated manner because of the sheer amount of relaxed geometries. For this purpose, we introduce two filters: a dipole and an X-ray diffraction (XRD) filter, which are described in full detail in the Methods section. Only the structures that passed both filters were considered in the further analysis. In total, 537 out of 3450 structures were filtered out via these filters.

According to Duncan et al.,[37] the formation energies of the substitutional dopants D_M with M ∈ {Hf, Zr} and interstitial dopants D_I are written as

$$E_{\text{form}}(D_M) = E(D_M) - \left[\frac{n-1}{n}E(MO_2) + E(D) + E(O_2)\right] \quad (1)$$

$$E_{\text{form}}(D_I) = E(D_I) - [E(MO_2) + E(D)] \quad (2)$$

where $E(D_M)$ and $E(D_I)$ are the total energies of the relaxed structures doped with substitutional and interstitial defects, respectively, $E(MO_2)$ is the total energy of the pristine supercell of the corresponding size, n is the number of formula units (f.u.) in the supercell (for instance, a primitive monoclinic cell contains 4 f.u.), and $E(D)$ and $E(O_2)$ are the chemical potentials of D and O_2, respectively. Subtracting the formation energies of the interstitial and substitutional dopants from each other yields $E^{\text{rel}}_{\text{form}}(D)$, the relative formation energy of the dopant D. Here the dependency on the chemical potential of the dopant, which is very much influenced by the experimental conditions, is eliminated

$$E^{\text{rel}}_{\text{form}}(D) = E(D_I) - E(D_M) - \frac{1}{n}E(MO_2) + E(O_2) \quad (3)$$

Note that the subtraction also cancels out some of the insufficiencies of the chosen electronic structure method. $E^{\text{rel}}_{\text{form}}$ depends only on the experimental parameter $E(O_2)$, the chemical potential of O_2, which is calculated here for a perfect

https://dx.doi.org/10.1021/acsami.0c08310
ACS Appl. Mater. Interfaces 2020, 12, 32915−32924

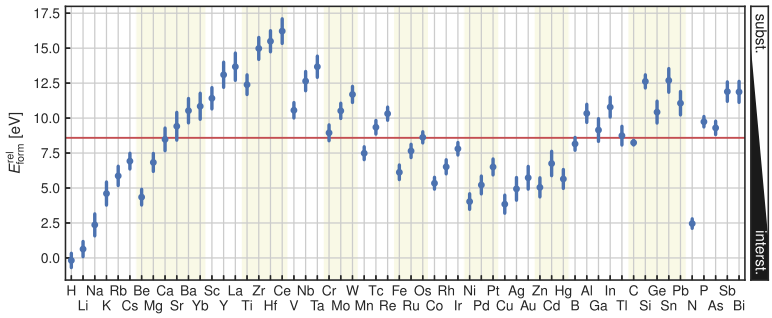

Figure 1. Relative formation energies of the considered dopants. The values are averaged over the host materials (HfO_2 and ZrO_2), nominal doping concentrations (3.125 and 6.25 f.u. %), and crystal phases (monoclinic, orthorhombic, polar-orthorhombic, and tetragonal). The error bars give the standard deviations. The dopants on the horizontal axis are sorted by their group and period in the periodic table of elements. Yb and Ce from the lanthanide series are assigned to the beryllium and titanium groups because of the similarity of the electronic structures. The red line is the reference for the incorporation type of defects taken from the work of Duncan et al.[37] The dopants lying above the red line rather build a substitutional defect. The dopants below the line rather build an interstitial defect.

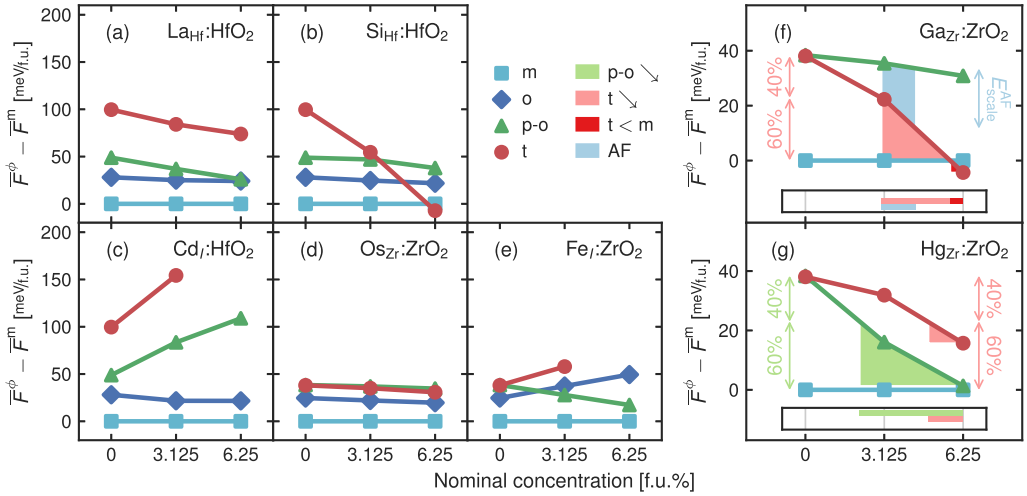

Figure 2. Free energies of the crystal phases in (a) substitutional La-doped HfO_2, (b) substitutional Si-doped HfO_2, (c) interstitial Cd-doped HfO_2, (d) substitutional Os-doped ZrO_2, (e) interstitial Fe-doped ZrO_2, (f) substitutional Ga-doped ZrO_2, and (g) substitutional Hg-doped ZrO_2 vs the doping concentration at 300 K. The free energy of each crystal phase $\phi \in \{m, o, p\text{-}o, t\}$ is referenced to the corresponding m-phase. The *TS* contribution is taken from the work of Künneth et al.[11] and assumed to be independent of the doping concentration. (f,g) Visual aid for understanding how the bars in Figure 3 are derived from the free energies of the crystal phases. For clarity, the o-phase lines are omitted in (f,g).

O_2 ambient condition. Large values of $E^{rel}_{form}(D)$ indicate that the incorporation of the dopant as a substitutional defect is favored. For small values, the interstitial defect is favored.

The values of the relative formation energy depend on the valence of the dopant ion and its size in terms of ionic radius, and range around a few eV. Interestingly, the values rather depend to a small extent on the host material, the doping concentration, and the crystal phase. Applying eq 3 to a particular doping species, having two different host materials, two concentrations, and four phases, 16 different values of E^{rel}_{form} for each of the 58 doping species can be calculated. Figure 1 depicts the means and standard deviations of E^{rel}_{form} for different doping species. In the figure, it becomes apparent that these values have a surprisingly small variation of about 100 meV, meaning that the relative formation energy of a dopant, defining its incorporation type into the host, is a major trend essentially independent of the host material, doping concentration, and crystal phase. After determining the incorporation type of the dopant, further dependencies will be investigated in detail.

The general expectations are confirmed in trends: the tetravalent Ti, Zr, Hf, Ce, Si, Ge, Sn, and Pb rather build a substitutional defect on the metal site in HfO_2 or ZrO_2 because their relative formation energies range in the upper energy interval. Hydrogen, having the smallest radius of all the considered species, also has the smallest E^{rel}_{form}, which means that it is more likely to build an interstitial defect compared to all other species. While large doping atoms substitute the metal atoms in the host, small doping atoms can build interstitials with a higher probability. However, almost all calculated relative formation energies are positive, implying that the considered doping species never build interstitials, except for hydrogen.

Duncan et al.[37] calculated the relative formation energies of doped HfO_2 in the monoclinic phase at approximately 1% doping concentration. Their results show that several dopants can also create an interstitial defect in HfO_2. They cite several publications dealing with both substitutional and interstitial defects in HfO_2 in accordance with their findings. However, Duncan et al. used a spin-polarized local density approximation (LDA)[38] with an on-site Coulomb correction (LDA + *U*) formalism, whereas we utilized the simple LDA approach. The relative formation energies from our study over four crystal phases are in remarkable agreement with Duncan et al.'s

https://dx.doi.org/10.1021/acsami.0c08310
ACS Appl. Mater. Interfaces 2020, 12, 32915−32924

calculations for the monoclinic phase and smaller doping concentrations (see the Supporting Information for comparison), except for the overall shift of the values. This discrepancy in the zero lines in Duncan et al.'s and current studies is attributed to the LDA + U corrections to Hf (U^d = 6.6 eV) and O (U^p = 9.5 eV) atoms in Duncan et al.'s work, describing more precisely the electronic structure of the doped HfO_2 which allows better values for the absolute formation energy. To be in good agreement with experimental findings and compensate these U corrections in our calculations, we indicate the overall shift of 8.5 eV as a red line in Figure 1—the substitutional−interstitial-filter—which is precisely the zero line in Duncan et al.'s calculations. E^{rel}_{form} above or below this line correspondingly leads to the substitutional or interstitial defect. However, this filter should not be considered as a hard filter, because the relative formation energy depends on the chemical potential of O_2, which is governed by experiment. This means that, for instance, Pt—being somewhat below the substitutional−interstitial-filter—can also build a substitutional defect if the chemical potential of oxygen is high enough (cf. eq 3). This can be ensured if the oxygen plasma is used instead of the ambient oxygen. Another possibility to alter the chemical potential of oxygen during the annealing procedure is to use specific electrode materials, for instance, TiO_2[34] or apply different pressure conditions[39] (see the Supporting Information).

Si and La are very well-known promoters of ferroelectric characteristics in HfO_2. Richter et al.[40] and Schroeder et al.[41] describe them as "fragile" and "robust" ferroelectric systems, respectively. These two dopants are also two good examples for discussion of the energies of the crystal phases depending on the doping concentration. It is expected that Si and La will build substitutional defects with a low concentration of oxygen vacancies during the crystallization process under oxygen-rich conditions (electronic compensation of defects).[31,32,34]

The La doping causes the free energy of the p-o- and t-phases to decline, as depicted in Figure 2a. The p-o-phase stays far below the t-phase and eventually crosses the m-phase at approximately 15% if extrapolated. Above this La concentration, the p-o-phase is bulk stable. However, it is known experimentally that even at 5% La-doping, the ferroelectric characteristics emerge,[41] while the m-phase is expected to prevail from the energy landscape of the crystal phases.

Si-doped HfO_2 exhibits more complicated behavior in experiments, having a ferroelectric window in the 2.6−4.3% doping concentration range and an antiferroelectric window between 4.3 and 5.6%. Above 5.6%, the tetragonal phase is stabilized.[17] The experimentally observed tetragonal phase can be easily explained by means of Figure 2b: at the concentration of about 5.8%, the t-line surpasses the m-line and the t-phase becomes bulk stable.

However, within this simple picture of free energies, the ferroelectric characteristics of moderately La-doped HfO_2 and ferro- or antiferroelectric characteristics of Si-doped HfO_2 cannot be explained because the m- and o-phases have lower free energies than the p-o- and t-phases. Additional effects stemming from, for instance, strain conditions,[17,42] kinetics of phase formation,[43,44] primitive cell volumes, thickness of the HfO_2 films,[10] and their grained structure[11,45,46] can directly or effectively increase the free energies of the m- and o-phases. Owing to the generally higher kinetic barriers in the o-phase if compared with the m-phase,[47] the m-phase is preferred to form over the o-phase, making the o-phase even less probable to occur in HfO_2 and ZrO_2. Therefore, the m- and o-lines in Figure 2 can be shifted upward in the reader's mind for the purpose of the discussion. In this case, the crossing point of the m- and p-o-lines is shifted to the left, allowing the ferroelectricity to occur at a lower doping concentration for both dopants. Additionally, the t-line crosses the p-o-line at 3.5% in Si-doped HfO_2. Above this concentration, the field-induced phase transition from the paraelectric t-phase to the ferroelectric p-o-phase can occur, explaining the antiferroelectric behavior.[12,17] The direct comparison of Figure 2a,b makes it evident that the free energy of the p-o-phase reacts more strongly with the increase of the doping concentration of La than of Si, which implies that La promotes the ferroelectricity more strongly than Si. This observation correlates with the terminology of "robust" and "fragile" ferroelectric systems.

We performed a vast study on doped HfO_2 and ZrO_2 in a self-consistent manner. This allows us to compare the computed energies and make statements about the relative effect strengths of different dopants on the ferroelectricity and antiferroelectricity of HfO_2 and ZrO_2 systems. For instance, Figure 2c−e compares interstitial Cd-doped HfO_2, substitutional Os-doped ZrO_2, and interstitial Fe-doped ZrO_2. Obviously, Cd strongly disfavors the p-o- and t-phases, hence the probability is low that Cd will promote any ferro- or antiferroelectric characteristics in HfO_2. Os has a very weak effect on these two phases, which is even slightly weaker than the Si effect on the p-o-phase. Therefore, Os might or might not promote ferroelectricity in ZrO_2. Fe strongly decreases the free energy of the p-o-phase, even more significantly than La in HfO_2 it does, while the free energies of o- and t-phases are increased. As a consequence, Fe should be an even better promoter of the ferroelectric characteristics in ZrO_2 if compared with La-doped HfO_2. To sum up, the characteristics of doped HfO_2 and ZrO_2 in the frame of the energy landscape of the crystal phases can be described in the simple observations as the decline in the free energy of phases with increasing doping concentration and their crossings.

For the quantitative description of these observations, certain criteria must be defined. We chose La-doped HfO_2, which is known to be a good ferroelectric system, to serve as a link between the experiment and simulation. In the experiment, 5% La concentration is sufficient for the ferroelectric properties to emerge, which corresponds to 15−20 meV/f.u. of free energy decline of the p-o-phase. The p-o-phase, according to the simulation, still remains above the m- and o-phases, hence further mechanisms are needed for its stabilization, as discussed previously. This free energy scale can be applied to other dopants, allowing a direct comparison with La. Dopants, which lead to the free energy decline of the p-o-phase larger than 20 meV/f.u., are expected to be better ferroelectricity promoters in HfO_2 as La, and vice versa. This absolute free energy scale is approximately 40% of the p-o-phase energy with respect to the m-phase. The relative scale of 40% applied to the p-o-phase in ZrO_2 leads to a similar absolute energy scale because the free energies of the p-o-phase referenced to the corresponding m-phases are similar in pure HfO_2 and ZrO_2 (cf. Figure 2c,d). Hence, we considered a 40% free energy decline for the p-o-phase to be significant to promote the ferroelectric characteristics in both HfO_2 and ZrO_2, as sketched in Figure 2f,g. Such a high threshold efficiently separates the dopants with a high impact on the ferroelectric characteristics, like La, from those with low impact. The crossing of the p-o- and m-lines, meaning that p-o-phase becomes bulk stable, is then an even stronger indication of the potential ferroelectric characteristics.

https://dx.doi.org/10.1021/acsami.0c08310
ACS Appl. Mater. Interfaces 2020, 12, 32915−32924

The t-phase of the undoped HfO_2 and ZrO_2 has a particularly high value of the dielectric constant κ, meaning that it can be used as an insulator in dynamic random access memory, for instance, for these oxides.[48] Provided that the dielectric constant does not decrease with an introduction of dopants, which we have not investigated in this paper, the decline of the free energy of the t-phase can be interpreted as an enhancement of the high-κ characteristics in HfO_2 and ZrO_2. The same relative energy scale as for the p-o-phase can be applied to the t-phase. While the free energy of the t-phase in ZrO_2 is comparable to the free energies of the p-o-phase in both HfO_2 and ZrO_2, the t-phase free energy in HfO_2 is twice as high. Correspondingly, it leads to a doubled absolute energy scale for the HfO_2 t-phase. However, it is still plausible because the effect of the temperature on the free energy of the HfO_2 t-phase is also approximately twice as high compared to the ZrO_2 t-phase.[11]

Finally, the antiferroelectric characteristics can be explained through the field-induced transition from the t- to the p-o-phase.[12] As a necessary condition, the free energy of the t-phase must be smaller than the free energy of the p-o-phase. In comparison, this condition is fulfilled for undoped ZrO_2 but not for HfO_2 (Figure 2). Experimentally, the antiferroelectric behavior is precisely observed for pure ZrO_2, but not for HfO_2.[25] The crystal phases of both HfO_2 and ZrO_2 exhibit similar trends in terms of the total energy and the crystal volume except for the t-phase, leading to the advantageous small total energy and large volume differences for the p-o- and t-phases in ZrO_2, compared to HfO_2 (see the Supporting Information). This can be explained by the combined effect of the different bonding strengths between atoms in HfO_2 and ZrO_2 and the high crystal symmetry of the t-phase, which makes this phase stand out from the others. Hence, the antiferroelectric characteristics are more to be expected in doped ZrO_2 than in doped HfO_2 because pure ZrO_2 has an intrinsic tendency toward it. Additionally, we have to estimate the antiferroelectric energy scale $E_{\text{scale}}^{\text{AF}}$—the maximal energy difference between the free energies of the t- and p-o-phases—which can be surmounted by the external electric field. While the crossing of the t- and p-o-lines defines the left boundary for the doping concentration range for the antiferroelectric activity, $E_{\text{scale}}^{\text{AF}}$ defines its right boundary. For the estimation, we use

$$E_{\text{scale}}^{\text{AF}} = E_{\text{scale}}^{\text{ext}} P_s V \tag{4}$$

where $E_{\text{scale}}^{\text{ext}}$ is the common, external electric field scale used in experiments, P_s the spontaneous polarization of the p-o-phase, and V its volume. The $E_{\text{scale}}^{\text{AF}}$ is then the energy which is needed to separate the charges across volume V in order to build up polarization P_s at the given external field, starting from the paraelectric and moving toward the polarized (ferroelectric) phase. We took 2 MV cm^{-1} to be the typical, external electric field. The spontaneous polarization and the volume of the formula unit of the p-o-phase for HfO_2 and ZrO_2 are 56, 54 μC cm^{-2} and 32.2, 32.9 $Å^3$, respectively.[36] These values yield the antiferroelectric energy scale of 22 meV/f.u. Furthermore, for the antiferroelectric characteristics, we enforce the condition that the free energy of the t-phase is decreased significantly.

Using these definitions, the bars in Figure 3 depict the concentration range for which the significant effects of the dopants on HfO_2 and ZrO_2 are expected. The light and dark red bars show the decline of the free energy of the t-phase, thereby suggesting the corresponding dopants for high-κ applications, for instance. The light and dark green bars indicate the enhancement of the ferroelectric characteristics. Lastly, the

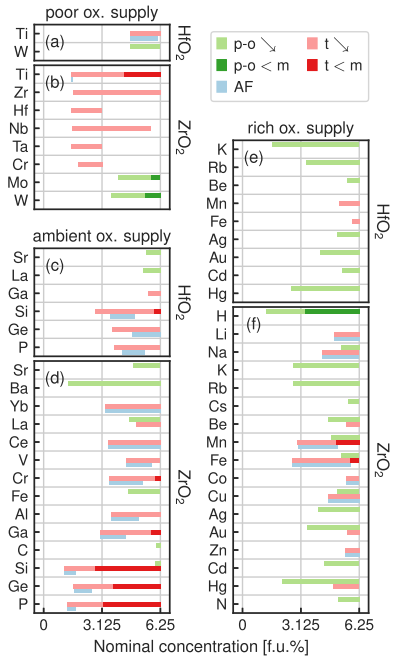

Figure 3. Concentration ranges for dopants which have a significant effect on the free energies of the p-o- and t-phases in HfO_2 and ZrO_2 under different oxygen supply conditions. The light and dark red bars encode the concentration ranges in which the free energy of the t-phase is significantly reduced, allowing the high-κ application for these dopants. The light and dark green bars mark the concentration ranges in which the ferroelectricity is enhanced. The light blue bars show the antiferroelectric concentration range windows. The dopants in (a,b) are interstitial defects, in (e,f) are substitutional, and in (c,d) both defect types are mixed, as shown in Figure 1.

light blue bars mark the strengthening of the antiferroelectric characteristics. They all are overlapping with the corresponding red bars because we require the decline of the free energy of the t-phase for the antiferroelectric behavior. Furthermore, Figure 3 distinguishes the effect of the dopants depending on the oxygen supply during the crystallization process.

Consider Fe-doped ZrO_2. According to Figure 1, Fe atoms tend to incorporate as interstitials into ZrO_2 under ambient oxygen conditions, because its relative formation energy lies below the substitutional−interstitial-filter. As discussed previously, we expect that this defect promotes the ferroelectricity in ZrO_2 under this condition. This fact is marked by the corresponding light green bar in Figure 3d in agreement with Figure 2e. However, if the oxygen supply or its chemical potential is increased in a way that the relative formation energy for Fe surpasses the substitutional−interstitial filter (eq 3), then Fe can possibly build a substitution for the Zr atom. In this case, the energy landscape for crystal phases looks different (see the Supporting Information), which allows Fe to enhance not only the ferroelectricity in ZrO_2 but also the tetragonality and antiferroelectricity for different ranges of concentrations. The corresponding doping concentration ranges are depicted in Figure 3f. Hence, the ferroelectric/antiferroelectric behavior in Fe-doped ZrO_2 can be tuned by the oxygen supply and doping concentration.

Two other examples for ZrO_2 are Mo and W dopants. Under ambient oxygen conditions, they are expected to build a substitutional defect, because their relative formation energies lie above the substitutional−interstitial-filter in Figure 1. In this

https://dx.doi.org/10.1021/acsami.0c08310
ACS Appl. Mater. Interfaces 2020, 12, 32915−32924

case, however, these dopants do not exhibit any significant effect on ZrO_2 characteristics. In contrast, Mo and W are expected to strongly promote the ferroelectricity in ZrO_2 if they build the interstitial defects. In fact, at around 6 f.u. %, the p-o-line crosses the m-line for these dopants, making the p-o-phase bulk stable (see the Supporting Information). In order to force these two dopants to build the interstitials instead of Zr substitution, the relative formation energy must decrease below the substitutional−interstitial filter in Figure 1, which can be achieved with a reduced oxygen supply, or a reduced oxygen chemical potential. Therefore, Mo and W are marked by light and dark green bars in Figure 3b.

Sr-doped HfO_2, which was found to exhibit ferroelectric characteristics,[33,49] is accordingly depicted in Figure 3c. As previously discussed, La is also marked here as a ferroelectricity promoter in HfO_2. However, Si-doped HfO_2 under ambient oxygen conditions have only the tetragonality and antiferroelectricity to a significant degree but not the ferroelectricity, as discussed previously. The reason for this is that we chose a rather high threshold for significance. Only if the dopant cuts the free energy of the p-o-phase by 40% with respect to the free energy of the m-phase will this dopant be considered as a good enhancer of the ferroelectric characteristics, which Si in HfO_2 is not, according to our calculations. This does not mean that Si does not enhance the ferroelectricity in HfO_2, but that all other dopants marked by the green bar in Figure 3 are better for this application than Si.

Hg doping is also worthy of discussion: it is depicted in Figure 3e,f as a good enhancer of the ferroelectric properties in both HfO_2 and ZrO_2. The free energy of the Hg-doped p-o-phase declines at a high rate with the increase of the concentration, if Hg is incorporated as a substitutional defect (Figure 2g and Supporting Information). Having a similar electronic structure to Sr, which builds metal substitution in HfO_2 and ZrO_2,[33] Hg can also possibly build a substitution under conditions of elevated oxygen supply. Hence, Hg, Mo, and W provide an option to manufacture bulk ferroelectric ceramics, especially if ZrO_2 is used.

For pure ZrO_2, Starschich et al.[12] measured a piezoelectric coefficient of 10 pm V^{-1}. For Si-doped HfO_2, the following values were recently published: d_{33} = 20 pm V^{-1} and d_{31} = −11.5 pm V^{-1}.[18,19] All the authors explain their measured piezoelectric properties with the field-induced phase transition from a nonpolar to a polar crystal phase, because the piezoelectric coefficient changes during the wake-up procedure, in which a double hysteresis polarization−field curve transitions to a simple one. The piezoelectric effect itself is then attributed to the change in the crystal phase volume during the transition.

Figure 4 depicts the polarization (a,b) and the corresponding strain (c,d) hysteresis loops produced by the modeling of the field-induced phase transition. It is an example of how the form of the polarization double hysteresis, whether it is fully pinched or not, affects the form of the strain hysteresis. Both these strain loops are desired depending on the application. In the idealistic model, for the fully pinched polarization double hysteresis loop (a), the polar regions transform back to 100% nonpolar at zero external field, which in turn leads to the minimal strain in (c). However, if the polarization does not vanish after the removal of the external field (b), the minimal strain state cannot be achieved because of the nonvanishing polar regions leading to the remnant strain (d). Thus, the maximal achievable strain change $\Delta\sigma_{max}$ is reduced. Hence, for optimizing the stroke, the fully pinched polarization double hysteresis is favored. However,

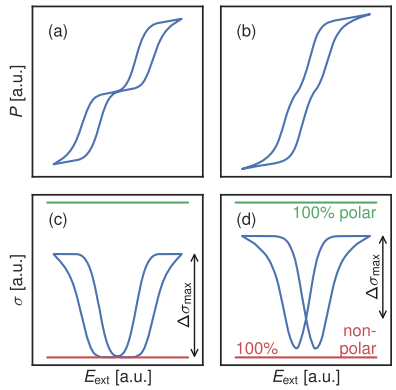

Figure 4. Modeled fully pinched (a) and partially pinched (b) polarization double hysteresis loops and the corresponding strain hysteresis loops (c,d).

the problem is that the strain changes slowly with the external electric field around zero in (c) if compared to (d). The rate of strain change around zero electric field defines the piezoelectric coefficient *d*. Therefore, if an application demands high and linear *d*, the not-pinched polarization double hysteresis is preferable. Jo et al.[50] discuss these aspects in full detail.

Nevertheless, both the nonlinear stroke $\Delta\sigma_{max}$ and the linear piezoelectric coefficient *d* increase, if the difference between the crystalline volumes of the polar and nonpolar phases increases. The higher the difference, the stronger the overall device volume changes are during the transition from 100% nonpolar fraction (red lines in (c,d)) to 100% polar fraction (green lines). This effectively stretches the strain hysteresis loops in the vertical direction. However, 100% of the polar fraction cannot be achieved at finite external electric fields.

Using the calculated volumes of the t- and p-o-phases, which we set to be the nonpolar and polar phases, respectively, we can estimate the piezoelectric effect of the dopants in HfO_2 and ZrO_2 stemming from the field-induced phase transition. The hydrostatic piezoelectric coefficient can be estimated as follows

$$d_h = \sigma_h \frac{1}{E^{ext}_{scale}} = \frac{V_{p\text{-}o} - V_t}{V_t} \frac{1}{E^{ext}_{scale}} \quad (5)$$

where σ_h is the hydrostatic strain and $V_{p\text{-}o}$ and V_t are the volumes of the p-o- and t-phases, respectively. As in eq 4, E^{ext}_{scale} gives the typical external electric field scale in experiments and we chose it to be 2 MV cm^{-1}. The hydrostatic piezoelectric coefficient for a single crystal is defined as $d_{31} + d_{32} + d_{33}$ and for a polycrystalline material as $2d_{31} + d_{33}$.[50] Applying eq 5 to our self-consistent study, we can directly compare the effect of different dopants on the piezoelectric activity for both HfO_2 and ZrO_2. In order to compare our calculated values with the experimental values for the piezoelectric coefficients and strains, we use the following definitions

$$d^\star = \frac{1}{3} d_h \quad (6)$$

$$S = \frac{1}{3} \sigma_h \quad (7)$$

Figure 5 shows the calculated strains *S* due to the phase transformation, and from them the estimated piezoelectric coefficients $d^\star$. Only those dopants expected to exhibit the antiferroelectric behavior, as marked in Figure 3, are considered

https://dx.doi.org/10.1021/acsami.0c08310
ACS Appl. Mater. Interfaces 2020, 12, 32915−32924

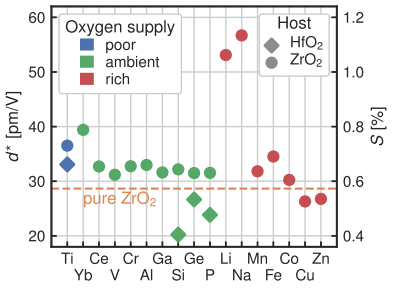

Figure 5. Calculated strains and estimated piezoelectric coefficients stemming from the field-induced transition from the t- to p-o-phase.

here. $d^{\star}$ defines the theoretical upper bound for the piezoelectric effect, because not all p-o-regions in a device can be induced from the t-phase at a finite external electric field, as shown in Figure 4.

The correspondingly calculated crystalline piezoelectric coefficients $d^{\star}_{cryst}$ for HfO_2 and ZrO_2 are −1.9 and −2.0 pm V^{-1}, respectively,[51] which is 1 order of magnitude smaller than the coefficients estimated herein, stemming from the field-induced phase transition. According to our findings, the Si-doped HfO_2 with very high experimentally measured piezoelectric coefficients is expected to be the weakest of the piezoelectric systems considered here. Table 1 compares the

Table 1. Comparison of the Experimental and Our Estimated Values

system	d [pm V^{-1}]	S [%]
Current Study		
ZrO_2	29	0.58
Yb:ZrO_2	39	0.78
Li:ZrO_2	53	1.06
Na:ZrO_2	57	1.14
Si:HfO_2	20	0.4
Crystalline Coefficients		
ZrO_2[51]	−2.0	
HfO_2[51]	−1.9	
Experiments		
ZrO_2[12]	10	0.15
Mg:ZrO_2[29]	10	0.28
Si:HfO_2[18]	19.8	0.3
Si:HfO_2[19]	−11.5 (d_{31})	
AlN[16]	4.3	
$(MgZr)_{0.35}Al_{0.65}N$[16]	12.2	
$LiNbO_3$[20]	10	6×10^{-3}
PZT-based[20]	333−2000	0.11−0.82
BNT-based[20]	214−844	0.13−0.57
KNN-based[20]	235−901	0.039−0.34

piezoelectric coefficients and strains found experimentally for different material systems with the current findings. For the pure ZrO_2 and Mg-doped ZrO_2 samples, the experimental values have been obtained from thick CSD layers[12,29] which seem to be not optimized as the hysteresis loops show an unexplained thickness dependence. The Si-doped HfO_2 samples, however, are obtained from mature ALD processes.[18,19] The piezoelectric coefficients of PZT-, BNT-, and KNN-based materials are unattainable for HfO_2 and ZrO_2—a consequence of the lower dielectric constant—however, their achievable strain values can be improved by the optimized ZrO_2.

Another important figure of merit for piezoelectric applications is the electromechanical coupling coefficient (EMCC), which is defined as follows

$$k^2 = \frac{d^2}{s^E \varepsilon^T} \tag{8}$$

with d, s^E, and ε^T denoting the piezoelectric coefficient, elastic compliance at a constant electric field, and electric permittivity at constant mechanical stress, respectively.[52] However, this formula can not be applied to the incipient type of ferroelectrics like ZrO_2, as it uses crystalline properties. Instead, we consider the effective EMCC

$$k_{eff}^2 = \frac{U_m^2(d_{eff})}{U_e(s_{eff}^E)U_d(\varepsilon_{eff}^T)} \tag{9}$$

where U_e is the elastic, U_d electric, and U_m mutual energies.[53] These energies depend only on the effective elastic compliance s_{eff}^E, electric permittivity ε_{eff}^E, and piezoelectric coefficient d_{eff}, which is $d^{\star}$ in our case. Thus, eq 9 precisely resembles the dependence of the EMCC on the basic material coefficients, as described by eq 8. The electric permittivity of ZrO_2 ranges from 20 to 40, depending on the crystal phase. This is beneficial if compared to perovskite-based piezoelectrics for which the electric permittivity can achieve values of several thousands. However, the perovskite-based materials exhibit more superior piezoelectric constants, as reported in Table 1, which acts against the benefit of the electric permittivity. The comparison of AlN with ZrO_2 reveals a converse picture: ZrO_2 is inferior to AlN in terms of the electric permittivity ($\varepsilon_{AlN} \approx 9$) and superior in terms of the piezoelectric coefficient (Table 1). This shows the potential of ZrO_2 to compete with both materials in terms of the electromechanical coupling constant.

3. CONCLUSIONS

In conclusion, we have found a number of promising dopants for HfO_2 and ZrO_2 materials for enhancing the ferroelectric, antiferroelectric, and piezoelectric characteristics, as shown in Figures 3 and 5. However, the assumption for this study is that the defects are completely electronic compensated, as we did not take the oxygen vacancies into consideration. In a first step, we classified the dopants with respect to the incorporation type, using the relative formation energy E_{form}^{rel}. We found E_{form}^{rel} to be dependent on the dopant, but—to our surprise—only marginally dependent on the host material, crystal phase, and concentration.

Mo and W are expected to promote the ferroelectricity in ZrO_2 to a very large extent under poor oxygen supply conditions (Figure 3b), which in turn can lead to oxygen vacancies. Hence, it might be complicated to ensure both the conditions of interstitial incorporation of Mo and W and suppression of oxygen vacancies in an experiment. Nevertheless, it is worth investigating the effect of these dopants experimentally as well as theoretically with regard to their ionic charge compensation. Additionally, Mo, W, and Hg may be used to stabilize the polar-orthorhombic phase in ZrO_2 in a ceramic process, if oxygen vacancies can be sufficiently suppressed.

ZrO_2 shows generally a larger potential for piezoelectric applications than HfO_2 because of the approximately 80% larger volume difference between t- and p-o-phases. Li and Na are very promising dopants in ZrO_2 for the piezoelectric application. They enhance the piezoelectric effect approximately by a factor of 2 compared to pure ZrO_2. In contrast to Mo and W for the

https://dx.doi.org/10.1021/acsami.0c08310
ACS Appl. Mater. Interfaces 2020, 12, 32915−32924

ferroelectric application, these two dopants need oxygen-rich supply conditions, thus suppressing the oxygen vacancies and supporting the electronic charge compensation. By the same token, the dopants in Figure 3e,f rather achieve the corresponding enhancements as the dopants in Figure 3a,b. Additionally, Yb also increases the piezoelectric effect in ZrO_2 by one-third under ambient oxygen supply conditions.

4. METHODS

4.1. Substitutional Doping. In our study, we considered 48- and 96-atomic supercells of HfO_2 and ZrO_2 for the incorporation of doping as a substitution on the metal site. The metal (cationic) sites in the monoclinic, orthorhombic, polar-orthorhombic, and tetragonal crystal phases are mutually equivalent owing to the crystal symmetry. Hence, it is sufficient to consider only one metal site for the substitutional doping. Substituting one metal atom in a 96-atomic supercell with one doping atom leads to the doping concentration of 3.125 f.u. %, while 1 f.u. consists of three atoms. One substitutional doping in a 48-atomic supercell corresponds to 6.25 f.u. % concentration.

The primitive unit cells of the considered crystal phases consist of 12, 24, 12, and 6 atoms, respectively. The 12-atomic conventional tetragonal cell can be built through a coordinate transformation. Hence, a $1 \times 2 \times 2$ supercell is used for the construction of a 96-atomic orthorhombic cell, while a $2 \times 2 \times 2$ supercell is used for the other three crystal phases. One doping atom in such periodic supercells produces an isotropic dopant distribution, where the distance between the doping atoms in all three Cartesian directions is approximately 10 Å for all phases. However, there are three possible supercells for 48-atomic m-, p-o-, and t-cells: $1 \times 2 \times 2$, $2 \times 1 \times 2$, and $2 \times 2 \times 1$. For the o-phase, there are only two possibilities: $2 \times 1 \times 2$, and $2 \times 2 \times 1$. These doped supercells exhibit strong anisotropy of the doping distribution because along one direction the doping atoms are separated only by approximately 5 Å. To eliminate the effect of anisotropy of the dopant distribution, we considered all the described 48-atomic supercells.[32] For evaluation purposes, the averages of the total energies and supercell volumes were calculated.

4.2. Interstitial Doping. While the starting geometries for the structural relaxation of the substitutionally doped supercells are unambiguously defined by the metal sites, there are an infinite number of positions, where an interstitial defect can be placed in the crystal for the structural relaxation. We utilized an interstitial site-finder code implemented in the pymatgen library.[54] Using generous parameters for the finder, we found up to 38 starting positions for different crystal phases for an interstitial Si atom in ZrO_2, which we chose to be our sample system. During the structural relaxation, however, different geometries often collapsed into the same relaxed structure. The examination of these relaxed geometries showed that the low distortion of the host geometry by the interstitial corresponds to the low total energy. Furthermore, the interstitials in these weakly distorted geometries built a similar arrangement with the metal atoms across all crystal phases. Therefore, for each crystal phase and material host, we chose certain positions for the interstitial sites, which are similar to each other. These universal interstitial sites were used for all the doping species considered herein. These interstitial positions are listed in the Supporting Information.

For the interstitial incorporation of the doping atoms, the same supercells of HfO_2 and ZrO_2 as for the substitutional dopants were considered. Introducing the interstitial atom into the supercells, 49- and 97-atomic supercells are produced. The question then arises as to how to define the doping concentration. In order to compare the effect of a dopant, for instance, on the volume of the host depending on the incorporation type, we defined the small and large supercells to have 16 and 32 f.u., respectively. To emphasize this, we use the term nominal concentration for both the substitutional and interstitial dopants, which is given in f.u. %.

4.3. DFT Calculations. The electronic structure calculations in this study were conducted with the all-electron code FHI-AIMS[55] using the LDA.[38] The code implements the Monkhorst−Pack grid for the k-point definition. Depending on their orientation, for the 48- and 49-atomic structures, $4 \times 2 \times 2$, $2 \times 4 \times 2$, and $2 \times 2 \times 4$ grids were used. For the 96- and 97-atomic structures, it was a $2 \times 2 \times 2$ grid. For the geometry relaxation, the convergence criterion for the ions was set to 1×10^{-3} eV Å^{-1}. These settings were tested in a convergence study and found to be sufficient. The all-electron code has predefined basis sets for nearly all elements of the periodic table, and does not rely on the transferability of the constructed pseudopotentials, which is of great advantage for a dopant screening study.

All the calculations were performed in two steps: first, the geometries were pre-relaxed using the light basis set of FHI-AIMS with default settings. In the second step, the basis set was changed to the tight set with the first and second tier settings fully enabled, which delivered precise geometries and total energies.

4.4. Dipole Filter. The dipole filter[32] compares the dipole moments evaluated from the Hirshfeld charge analysis of the relaxed doped structures with the reference dipole moments of the corresponding undoped polar structures of HfO_2 and ZrO_2, which are 0.019 and 0.015 eÅ/f.u., respectively. If the absolute value of the dipole moment of a relaxed m-, o-, or t-structure exceeds half of the reference dipole moment, then this initially nonpolar structure has built a significant dipole moment during the relaxation and is deemed to have been filtered out. If the dipole moment of a relaxed p-o-structure projected on a plane perpendicular to the polar axis exceeds half of the reference dipole moment, then the dipole has acquired a significant rotation, and this structure is also deemed to have been filtered out. Furthermore, the reduction of the dipole moment projected on the polar axis below half of the reference means a significant decline of the polarization. In this case, such a structure is also deemed to have been filtered out.

4.5. XRD Filter. This filter compares multiple and—in a certain way—calculated X-ray scattering patterns of the doped HfO_2 or ZrO_2 structures with the corresponding reference patterns. For the calculation of the scattering patterns, we used the Atomic Simulation Environment (ASE) library,[56] which implements the Debye formula.

How this filter exactly works is best explained by way of a particular example. Consider a relaxed 97-atomic structure of HfO_2, which was initially in the t-phase configuration, with an interstitial defect. In order to tell if the structure has significantly deformed and can no longer be considered as a t-phase structure, it is necessary to analyze not only the relaxed structure as a whole but also the oxygen atoms and Hf atoms with the dopant separately from each other. Hence, the scattering pattern is calculated for the full 97-atomic structure as well as for the 64-atomic structure, which consists only of oxygen atoms, and the 33-atomic structure, which is made of Hf atoms and the doping atom. The ASE implementation of the Debye formula works only for molecules but not for structures with a periodic boundary conditions. Therefore, we build approximately $3 \times 3 \times 3$ nm^3 large molecules out of the 97-, 64-, and 33-atomic periodic structures. This size of the molecules is large enough to reproduce the important features in the scattering patterns of extended crystals. Additionally, the scattering patterns for all four crystal phases of pure HfO_2 are computed as references in the same manner: $3 \times 3 \times 3$ nm^3 molecules consisting of both hafnium and oxygen, only of oxygen, and only of hafnium atoms. Finally, the doped molecules are compared with four corresponding references for different phases by computing residuals, which are defined as follows

$$\mathrm{res}^{\phi} = \frac{\int |\mathcal{I}_{\mathrm{D}} - \mathcal{I}^{\phi}_{\mathrm{pure}}| d(2\theta)}{\int \mathcal{I}^{\phi}_{\mathrm{pure}} d(2\theta)} \tag{10}$$

where $\phi \in \{\mathrm{m}, \mathrm{o}, \mathrm{p\text{-}o}, \mathrm{t}\}$, $\mathcal{I}_{\mathrm{D}}$ and $\mathcal{I}^{\phi}_{\mathrm{pure}}$ are the calculated scattering patterns of the doped and pure molecules, respectively. The integrations are performed over the scattering angle 2θ, which is chosen to range from 5 to 85°. For the scattering patterns, the wavelength of 1.5 μm is utilized.

The smaller the residual res^{ϕ} is, the greater the similarity of the relaxed doped structure to the pure phase ϕ. For this particular example, if in all three cases: (i) all hafnium and oxygen atoms plus the doping atoms, (ii) only oxygen atoms, and (iii) hafnium and doping atoms, the residuals for the t-phase happen to be the smallest among the corresponding residuals for the other phases, and then the particular

https://dx.doi.org/10.1021/acsami.0c08310
ACS Appl. Mater. Interfaces 2020, 12, 32915−32924

doped structure is considered to have remained in the tetragonal crystal phase. However, if in one or more cases, this is not true, then this structure is filtered out from further analyses.

■ ASSOCIATED CONTENT

Supporting Information

The Supporting Information is available free of charge at https://pubs.acs.org/doi/10.1021/acsami.0c08310.

Total energies and volumes of all the doped supercells computed here, comparison of relative formation energies from our study and those from Duncan et al., comparison of total energies and volumes of the four crystal phases of both pure HfO_2 and ZrO_2 for different exchange correlation potentials, starting geometries for the relaxation calculations (Cartesian coordinates of the four primitive crystal phases of both pure HfO_2 and ZrO_2 and Cartesian coordinates of the interstitial sites), and dependence of oxygen chemical potential on the precursor pressure (PDF)

Geometry and interstitial site positions of all the relaxed structures (ZIP)

■ AUTHOR INFORMATION

Corresponding Author

Alfred Kersch − *Munich University of Applied Sciences, 80335 Munich, Germany;* orcid.org/0000-0003-4407-555X; Email: alfred.kersch@hm.edu

Author

Max Falkowski − *Munich University of Applied Sciences, 80335 Munich, Germany;* orcid.org/0000-0002-5426-4509

Complete contact information is available at: https://pubs.acs.org/10.1021/acsami.0c08310

Notes

The authors declare no competing financial interest.

■ ACKNOWLEDGMENTS

M.F. received funding from the Deutsche Forschungsgemeinschaft (German Research Foundation) in the frame of the project "Zeppelin" (Project KE 1665/5-1). M.F. and A.K. gratefully acknowledge the Gauss Centre for Supercomputing e.V. (www.gauss-centre.eu) for funding this project by providing computing time on the GCS Supercomputer SuperMUC-NG at Leibniz Supercomputing Centre (www.lrz.de) under the grant: pr27su.

■ REFERENCES

(1) Park, M. H.; Hwang, C. S. Fluorite-Structure Antiferroelectrics. *Rep. Prog. Phys.* **2019**, *82*, 124502.

(2) Park, M. H.; Lee, Y. H.; Mikolajick, T.; Schroeder, U.; Hwang, C. S. Review and Perspective on Ferroelectric HfO_2-Based Thin Films for Memory Applications. *MRS Commun.* **2018**, *8*, 795−808.

(3) Hoffmann, M.; Fengler, F. P. G.; Herzig, M.; Mittmann, T.; Max, B.; Schroeder, U.; Negrea, R.; Lucian, P.; Slesazeck, S.; Mikolajick, T. Unveiling the Double-Well Energy Landscape in a Ferroelectric Layer. *Nature* **2019**, *565*, 464−467.

(4) Chernikova, A.; Kozodaev, M.; Markeev, A.; Negrov, D.; Spiridonov, M.; Zarubin, S.; Bak, O.; Buragohain, P.; Lu, H.; Suvorova, E.; Gruverman, A.; Zenkevich, A. Ultrathin $Hf_{0.5}Zr_{0.5}O_2$ Ferroelectric Films on Si. *ACS Appl. Mater. Interfaces* **2016**, *8*, 7232−7237.

(5) Ambriz-Vargas, F.; Kolhatkar, G.; Broyer, M.; Hadj-Youssef, A.; Nouar, R.; Sarkissian, A.; Thomas, R.; Gomez-Yáñez, C.; Gauthier, M. A.; Ruediger, A. A Complementary Metal Oxide Semiconductor Process-Compatible Ferroelectric Tunnel Junction. *ACS Appl. Mater. Interfaces* **2017**, *9*, 13262−13268.

(6) Ryu, H.; Wu, H.; Rao, F.; Zhu, W. Ferroelectric Tunneling Junctions Based on Aluminum Oxide/Zirconium-Doped Hafnium Oxide for Neuromorphic Computing. *Sci. Rep.* **2019**, *9*, 20383.

(7) Qin, J.; Huang, F.; Li, X.; Deng, L.; Kang, T.; Markov, A.; Yue, F.; Chen, Y.; Wen, X.; Liu, S.; Xiong, Q.; Semin, S.; Rasing, T.; Modotto, D.; Morandotti, R.; Xu, J.; Duan, H.; Bi, L. Enhanced Second Harmonic Generation from Ferroelectric HfO_2-Based Hybrid Metasurfaces. *ACS Nano* **2019**, *13*, 1213−1222.

(8) Dragoman, M.; Aldrigo, M.; Modreanu, M.; Dragoman, D. Extraordinary Tunability of High-Frequency Devices Using $Hf_{0.3}Zr_{0.7}O_2$ Ferroelectric at Very Low Applied Voltages. *Appl. Phys. Lett.* **2017**, *110*, 103104.

(9) Park, M. H.; Lee, Y. H.; Kim, H. J.; Kim, Y. J.; Moon, T.; Kim, K. D.; Müller, J.; Kersch, A.; Schroeder, U.; Mikolajick, T.; Hwang, C. S. Ferroelectricity and Antiferroelectricity of Doped Thin HfO_2-Based Films. *Adv. Mater.* **2015**, *27*, 1811−1831.

(10) Hoffmann, M.; Schroeder, U.; Schenk, T.; Shimizu, T.; Funakubo, H.; Sakata, O.; Pohl, D.; Drescher, M.; Adelmann, C.; Materlik, R.; Kersch, A.; Mikolajick, T. Stabilizing the Ferroelectric Phase in Doped Hafnium Oxide. *J. Appl. Phys.* **2015**, *118*, 072006.

(11) Künneth, C.; Materlik, R.; Kersch, A. Modeling Ferroelectric Film Properties and Size Effects from Tetragonal Interlayer in $Hf_{1-x}Zr_xO_2$ Grains. *J. Appl. Phys.* **2017**, *121*, 205304.

(12) Starschich, S.; Schenk, T.; Schroeder, U.; Boettger, U. Ferroelectric and Piezoelectric Properties of $Hf_{1-x}Zr_xO_2$ and Pure ZrO_2 Films. *Appl. Phys. Lett.* **2017**, *110*, 182905.

(13) Mimura, T.; Shimizu, T.; Funakubo, H. Ferroelectricity in $YO_{1.5}$-HfO_2 films around 1 μm in thickness. *Appl. Phys. Lett.* **2019**, *115*, 032901.

(14) Wang, C.; Pan, C.; Wang, Z. Electronic Skin for Closed-Loop Systems. *ACS Nano* **2019**, *13*, 12287−12293.

(15) Park, J.; Lee, Y.; Lee, H.; Ko, H. Transfer Printing of Electronic Functions on Arbitrary Complex Surfaces. *ACS Nano* **2020**, *14*, 12−20.

(16) Yokoyama, T.; Iwazaki, Y.; Onda, Y.; Nishihara, T.; Sasajima, Y.; Ueda, M. Highly Piezoelectric co-Doped AlN Thin Films for Wideband FBAR Applications. *IEEE Trans. Sonics Ultrason.* **2015**, *62*, 1007−1015.

(17) Böscke, T. S.; Müller, J.; Bräuhaus, D.; Schröder, U.; Böttger, U. Ferroelectricity in Hafnium Oxide Thin Films. *Appl. Phys. Lett.* **2011**, *99*, 102903.

(18) Kirbach, S.; Kühnel, K.; Weinreich, W. Piezoelectric Hafnium Oxide Thin Films for Energy-Harvesting Applications. *2018 IEEE 18th International Conference on Nanotechnology (IEEE-NANO)*; IEEE, 2019; pp 31−34.

(19) Mart, C.; Kämpfe, T.; Hoffmann, R.; Eßlinger, S.; Kirbach, S.; Kühnel, K.; Czernohorsky, M.; Eng, L. M.; Weinreich, W. Piezoelectric Response of Polycrystalline Silicon-Doped Hafnium Oxide Thin Films Determined by Rapid Temperature Cycles. *Adv. Electron. Mater.* **2020**, *6*, 1901015.

(20) Hao, J.; Li, W.; Zhai, J.; Chen, H. Progress in High-Strain Perovskite Piezoelectric Ceramics. *Mater. Sci. Eng., R* **2019**, *135*, 1−57.

(21) Zheng, T.; Wu, J.; Xiao, D.; Zhu, J. Recent Development in Lead-Free Perovskite Piezoelectric Bulk Materials. *Prog. Mater. Sci.* **2018**, *98*, 552−624.

(22) Jo, W.; Granzow, T.; Aulbach, E.; Rödel, J.; Damjanovic, D. Origin of the Large Strain Response in $(K_{0.5}Na_{0.5})NbO_3$-modified $(Bi_{0.5}Na_{0.5})TiO_3$-$BaTiO_3$ Lead-Free Piezoceramics. *J. Appl. Phys.* **2009**, *105*, 094102.

(23) Noor-A-Alam, M.; Olszewski, O. Z.; Nolan, M. Ferroelectricity and Large Piezoelectric Response of AlN/ScN Superlattice. *ACS Appl. Mater. Interfaces* **2019**, *11*, 20482−20490.

(24) Talley, K. R.; Sherbondy, R.; Zakutayev, A.; Brennecka, G. L. Review of High-Throughput Approaches to Search for Piezoelectric Nitrides. *J. Vac. Sci. Technol., A* **2019**, *37*, 060803.

(25) Müller, J.; Böscke, T. S.; Schröder, U.; Mueller, S.; Bräuhaus, D.; Böttger, U.; Frey, L.; Mikolajick, T. Ferroelectricity in Simple Binary ZrO_2 and HfO_2. *Nano Lett.* **2012**, *12*, 4318−4323.

(26) Reyes-Lillo, S. E.; Garrity, K. F.; Rabe, K. M. Antiferroelectricity in Thin-Film ZrO_2 from First Principles. *Phys. Rev. B: Condens. Matter Mater. Phys.* **2014**, *90*, No. 140103(R).
(27) Liu, J.; Liu, S.; Liu, L. H.; Hanrahan, B.; Pantelides, S. T. Origin of Pyroelectricity in Ferroelectric HfO_2. *Phys. Rev. Appl.* **2019**, *12*, 034032.
(28) *Ferroelectricity in Doped Hafnium Oxide: Materials, Properties and Devices*; Schroeder, U., Hwang, C. S., Funakubo, H., Eds.; Woodhead Publishing Series in Electronic and Optical Materials; Woodhead Publishing, 2019.
(29) Starschich, S.; Böttger, U. Doped ZrO_2 for Future Lead Free Piezoelectric Devices. *J. Appl. Phys.* **2018**, *123*, 044101.
(30) Yoneda, S.; Hosokura, T.; Kimura, M.; Ando, A.; Shiratsuyu, K. Nonlinear Polarization Responses of ZrO_2-Based Thin Films Fabricated by Chemical Solution Deposition. *Jpn. J. Appl. Phys.* **2017**, *56*, 10PF07.
(31) Künneth, C.; Materlik, R.; Falkowski, M.; Kersch, A. Impact of Four-Valent Doping on the Crystallographic Phase Formation for Ferroelectric HfO_2 from First-Principles: Implications for Ferroelectric Memory and Energy-Related Applications. *ACS Appl. Nano Mater.* **2018**, *1*, 254−264.
(32) Falkowski, M.; Künneth, C.; Materlik, R.; Kersch, A. Unexpectedly Large Energy Variations from Dopant Interactions in Ferroelectric HfO_2 from High-Throughput Ab Initio Calculations. *npj Comput. Mater.* **2018**, *4*, 73.
(33) Materlik, R.; Künneth, C.; Mikolajick, T.; Kersch, A. The Impact of Charge Compensated and Uncompensated Strontium Defects on the Stabilization of the Ferroelectric Phase in HfO_2. *Appl. Phys. Lett.* **2017**, *111*, 082902.
(34) Materlik, R.; Künneth, C.; Falkowski, M.; Mikolajick, T.; Kersch, A. Al-, Y-, and La-Doping Effects Favoring Intrinsic and Field Induced Ferroelectricity in HfO_2: A First Principles Study. *J. Appl. Phys.* **2018**, *123*, 164101.
(35) Batra, R.; Huan, T. D.; Rossetti, G. A.; Ramprasad, R. Dopants Promoting Ferroelectricity in Hafnia: Insights From a Comprehensive Chemical Space Exploration. *Chem. Mater.* **2017**, *29*, 9102−9109.
(36) Schenk, T.; Fancher, C. M.; Park, M. H.; Richter, C.; Künneth, C.; Kersch, A.; Jones, J. L.; Mikolajick, T.; Schroeder, U. On the Origin of the Large Remanent Polarization in La:HfO_2. *Adv. Electron. Mater.* **2019**, *5*, 1900303.
(37) Duncan, D.; Magyari-Köpe, B.; Nishi, Y. Properties of Dopants in HfO_x for Improving the Performance of Nonvolatile Memory. *Phys. Rev. Appl.* **2017**, *7*, 034020.
(38) Perdew, J. P.; Wang, Y. Accurate and Simple Analytic Representation of the Electron-Gas Correlation Energy. *Phys. Rev. B: Condens. Matter Mater. Phys.* **1992**, *45*, 13244−13249.
(39) Reuter, K.; Scheffler, M. Composition, Structure, and Stability of RuO_2(110) as a Function of Oxygen Pressure. *Phys. Rev. B: Condens. Matter Mater. Phys.* **2001**, *65*, 035406.
(40) Richter, C.; Schenk, T.; Park, M. H.; Tscharntke, F. A.; Grimley, E. D.; LeBeau, J. M.; Zhou, C.; Fancher, C. M.; Jones, J. L.; Mikolajick, T.; Schroeder, U. Si Doped Hafnium Oxide—A "Fragile" Ferroelectric System. *Adv. Electron. Mater.* **2017**, *3*, 1700131.
(41) Schroeder, U.; Richter, C.; Park, M. H.; Schenk, T.; Pešić, M.; Hoffmann, M.; Fengler, F. P. G.; Pohl, D.; Rellinghaus, B.; Zhou, C.; Chung, C.-C.; Jones, J. L.; Mikolajick, T. Lanthanum-Doped Hafnium Oxide: A Robust Ferroelectric Material. *Inorg. Chem.* **2018**, *57*, 2752−2765.
(42) Shiraishi, T.; Katayama, K.; Yokouchi, T.; Shimizu, T.; Oikawa, T.; Sakata, O.; Uchida, H.; Imai, Y.; Kiguchi, T.; Konno, T. J.; Funakubo, H. Impact of Mechanical Stress on Ferroelectricity in $(Hf_{0.5}Zr_{0.5})O_2$ Thin Films. *Appl. Phys. Lett.* **2016**, *108*, 262904.
(43) Park, M. H.; Lee, Y. H.; Mikolajick, T.; Schroeder, U.; Hwang, C. S. Thermodynamic and Kinetic Origins of Ferroelectricity in Fluorite Structure Oxides. *Adv. Electron. Mater.* **2019**, *5*, 1800522.
(44) Lee, Y. H.; Hyun, S. D.; Kim, H. J.; Kim, J. S.; Yoo, C.; Moon, T.; Kim, K. D.; Park, H. W.; Lee, Y. B.; Kim, B. S.; Roh, J.; Park, M. H.; Hwang, C. S. Nucleation-Limited Ferroelectric Orthorhombic Phase Formation in $Hf_{0.5}Zr_{0.5}O_2$ Thin Films. *Adv. Electron. Mater.* **2019**, *5*, 1800436.
(45) Materlik, R.; Künneth, C.; Kersch, A. The origin of ferroelectricity in $Hf_{1-x}Zr_xO_2$: A computational investigation and a surface energy model. *J. Appl. Phys.* **2015**, *117*, 134109.
(46) Park, M. H.; Lee, Y. H.; Kim, H. J.; Schenk, T.; Lee, W.; Kim, K. D.; Fengler, F. P. G.; Mikolajick, T.; Schroeder, U.; Hwang, C. S. Surface and Grain Boundary Energy as the Key Enabler of Ferroelectricity in Nanoscale Hafnia-Zirconia: A Comparison of Model and Experiment. *Nanoscale* **2017**, *9*, 9973−9986.
(47) Liu, S.; Hanrahan, B. M. Effects of Growth Orientations and Epitaxial Strains on Phase Stability of HfO_2 Thin Films. *Phys. Rev. Mater.* **2019**, *3*, 054404.
(48) Fischer, D.; Kersch, A. The Effect of Dopants on the Dielectric Constant of HfO_2 and ZrO_2 from First Principles. *Appl. Phys. Lett.* **2008**, *92*, 012908.
(49) Schenk, T.; Müller, S.; Schroeder, U.; Materlik, R.; Kersch, A.; Popovici, M.; Adelmann, C.; Van Elshocht, S.; Mikolajick, T. Strontium Doped Hafnium Oxide Thin Films: Wide Process Window for Ferroelectric Memories. *2013 Proceedings of the European Solid-State Device Research Conference (ESSDERC)*; IEEE, 2013; pp 260−263.
(50) Jo, W.; Dittmer, R.; Acosta, M.; Zang, J.; Groh, C.; Sapper, E.; Wang, K.; Rödel, J. Giant Electric-Field-Induced Strains in Lead-Free Ceramics for Actuator Applications - Status and Perspective. *J. Electroceram.* **2012**, *29*, 71−93.
(51) Materlik, R. Stabilization of Ferroelectricity in Hafnia, Zirconia and their Mixtures by Dopants and Interface Energy: First Principles Calculations and a Phenomenological Model. Ph.D. Thesis, Technische Universität Dresden, 2019.
(52) An American National Standard. IEEE Standard on Piezoelectricity. *IEEE Transactions on Sonics and Ultrasonics*, 1987.
(53) Chang, S. H.; Rogacheva, N. N.; Chou, C. C. Analysis of Methods for Determining Electromechanical Coupling Coefficients of Piezoelectric Elements. *IEEE Trans. Sonics Ultrason.* **1995**, *42*, 630−640.
(54) Ong, S. P.; Richards, W. D.; Jain, A.; Hautier, G.; Kocher, M.; Cholia, S.; Gunter, D.; Chevrier, V. L.; Persson, K. A.; Ceder, G. Python Materials Genomics (pymatgen): A Robust, Open-Source Python Library for Materials Analysis. *Comput. Mater. Sci.* **2013**, *68*, 314−319.
(55) Blum, V.; Gehrke, R.; Hanke, F.; Havu, P.; Havu, V.; Ren, X.; Reuter, K.; Scheffler, M. Ab Initio Molecular Simulations with Numeric Atom-Centered Orbitals. *Comput. Phys. Commun.* **2009**, *180*, 2175−2196.
(56) Hjorth Larsen, A.; Jørgen Mortensen, J.; Blomqvist, J.; Castelli, I. E.; Christensen, R.; Dułak, M.; Friis, J.; Groves, M. N.; Hammer, B.; Hargus, C.; Hermes, E. D.; Jennings, P. C.; Bjerre Jensen, P.; Kermode, J.; Kitchin, J. R.; Leonhard Kolsbjerg, E.; Kubal, J.; Kaasbjerg, K.; Lysgaard, S.; Bergmann Maronsson, J.; Maxson, T.; Olsen, T.; Pastewka, L.; Peterson, A.; Rostgaard, C.; Schiøtz, J.; Schütt, O.; Strange, M.; Thygesen, K. S.; Vegge, T.; Vilhelmsen, L.; Walter, M.; Zeng, Z.; Jacobsen, K. W. The atomic simulation environment-a Python library for working with atoms. *J. Phys.: Condens. Matter* **2017**, *29*, 273002.

https://dx.doi.org/10.1021/acsami.0c08310
ACS Appl. Mater. Interfaces 2020, 12, 32915−32924